

An Experimental Investigation of Wingtip Vortices Generated by a Reverse Delta Wing of Different Wing Configurations

Mengyizhe He

Master of Engineering

Department of Mechanical Engineering

McGill University, Montréal, Québec, Canada

December 2018

A thesis submitted to McGill University in partial fulfillment
of the requirements of the degree of Master of Engineering

© Mengyizhe Shawn He 2018

ACKNOWLEDGEMENTS

First and foremost, I would like to thank my thesis supervisor, Professor Timothy Lee, for believing in me and for having pushed my limits and helped me see what I am capable of.

I would also like to thank my colleagues at the Aerodynamics Laboratory, Vincent Tremblay-Dionne, Lok Sun Ko, and David Huitema, for being not only great labmates but also dear friends outside the academy. In particular, Lok Sun is thanked for showing me the ropes and sharing his humour when I had lost mine. Vincent is thanked for always being there to offer me any advice or help I sought. His relentless work energy motivated me to keep going at some of the most difficult times.

Furthermore, I would like to pay appreciation to the supports from my family: to my parents, Katrina and Haibo who had given me the opportunity to attend this great institute, and more importantly, the chance to experience the world; to my partner, Delphine Rey, who brings endless love and joy to my life, which had helped me through many hardships.

Last but not least, I want to extend my gratitude to the staff of the Department of Mechanical Engineering at McGill, especially Anne-Marie Pierre, Mathieu Beauchesne, and Lydia Dyda who had all assisted me in completing this project.

ABSTRACT

The reverse delta wing (RDW) planform is uniquely seen on the Lippisch-type wing-in-ground effect vehicles that have emerged as a new and sustainable mode of commercial sea travel in the last decade, yet public archives of RDWs are rarely seen and relevant academic studies are scarce. This study investigates wingtip vortices generated by different RDW configurations outside ground effect (GE) as to expand knowledge about RDWs and to set potential benchmarks for future studies in GE. Flow measurements of 16" in chord 65°-sweep RDW models were obtained using a seven-hole pressure probe at low subsonic speeds and a Reynolds number of 3.3×10^5 . Major attention was paid to the streamwise evolution and characteristics of the tip vortices at an angle of attack of 16°. The various wing models were configured with, separately and jointly, trailing-apex cropping, anhedral and winglets. Gurney flaplike strips were also examined as a lift augmentation and passive flow control device. In addition, the lift and drag forces of each configuration were measured via a force balance to supplement the flow-field data. The cropping had a minimal impact on the RDW vortices and aerodynamic forces while the anhedral engendered faster-rotating vortices and minimized lift-induced drag. The side-edge strips enhanced the vortex strength and wing lift, but also drag. The winglets generated a co-rotating vortex pair but kept the total vortex strength mostly intact. Lift based on vortex circulation underestimated the experimental values by 1.5-11.3%, suggesting that the RDW vortex strength can represent majority of the actual lift. Lastly, induced drag computed using vorticity flow field constituted 17.6-27.5% of the total drag.

ABRÉGÉ

La technologie de l'aile delta inversée, autrefois été conçue par l'allemand Alexander Lippisch, est utilisée de nos jours par certains fabricants pour la conception d'une nouvelle génération de véhicules à effet de sol. Malgré le regain de popularité de ce moyen de transport économique et écologique, peu d'articles scientifiques sont actuellement disponibles. Cette thèse, destinée à l'étude des tourbillons générés par différentes configurations d'aile delta inversée (l'angle de flèche = 65°) dans un écoulement libre, permettra d'améliorer les connaissances sur ce type d'aile et d'établir une référence pour des futures études en effet de sol. Des mesures d'écoulement de la traînée à proximité de l'aile ont été obtenues en utilisant une sonde de pression à sept trous, à des vitesses subsoniques et un nombre de Reynolds fixé à 3.3×10^5 , plus particulièrement sur l'évolution et les caractéristiques des tourbillons en bout d'aile à un angle d'attaque sélectionné de 16° . Les différents modèles d'ailes ont été configurés avec le recadrage d'apex traînant, le dièdre négatif, et des winglets, séparément et ensemble. Des bandes latérales, communément appelé «Gurney flap», ont également été utilisées en tant que dispositif passif d'augmentation de portance. Les mesures de portance et de traînée ont été obtenues pour supporter les mesures d'écoulement. Le recadrage d'apex traînant a eu un impact négligeable sur la vorticit   mais important sur les coefficients a  rodynamiques de l'aile. Par ailleurs, la modification du di  dre n  gatif, en anglais «Anhedral angle», a engendr  e des vitesses tangentielles plus grandes et une tra  n  e minimis  e. Les bandes lat  rales ont

augmenté la force du tourbillon, la portance et la traînée des différentes configurations. Les winglets ont générés une paire de tourbillons co-rotatifs et une circulation inchangée. La portance, calculée théoriquement à l'aide de la circulation du tourbillon, a été sous-estimée analytiquement par rapport aux valeurs expérimentales (de 1.5 à 11.3%). Cela suggère que la force du tourbillon d'une aile delta inversée peut représenter la majorité de la portance réelle. Pour conclure, à partir des mesures de vorticité, la traînée induite a été calculée et estimée à environ 17.6 à 27.5% de la traînée totale.

TABLE OF CONTENTS

ACKNOWLEDGEMENTS	ii
ABSTRACT	iii
ABRÉGÉ	iv
LIST OF TABLES	viii
LIST OF FIGURES	ix
LIST OF SYMBOLS	xii
LIST OF ABBREVIATIONS	xiv
1 Introduction	1
1.1 Background and Related History	1
1.2 Motivation	10
2 Literature Review	13
2.1 Typical Tip Vortex	13
2.2 Delta Wing	22
2.3 Reverse Delta Wing	31
2.4 Objectives	39
3 Experimental Apparatuses and Methodology	40
3.1 Flow Facility	40
3.2 Wing Models	42
3.3 Instrumentation	45
3.3.1 Seven-hole Pressure Probe	45
3.3.2 Two-dimensional Traverse Mechanism	51
3.3.3 Two-component Force Balance	51
3.4 Data Acquisition and Reduction	53

3.4.1	Vortex Flow Properties	54
3.4.2	Lift and Induced Drag Estimation	58
3.5	Experimental Uncertainty	61
4	Results and Discussion	64
4.1	Baseline Wing - 65°-sweep Reverse Delta Wing	64
4.1.1	Dependence of the Vortex Structure on the Angle of Attack	65
4.1.2	Streamwise Progression of the Vortex Flow Characteristics of the BW at $\alpha = 16^\circ$	68
4.1.3	Aerodynamic Performance of the BW	84
4.2	Effect of 30%c Cropping on the 65° RDW	87
4.2.1	Vortex Flow Characteristics of the Cropped RDW	88
4.2.2	Aerodynamic Performance of the Cropped RDW	89
4.3	Effect of 15° Anhedral on the 30%c Cropped RDW	90
4.3.1	Vortex Flow Characteristics of the Cropped RDW with Anhedral	90
4.3.2	Aerodynamic Forces of the Cropped RDW with Anhedral	93
4.4	Effect of 2%c Side-edge Strip on Different RDWs	93
4.4.1	Vortex Flow Characteristics of the SES-equipped RDWs	94
4.4.2	Aerodynamic Performances of the SES-equipped RDWs	98
4.4.3	Effect of Joint Anhedral and SES on the cropped RDW	99
4.5	Effect of 45° Winglets on the 30%c Cropped RDW with 15° Anhedral	99
4.5.1	Vortex Flow Characteristics of the Winglet-equipped RDW	100
4.5.2	Aerodynamic Performance of the Winglet-equipped RDW	101
4.6	Lift Estimation Using Vortex Strength	102
4.7	Induced Drag Estimation Using Streamwise Vorticity Field	104
5	Conclusions	107
	References	111

LIST OF TABLES

<u>Table</u>		<u>page</u>
3-1	Wing configurations and geometric parameters	43
3-2	Experimental uncertainties of flow conditions and wing models	62
3-3	Experimental uncertainties of force balance measurements	62
3-4	Experimental uncertainties of seven-hole pressure probe measurements	63
4-1	Predicted and measured lift coefficients at $\alpha = 16^\circ$	103
4-2	Estimated and theoretical induced drag coefficients at $\alpha = 16^\circ$	106

LIST OF FIGURES

<u>Figure</u>	<u>page</u>
1-1 Trailing vortices of a NACA0012 rectangular wing at $\alpha = 24^\circ$ and $Re = 10^5$ with applied suction to keep flow attached (left) [1]; vortices above a 75° thin delta wing at $\alpha = 20^\circ$ and $Re = 2 \times 10^4$ (right) [1].	5
1-2 Early WIG crafts in the 1960s: Lippisch-type Collins X-112 of the US [2] (left), Ekranoplan-type KM of the USSR [3] (right).	6
1-3 Most recent WIG crafts: (a)-(b) AirFish-8 of Singapore in flight[4], (c) WSH-500 of South Korea [5], (d) CYG-11 of P.R. of China [6].	10
1-4 Schematic diagrams of the AirFish-8 (Flightship-8) [7].	11
2-1 Illustration of initial tip vortex roll-up [8].	14
2-2 Leading-edge vortex (LEV) structure on slender delta wings. (a) Sketch of the LEVs over a slender delta wing [9]; (b) filaments of dye flow over a 65° delta wing at 2 inch/sec [10]; (c) three regions inside a LEV [9]; (d) reattachment location of different delta-wing sweep angles [11].	24
2-3 Flow visualization photographs of a 65° reverse delta wing (RDW) using smoke-wire (top figures) and dye-injection (bottom figures) techniques. (a) and (c) $\alpha = 14^\circ$ (b) and (d) $\alpha = 20^\circ$. SVF denotes spanwise vortex filament [12].	32
2-4 Streamwise development of normalized axial vorticity contours of a 65° reverse delta wing (RDW) (top) and delta wing (DW) (bottom) at $\alpha = 12^\circ$ [13].	33
2-5 Aerodynamic coefficients of reverse delta wing (RDW) and delta wing (DW). DW65 and RDW65 denote 65° -sweep DW and RDW, respectively. (W&Z) denotes (Wang and Zhang) and (W&K) denotes (Wentz and Kohlman). [13]	36

3-1	Joseph A. Bombardier subsonic wind tunnel. (a) tunnel inlet; (b) tunnel outlet; (c) tunnel schematic diagram [14].	41
3-2	Wing configurations. (BW, DW, crp, ahd, wgt, SES each denotes baseline wing, delta wing, cropped, anhedral, winglet and side-edge strip, respectively.)	44
3-3	General arrangement of the experimental setup in the test section. . .	46
3-4	Seven-hole pressure probe and traverse mechanism. (a) schematic diagram of the probe [14]; (b) the traverse.	47
3-5	Photographs of the two-component force balance. (a) force balance sensors under the tunnel [14]; (b) force balance test section setup. .	52
3-6	Data acquisition overview.	55
3-7	RDW+SES at $x/c=1.2$. (a) adaptive grid; (b) cross-stream velocity vectors; (c) axial vorticity contours.	56
3-8	Axial vorticity contour plot at $x/c = 1.2$ demonstrating total circulation Γ_o and effective span b'	59
4-1	Iso-vorticity contours of the baseline RDW vortex at $x/c = 1.01$ for $8^\circ \leq \alpha \leq 28^\circ$	66
4-2	Iso-axial velocity contours of the baseline RDW vortex at $x/c = 1.01$ for $8^\circ \leq \alpha \leq 28^\circ$	67
4-3	Three-dimensional representation of iso-vorticity contours at all streamwise stations at $\alpha = 16^\circ$	69
4-4	NACA0012 tip vortex flow contours at selected x/c . (a1)-(a3) Axial vorticity, (a4)-(a6) axial velocity, and (a7)-(a9) tangential velocity.	72
4-5	(a)-(g) (k)-(l) Streamwise dependence of a series of vortex parameters, (h)-(j) distribution of selected vortex parameters across the vortex core at $x/c = 1.5$	74
4-6	Close-up of normalized iso-vorticity contours at selected x/c . ζ_p denotes $\zeta_{peak}c/U$	78
4-7	Normalized axial velocity contours at selected x/c	80

4–8	Normalized streamwise velocity contours at selected x/c	82
4–9	(a) Axial vorticity, (b) tangential velocity, and (c) axial velocity distributions of the baseline RDW vortex along a vertical line passing the vortex centre at selected x/c	85
4–10	Lift and drag coefficient curves. (a)&(d) C_L curves, (b)&(e) C_D curves, (c)&(f) L/D curves.	86
4–11	Streamwise development of the induced drag coefficients computed with the Maskell wake-intergral model.	105

LIST OF SYMBOLS

AR	wing aspect ratio
b	wing span
b'	effective wing span
c	wing chord
C_D	total drag coefficient
C_{Di}	lift-induced drag coefficient
C_L	total lift coefficient
C_{Lmax}	maximum total lift coefficient
D	total drag force
D_i	lift-induced drag force
h_{SES}	SES height
L	total lift force
L/D	lift-to-drag ratio
r	vortex radius
r_c	vortex core radius
Re	chord-based Reynolds number
r_o	vortex outer radius
S	wing surface area
S_{BW}	baseline wing surface area

U	free-stream flow velocity
u_c	vortex core axial velocity
u, v, w	axial, vertical and spanwise velocity
v_θ	tangential velocity
$v_{\theta peak}$	peak tangential velocity
x, y, z	streamwise, vertical and spanwise flow direction
y_c	vertical vortex centre position
z_c	horizontal vortex centre position
α	angle of attack
α_{ss}	angle of attack at static stall
Γ	circulation
Γ_c	core circulation
Γ_o	total circulation
Δ	scan grid resolution
δ_A	anhedral angle
ζ	streamwise vorticity
ζ_{peak}	peak streamwise vorticity
Λ	sweep angle
ρ	free-stream air density
σ	a special source term
ϕ	velocity potential function
ψ	stream function

LIST OF ABBREVIATIONS

ahd	anhedral
BW	baseline wing
crp	cropping or cropped
DW	delta wing
FB	force balance
GE	ground effect
LEV	leading-edge vortex
OGE	outside ground effect
RDW	reverse delta wing
SES	Gurney flaplike side-edge strip
SVF	spanwise vortex filament
wgt	winglet
WIG	wing-in-ground effect

CHAPTER 1 Introduction

1.1 Background and Related History

Finite lifting surfaces can generate trailing vortices as a result of the pressure difference above and below the surface, creating upwash outboard and downwash inboard. A group of migrating geese flies efficiently using such phenomenon by staying in the upwash of the trailing vortices generated by the leader, hence a precise V-shape flight formation. Pilots learnt to operate in similar manners to save fuel and even perform aerobatics. While being advantageous in specifically arranged flight formations, it is often the hazardous impact of trailing vortices on aircraft passing through the wake zone that concerns aviation experts and operators globally. It is widely understood that an airplane during take-off and landing leaves behind trailing vortices and large turbulence near the ground that typically last several minutes. In the 1970s, the Federal Aviation Administration (FAA) instated operational procedures for airport take-off and landing to help planes avoid the vortex wake zone and greatly improved operation safety. However, it is still possible for an aircraft to encounter vortex wake turbulence, albeit cruising in steady air environment. In general, flying into a vortex could impose unwanted roll movements; going in between a pair of counter-rotating vortices could induce a sudden reduction/increase in the rate of climb/descent; moreover, passing transversely across the vortex wake could impose instabilities and significant stresses on the aircraft's structure. For instance, in April

2014, two Indian Air Force C-130J (Super Hercules) airplanes were conducting a low-level penetration training. Both airplanes were flying at 300 feet above ground level followed by a climb to 1000 feet altitude. After the lead aircraft completed the 1000-foot climb, the second one “failed to adopt a flight path to avoid the massive wake generated by the four engines of the lead C-130J”, and subsequently lost control and crashed near the Gwalior air base without any warning, killing all 5 personnel onboard [15]. Trailing vortices can be generated by various parts of an airplane, and the predominant of which are wingtip vortices or simply tip vortices. Tip vortices can be visible during aerodynamic condensation or freezing, when the water vapor in air condensates or freezes under the temperature drop in the low-pressure region of highly rotational air particles at the vortex core. Such occasions are rare, therefore aviation safety measures for any wake vortex encounters can only be derived from sheer experience, and more likely from better scientific understandings of this phenomenon.

As a wing generates lift with its forward motion, the pressure imbalance over the bottom and top of the wing surface gives rise to a spanwise flow that “leaks” outboard from below and “curls” inboard around the wingtip. The three-dimensional flow structure, exclusive to finite wings, is behind the formation of trailing tip vortices. The original vortex theory was first mentioned in *Aerodynamics* by English automobile engineer and aerodynamicist F. W. Lanchester in 1907, in which he theorized two “vortex ropes” (vortex filaments) aft wingtips, just four years after the first manned and sustained flight by the Wright Brothers of Ohio, USA. Lanchester’s book detailed the understanding of wingtip vortex, more importantly, it discussed

the connection between circulation and lift, an idea Lanchester first presented at the Birmingham Natural History and Philosophical Society as early as 1894 [16]. A year after the publication of *Aerodynamics*, Lanchester met and shared his ideas with German engineers Ludwig Prandtl and Theodore von Kármán who verified the vortex theory by “emitting an ammonia cloud into the air” a few years later [16], perhaps one of the earliest flow visualization experiments conducted in history. By integrating Lanchester’s ideas into analytical physical models, Prandtl came to develop and later refined the lifting-line theory that built the basis of modern wing theory and advanced the understanding of induced drag and wing aspect ratio. As a vortex filament must extend to the boundaries of the fluid or form a closed path (Helmholtz’s second theorem), the lifting-line theory represents the lift on a three-dimensional wing with infinitesimal spanwise sections of varying circulation. Each local section generates lift and creates a change in circulation that induces a trailing vortex filament, forming a continuous vortex sheet behind the wing. It allows for the computation of lift and induced drag from the wing geometry.

Supersonic Flight and Delta Wings

The WWI era sparked many airplane designs and development, most of which were biplanes featured rectangular or elliptical wing planforms and flew at speeds of roughly 130 mph. A German airplane designer Alexander M. Lippisch was inspired by the arrow-shaped flying seed of a tropical plant and created a triangular wing with thicker and longer wing surface near the fuselage for storage. The first motorized delta-winged airplane, Delta I, based on this idea took flight in 1931 [17]. At the fifth Volta Conference in 1935, the world-leading physicists in aeronautics

discussed the major issues in achieving faster and higher flights. The concept of swept wings for supersonic flight was introduced for the first time by Adolf Busemann, and the design of a supersonic wind tunnel was presented by Jakob Ackeret. Both were pupils of Ludwig Prandtl who himself presented shock wave formations in supersonic flows with pictures dating back to 1907 when he was simultaneously developing the incompressible inviscid airfoil theory [16]. Indeed, nowadays many regard Prandtl as the “father of modern aerodynamics”. The cumulative interests in supersonic flights soon led to the proof of the low-drag superiority of delta wings at supersonic speeds. Finally, on the brink of WWII, the famous Messerschmitt Me 163, a delta-wing rocket-powered German aircraft designed by Dr. Lippisch surpassed an unprecedented speed record of over 1000 km/h in 1941. Onwards, modern supersonic aircraft adopted the delta-wing design, and rigorous research on the aerodynamics of delta wings hasn’t stopped since.

Delta wings in general have a smaller wing aspect ratio (AR) than a conventional rectangular wing, resulting in smaller lift-to-drag ratios, L/D , and lift-curve slopes. To generate sufficient lift, they need to fly at high angles of attack and are often difficult to operate in take-off and landing, but the thin and highly swept wing gives unparalleled handling and manoeuvrability at high speeds. The strength of the delta wing root from the vortical flow over its surface which drastically differ from that of a typical tip vortex. The flow over the delta wing is dominated by a pair of leading-edge vortices (LEVs) where the vortex sheets separate at the leading edges and roll into a pair of counteracting spirals with tightening turns and accelerated axial flows in the core (Figure 1–1). Inside the LEV cores, jet-like flows (larger than

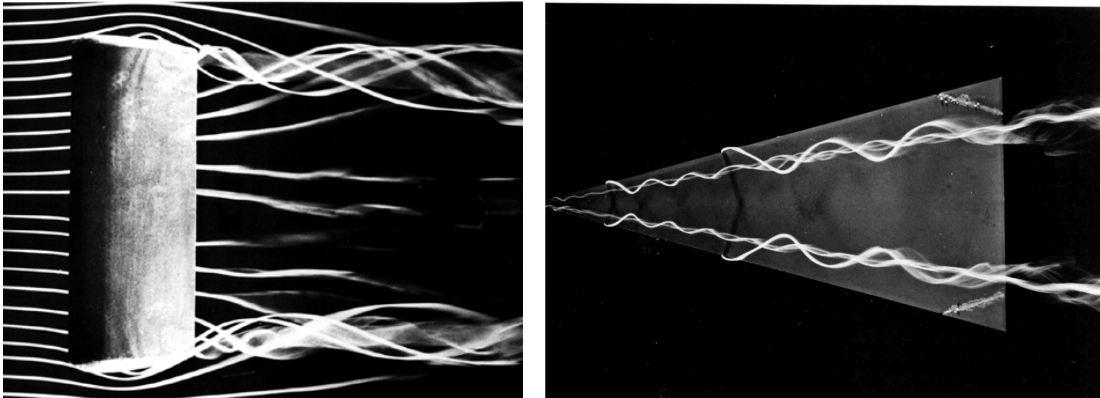


Figure 1-1: Trailing vortices of a NACA0012 rectangular wing at $\alpha = 24^\circ$ and $Re = 10^5$ with applied suction to keep flow attached (left) [1]; vortices above a 75° thin delta wing at $\alpha = 20^\circ$ and $Re = 2 \times 10^4$ (right) [1].

free-stream speed) create an upward suction on the top surface and in turn a lifting force, termed vortex lift, that plays a critical role in the lift generation of delta wings. Delta wings are categorized into slender and non-slender delta wings by the sweep angle Λ . Slender delta wings ($\Lambda \leq 65^\circ$) have been studied more extensively, because when comparing to their non-slender counterparts, not only can they utilize a larger percentage of the vortex lift, but also the high-sweep leading edges can stay inside the shock wave cone in supersonic flight.

Wing-in-Ground Effect Vehicles and Reverse Delta Wings

After WWII, Operation Paperclip brought Lippisch to work in the United States, where he developed interests in ground-effect vehicles, now commonly known as wing-in-ground effect (WIG) crafts. In ground effect (GE), a lifting system operating in close proximity to an underlying surface can experience an increase of the L/D ratio [18], also termed the aerodynamic efficiency. The ground hinders the roll-up

of wingtip vortices and restricts the downwash from reaching the top of the wing. Meanwhile, the static pressure in the flow below the wing is increased by the ram effect, and the dynamic pressure becomes smaller. It is as if the vehicle is gliding on a dynamic “air cushion”. The reduced turbulence levels in the “air cushion” lead to more efficient air mixing with the flow over the wing at the trailing edge. The collective result is a significant drop in induced drag and a boost in lift, hence the improved aerodynamic efficiency. The first flight of the Wright Flyer of 1903 that travelled 120 ft, roughly 4 ft above the ground, was an attribution to the GE phenomenon. By 1963, in the efforts led by Lippisch, the Collins X-112 “Aerofoil Boat” was the first WIG craft to feature an inverted or reverse delta wing planform and a large horizontal stabilizer, a revolutionary design that attained an unparalleled water speed of 124 km/h with one low-power engine (merely 25 hp), shown in Figure 1–2 (left). The strong wing anhedral was believed to funnel more flow into the “air cushion” as to further amplify the ram effect and lift in GE.



Figure 1–2: Early WIG crafts in the 1960s: Lippisch-type Collins X-112 of the US [2] (left), Ekranoplan-type KM of the USSR [3] (right).

Seemingly as a part of the technological rivalry in the Cold War, the Soviet Union secretly developed an experimental WIG craft, the Korabl-Maket (KM), also known as the “Caspian Sea Monster” (Figure 1–2 (right)). Comparing to the single-seater X-112, the KM, a Soviet Ekranoplan, was a 544-tonne turbojet-powered “flying ship” that could almost fill up an entire American football field. Equipped with a low-aspect-ratio ($AR = 2$) rectangular wing, it traversed the Caspian Sea at an operational speed of 500 km/h with the help of ten turbojet engines, each producing 13 tonnes of thrust for power augmented ram (PAR) take-off [18]. Interestingly, the eight engines mounted on the front pylons above and upstream of the wing also accelerated the air over the wing for even more lift. A large high-mounted tail shifted the centre of pitch downstream, which enabled a large range of height and pitch combinations. However, this design choice also came with the additional weight and viscous drag from the tail unit, with a small lift contribution in return. In fact, the lift-producing wing area took up less than 20% of the 92-by-37.6-meter rectangular envelope [19]. On the other hand, in spite of the same wing-tail/airplane configuration, the Collins X-112 used the tapered triangular shape of the reverse-delta planform to restrain the longitudinal shifting of the centre of pressure [18] in response to wave-induced instabilities, granting it superior stability at various ground height and pitch positions. The vehicle was able to perform “hydrodynamic jumps” during which it temporarily left the GE zone to overcome obstacles in its path. The RFB X-113 and X-114, its larger and more powerful successors built by German aircraft company Rhein Flugzeugbau (RFB), were claimed to have a L/D in the order of 25 [18], rendering the Lippisch design extremely efficient and

uniquely practical. For reference, the same-era Boeing 747-200 had more than triple the AR and a L/D of 15.5 in free flight [20]. The anhedral angle on the X-113 and X-114 elevated the larger fuselage above the water to circumvent the otherwise large hydrodynamic drag.

Near the end of the 20th century, numerous WIG craft concepts were envisioned to be the solution to faster and cheaper civil sea transport. The RFB X-113 and X-114 were registered as airplanes, they were perfectly suitable for military use; but for civil applications, the associated regulations and registration rigmaroles at that time would impair the economic feasibility and attractiveness in the market. Hanno Fischer, the then technical director of the RFB WIG program, knew it [21]. In 1979, he founded the R&D company Fischer-Flugmechanik (FF) and designed the AirFish series with the idea of registering them as boats. From 1979 to 1992, three iterations were built by RFB and tested for seaworthiness consecutively. The project came to a sudden halt with the downfall of RFB [21]. Until 2003, the International Maritime Organization (IMO) officially classified WIG craft as a high-speed maritime vessel [22] and dedicated regulations to the technical, legal, and safety aspects of the technology, helping accelerate the commercialization of modern WIG vehicles. Singaporean company WigetWorks picked up the fourth generation AirFish (AF8) project from Australian investors, and successfully registered it under the Singapore Registry of Ships in 2011. Figure 1–3 (a) and (b) show the AF8 in flight, and its general arrangement and dimensions can be found in Figure 1–4. As a modern derivative of the X-112 series, the AF8 was built to adhere to the IMO guidelines. It adopted the reverse-delta planform with 27.5% of the wing removed from the

trailing apex, unlike the X-112 family that used a full RDW. The planform has a 20° anhedral and two back-swept fins carrying ailerons inclined at roughly 64° upward from the wingtips. With a 15-meter wingspan, it operates at a height of 3-7 meters above the water without leaving the GE zone. The 1.4-by-4-meter cabin can seat up to 10 passengers. Powered by a 500 Hp V8 engine and two four-blade fixed-pitch fans, it travels at up to 200 km/h, which is fivefold the speed of typical cruise ships and two times faster than hydrofoil crafts or hovercrafts. The proven seaworthiness and demonstrated economical and aerodynamic efficiencies of the AF8 make it a promising candidate for the future of sustainable marine transportation. Currently WigetWorks is working with the National University of Singapore to develop scalable models [4].

The AF8 is not alone in the commercial WIG vehicle market. The collaborative efforts of the German Federal Ministry of Education and Research and FF led to the Hoverwing 2VT in 1997, a scaled down version of the projected 80-seat vessel (Hoverwing 80) also based on the Lippisch-type configuration and Hoverwing Technology. It used a retractable skirt between the two main hulls to create a static “air cushion” to assist take-off. With many successful sea trials in the Baltic Sea, South Korean company Wing Ship Technology Corp. built the WSH-500 (Hoverwing 50) in 2011, boasting a capacity of 50 passengers (Figure 1–3 (c)). A 150-seater version is in motion. Most recently, in 2015, the Chinese Hainan Yingge WIG Manufacturing Co. was readying the production of the CYG-11, a 10-seater WIG craft with a spanwise cropped RDW planform and two rectangular wings as shown in Figure 1–3

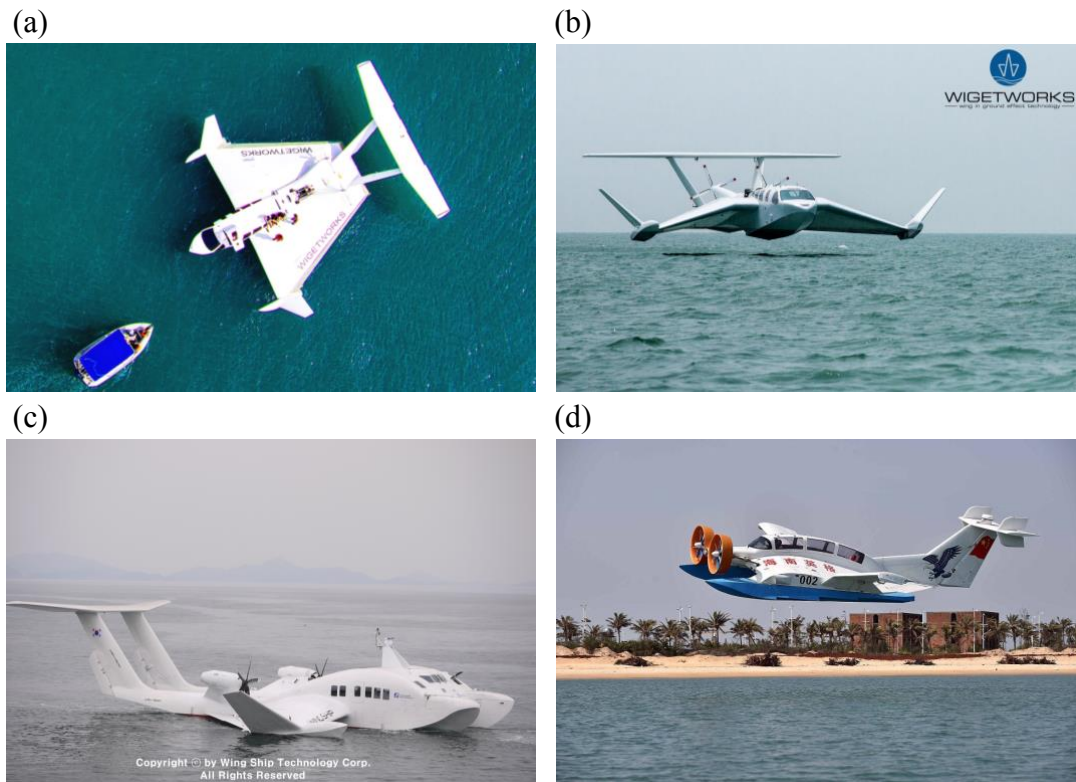


Figure 1-3: Most recent WIG crafts: (a)-(b) AirFish-8 of Singapore in flight[4], (c) WSH-500 of South Korea [5], (d) CYG-11 of P.R. of China [6].

(d), resembling a part Lippisch-type, part Ekranoplan design. The development of larger models is expected to achieve a seat capacity of 50-120 passengers [6].

1.2 Motivation

In spite of the success and long R&D history of the Lippisch-type WIG crafts, very little archived information on reverse delta wings is publicly available, in contrast to the copious studies of rectangular wings and slender delta wings. To the best of the author's knowledge, less than 20 articles relating to RDWs have been published since 2011. This project aimed to further expand on the understanding of

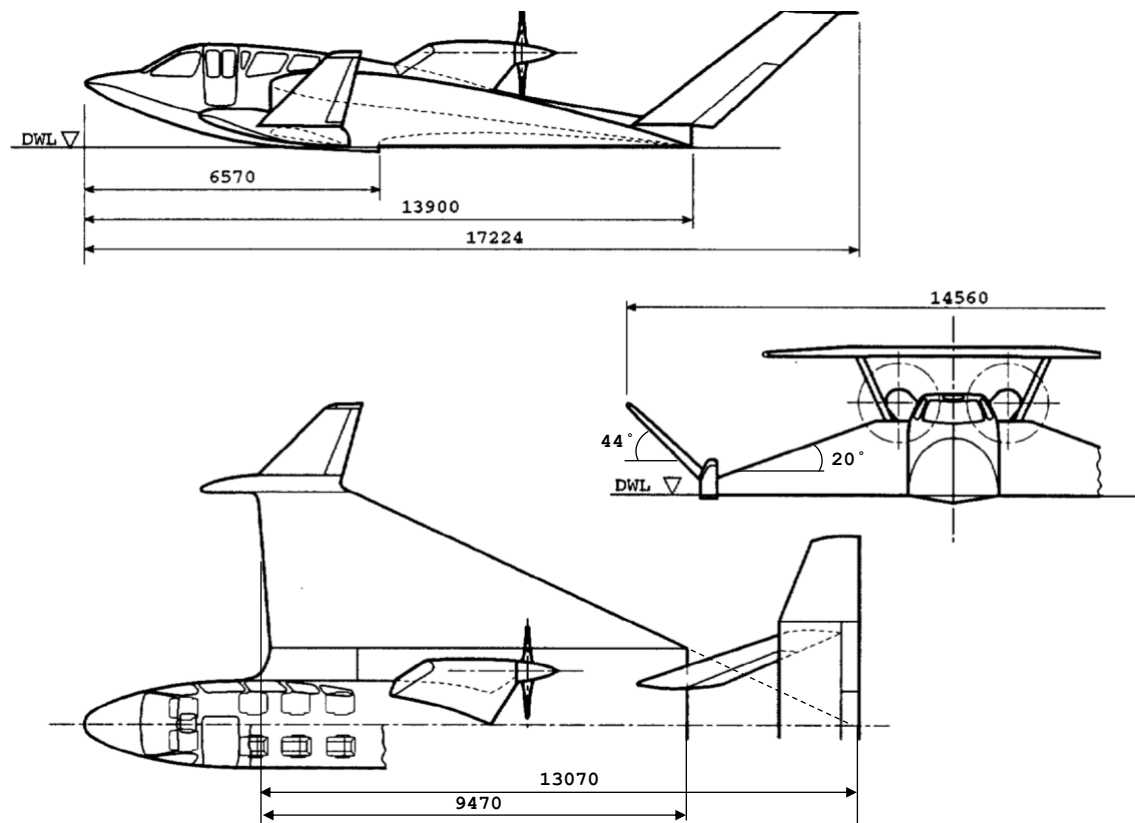


Figure 1–4: Schematic diagrams of the AirFish-8 (Flightship-8) [7].

the wingtip vortex characteristics and aerodynamic performances of a slender reverse delta wing outside GE. The main focus was placed on the effect of the trailing-apex cropping, wing anhedral, and the aileron-equipped winglets, all of which are conscious design elements of the AF8's reverse-delta planform. Gurney flaplike side-edge strips were also investigated as a lift augmentation device that can potentially improve the performance of future WIG crafts. The four geometric modifications were employed individually and jointly on a number of RDW models of different configurations. For comparison, a regular delta wing model of the same sweep and size was included in

the experiment. Wind-tunnel flow measurements above and aft the wing models were obtained at a selected angle of attack, as well as supplementary force balance data from zero lift to post-stall. The study will hopefully provide benchmarks to assist experimental and computational studies of RDWs inside GE in the near future.

CHAPTER 2

Literature Review

This chapter aims to introduce some fundamental characteristics of tip vortices and aerodynamic properties of the rectangular and slender delta wings to which the reverse-delta-wing tip vortices can be referred and compared in later chapters. The first section focuses on the universal structure and major properties of axisymmetric tip vortices in the near-wake of NACA-profiled rectangular wings. Discussions on the formation and development of the spanwise flow, axial flow, vortex strength, size and trajectory, as well as lift and induced drag estimation are summarized. The next section briefly highlights the leading-edge-vortex flow patterns and aerodynamics of the slender delta wings. The third section brings forth the existing studies of the reverse-delta-wing generated tip vortices and wing dynamics. Lastly, the chapter is concluded with a brief review of some passive vortex control techniques, in particular lift augmentation via the Gurney flap-like strips.

2.1 Typical Tip Vortex

Vortex Formation

As a byproduct of lift generation, higher pressure below the wing induces the flow to curl about the wingtip into the upper-surface low-pressure region. The process forms a helical structure that entrains the wing wake and propagates downstream [23, 24]. The increasing number of turns tighten and merge into a concentrated region of high vorticity and axial acceleration. The tip vortex continues

to evolve downstream, leaving behind the trailing vortex. The formation is very much focused around the roll-up process. The sketch on the right (Figure 2-1) shows that while the process generates two individual vortices with opposite senses of rotation at each wingtip, the flat region of the vortex sheet is not disrupted. It bridges the vortex pair and continually feeds vorticity into the vortex system. The roll-up propagates for tens and hundreds of chord lengths downstream ($x/c > 10^2$) of the trailing edge before it is considered complete. Phillips [23] defined that the completion occurs when irrotational fluid fully surrounds the merged region. The development of the vortex in this specific range, termed the near-field, determines the trailing vortex characteristics in the far field and has been the main focus in most studies.

Cross-stream Flow

Under realistic flight conditions, the Re reaches upwards of millions, and the trailing vortex is likely a turbulent flow [23]. Phillips [23] argued that the ever-tightening turns of the spiral structure merge in the centre to form a vortex with a smooth vorticity (ζ) distribution due to viscous diffusion and turbulent effects, while

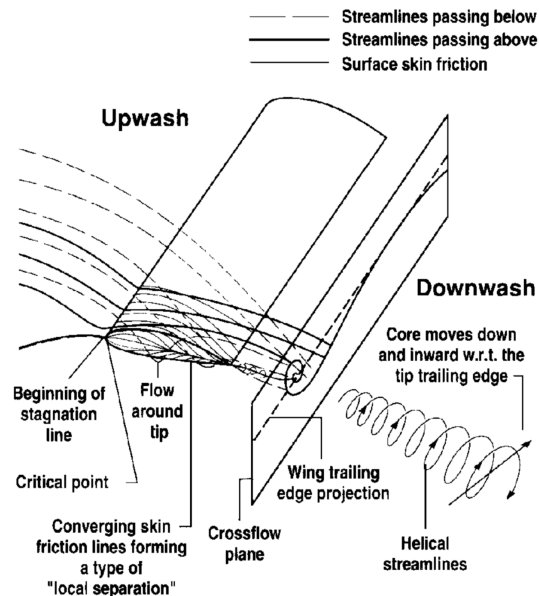


Figure 2-1: Illustration of initial tip vortex roll-up [8].

the outer region can still be comprised of discrete turns. He dissected the merged region into three distinct regions. The innermost area retains a highly viscous core that brings the rotational momentum down to zero near the centre. At a certain radius, it is surrounded by a thin layer of low viscous fluid where the rotational velocity peaks ($v_{\theta peak}$). Outside that are the discrete turns of the spiral structure being merged into the core and the discrete velocity distribution is smoothed out and made continuous by diffusion. This multi-structure vortex model has been widely adopted. Now many studies consider Region III the overall size of the vortex, defined by the outer radius, r_o , and Region II the core radius, r_c , outlined by the peak tangential velocity, $v_{\theta peak}$.

Shear layer carrying high cross-stream vorticity is entrained into the spiral structure immediately after the trailing edge. The vorticity level quickly intensifies and concentrates around the vortical axis where vorticity is the highest (ζ_{peak}). Ramaprian and Zheng [25] conducted the scan of a NACA 0015 half-wing with a blunt or square tip in the immediate near-wake from $x/c = 0.16$ to 3.3. The experiment used laser doppler velocimetry and fine water particles. It was observed that the shear layer shed off of the trailing edge mixed into the spiral structure and brought in high cross-stream vorticity. At a 10-degree angle of attack ($\alpha = 10^\circ$), the roll-up was immediate at $1/3c$ after the trailing edge, and as it progressed downstream, the cross-stream vorticity components diminished in the centre, and the resultant component of vorticity was nearly pure axial.

$$\zeta = \zeta_x = \frac{\partial w}{\partial y} - \frac{\partial v}{\partial z} \quad (2.1)$$

The authors went on to conclude that the dominance of the axial or streamwise vorticity in the core radius spread to the entire vortex for $x/c > 3$. Viscous diffusion led to nearly uniform spacing of the vorticity contours, and ζ was found to be mostly concentrated within a radius of $0.15c$ from the vortex centre. Four major factors were considered to competitively affect the peak vorticity level in coexistence. The continuous vorticity-trapping and feeding in the roll-up process and vortex stretching enticed by any axial pressure gradient help increase the maximum vorticity, meanwhile, the viscous and turbulent effects could cause diffusion and instability in the vortex and result in limited maximum vorticity [25].

The shear-layer roll-up starts early along the free end of the wing. Chow et al. [8] reported the sign of high-crossflow velocity circumventing the tip at $x/c = -0.59$ on a 4-foot-chord NACA 0012 half-wing model with a rounded tip at $Re = 4.6 \times 10^5$. The first indication of tip vortex was observed at $x/c = -0.394$ where small pockets of low-crossflow velocity fluid appeared between the feeding vortex sheet and the main vortex. The main vortex and smaller secondary vortices were present at $x/c = 0.5$ (leading edge set as origin) reported by Birch et al. [26] who used a square-tipped NACA 0012 wing at $Re = 2.01 \times 10^5$. The main vortex gained more strength progressively and eventually entrained the secondary vortices [26]. Further downstream, a near axisymmetry was observed one chord behind the trailing edge according to Ramaprian and Zheng [25], verified by Birch et al. [26] who reported that the vortex core started to exhibit axisymmetry from $x/c = 1.5$ relative to the leading edge. Aside from qualitatively trying whether the vorticity contours appear circular and evenly spaced, the axisymmetry can also be quantifiably justified by the

distribution of circumferentially averaged tangential velocity across the vortex. The cross-stream Cartesian velocity vectors v, w , at each data point are first transformed into tangential velocity vectors, v_θ, v_r , in polar coordinates. The mean tangential velocity is then obtained at each corresponding radius from the axis, as long as the vortex resembles a nearly circular shape. As discussed earlier, the highly viscous core renders the tangential velocity zero at the vortical axis. Away from the centre, v_θ climbs to a peak ($v_{\theta peak}$) at the boarder of the core, then quickly plunges and approaches zero asymptotically in the outermost free stream. As expected, v_θ changes sign from negative to positive when traversing across the vortex from inboard to outboard [26]. Vortex axisymmetry is said to be established when the tangential speed reaches its maximum at the same radius on both sides of the distribution curve, in other words, when $|v_{\theta max}| = |v_{\theta min}|$, or when the streamwise vorticity distribution curve displays the Gaussian distribution.

The peak streamwise vorticity, ζ_{peak} , increased up until $x/c = 0.9$ and fell back within half a chord after the trailing edge of the NACA wing, and for $x/c > 1.5$, both ζ_{peak} and $v_{\theta peak}$ decayed slightly with x/c . However, with increasing angle of attack both values rose almost linearly until stalling, due to the increasing vorticity-feeding from the continuous roll-up of the shear layer [26, 27].

Axial Flow

Batchelor [24] studied axisymmetric laminar vortex, he argued that the radial and tangential flow components create a radial pressure gradient that balances the centrifugal force, and a change in the azimuthal direction produces an axial pressure gradient that consequently leads to axial acceleration or deceleration. Batchelor [24]

provided an equation for axisymmetric vortex in laminar flow to demonstrate the relationship between the axial velocity, u , and free-stream velocity, U .

$$u^2 = U^2 + \int_r^\infty \frac{1}{r^2} \frac{\partial \Gamma^2}{\partial r} dr - 2\Delta H \quad (2.2)$$

The partial derivative of the square of circulation (Γ) with respect to the vortex radius (r), $\partial \Gamma^2 / \partial r$, in the second term of the right-hand side is positive, and the total head loss (ΔH) is not a dominant term at any rate of a typical tip vortex, thus the axial velocity in the vortex core is larger than U , possibly by a significant amount. The axial velocity is jet-like at the axis and monotonically decreases to U once away from the axis. It is also stated that further downstream the decay of the swirling motion eventually should lead to a recovery of the pressure deficit in the vortex core and drop the core axial velocity, u_c , close to the free-stream value.

The normalized maximum axial velocity recorded by Chow et al. [8] was 1.77, immediately upstream the trailing edge ($x/c = -0.005$). Over half a chord downstream, that number dropped gradually to 1.69. In comparison to this result, obtained from a round-tipped NACA 0012 half-wing at $\alpha = 10^\circ$, Chigier and Corsiglia [28] tested a similar wing at a 12-degree incidence and double the Re and reported a lower maximum value of 1.4 for the axial velocity, which then decreased to 1.1 immediately after the trailing edge. Nonetheless, both tests demonstrated a jet-like core flow as a result of the favorable axial pressure gradient induced by the high crossflow in the core. The authors attributed the high axial flow to the relatively high Re , the rounded wingtip and high angle of attack. On the other hand, Ramaprian and Zheng [25] reported a wake-like core of $u_c/U = 0.8$ with a square-tipped NACA half-wing

at $Re = 1.8 \times 10^5$. In the light of the conflicting results about the core axial flow and the mechanism that determines the jet-like or wake-like behaviour, many speculated that the Reynolds number and tip conditions were responsible. Lee and Pereira [27] pointed out that the rounded tip did produce higher u_c than the blunt tip but did not affect the overall vortical flow patterns. They showed for a square-tipped NACA 0012 half-wing, the angle at which the fluid inside the vortex core changed from wake-like to jet-like was around 7° . For $\alpha < 7^\circ$, the fluid's momentum was low and the wake turbulence was high enough to access the jet-like core developed upstream, causing the jet flow to dissipate and turning into wake-like. When $\alpha > 7^\circ$, the jet-like pocket was surrounded by the shear layers which protected it from viscous diffusion and the wing wake. The jet-like core originated from the free stream was sustained with a slightly reduced magnitude in the near wake. The nature of the wake-like or jet-like axial flow ultimately depends on the interaction between the tip vortex and the wing wake [27].

Vortex Strength and Circulation

The vortex strength is measured by the flux of vorticity in the closed surface area of the vortex on a crossflow plane, namely the circulation. The vortex becomes stronger as more vorticity is added in by the roll-up and reattachment of the shear layer, and it's reflected in the increase in circulation in the near wake. For the NACA 0015 wing at $\alpha = 10^\circ$, it appeared that the total circulation, Γ_o , increased quickly, plateaued and did not vary with x/c in the near wake for $x/c > 1.5$, implying that the roll-up process was nearly complete half a chord behind the trailing edge [26, 27]. This was further supported up by the fact that the core circulation, Γ_c , also was

seen with the similar trend, levelling out at roughly 75% the total circulation [26]. A nearly linear proportionality to increasing angle of attack exists for circulation, similar to the peak values of vorticity and tangential velocity.

Gerontakos and Lee [29] studied the aerodynamic performance of a cambered NACA 0012 wing for $2.5 \times 10^5 < Re < 1 \times 10^6$. They estimated the lift using the integral of spanwise circulation ($\Gamma(z)$) of the near-wake data.

$$C_l = \frac{L}{\frac{1}{2}\rho U^2 c} = \frac{\rho U \int_{-b/2}^{b/2} \Gamma(z) dz}{\frac{1}{2}\rho U^2 c} = 2 \int_{-b/2}^{b/2} \frac{\Gamma(z)}{Uc} dz = 2 \frac{\Gamma_o}{Uc} \quad (2.3)$$

The sectional lift coefficient C_l turns out to be just two times the normalized total circulation, Γ_o/Uc . The result of the circulation-based integral method agreed well with the measured lift from force balance, illustrating that the total circulation of the vortex in the near wake can represent nearly all of the total lift at all levels of Re below 10^6 , deeming it a respectable method of estimating lift forces generated by rectangular wings.

Vortex Size

Lee and Pereira [27] reported a vortex core radius, r_c , of 3.8% c at $\alpha = 5^\circ$ and 5.5% c at $\alpha = 10^\circ$ on the square-tipped NACA 0012 wing. Others have recorded very similar results, such as Birch et al.'s $r_c = 6\%c$ of a NACA 0015. For the overall vortex radius, r_o , Birch et al. [26] recorded $r_o/c = 0.1$ at 10° of incidence, making the ratio of core radius to outer radius $r_c/r_o = 60\%$. While α increased, the vortex size also increased as it is influenced by the increasing thickness of the shear layer during roll-up [25]. Nonetheless, vortex radius did not seem to have a clear dependence on

the vortex strength or circulation, in spite of the significant increase in the circulation with increasing α [26]. Last but not least, r_c/r_o dropped as Re increased [29].

Vortex Trajectory

Chow et al. [8] observed that the vortex has an upward and slightly outboard movement, so did Lee and Choi [30]. While Chow et al. [8] believed that the shift in the vortex trajectory was an inviscid effect from the tunnel walls, Lee and Choi [30] said that it was the influence from the low-pressure viscous wake. However, Ramaprian and Zheng [25] reported an upward but inboard movement by comparing two cross-stream velocity contours at $x/c = 0.67$ and 1.67 , arguing that the shear layer arriving from the inboard regions added more spanwise vorticity into the outer layers of the vortex, inducing the inboard movement.

Lift-induced drag

Birch et al. [26] computed the induced drag of the NACA 0015 wing at $Re = 2 \times 10^5$ via two methods, the Kusunose wake integral method [31] and Maskell's wake model [32], shown in Equations 2.4 and 2.5 respectively.

$$D_{i,Kusunose} = \iint_{S_2} \frac{1}{2} \rho (v^2 + w^2) dydz \quad (2.4)$$

$$D_{i,Maskell} = \frac{1}{2} \rho \iint_{S_\zeta} \psi \zeta dydz - \frac{1}{2} \rho \iint_{S_1} \phi \sigma dydz \quad (2.5)$$

Kusunose [31] showed that the induced drag generated by a finite wing can be expressed in terms of the swirl velocity field in a downstream plane S_2 as seen in Equation 2.4 above. In the second equation, Maskell's method decomposes a selected crossflow plane S_1 into a stream function ψ and velocity potential function ϕ , each multiplied with the vorticity $\zeta = \partial w / \partial y - \partial v / \partial z$ and a source term,

$\sigma = \partial v/\partial y - \partial w/\partial z$ [32]. The two methods yielded nearly identical results given that the vortex was axisymmetric with negligible streamwise velocity gradients. The induced drag coefficient C_{Di} ($= D_i/(1/2\rho U^2 S)$) increased dramatically with increasing α until the static-stall angle, α_{ss} , but was under 20% of the total drag coefficient C_D of the force-balance results [26]. For $Re < 10^6$, the C_{Di} was generally larger at higher Re , reported by Gerontakos and Lee [29].

2.2 Delta Wing

Delta wings have populated the design of most military supersonic aircraft. Today, applications for delta wings have spread to small-scale unmanned aerial vehicles (UAVs), micro aerial vehicles (MAVs), tip vortex modification and control, etc. Despite their supersonic flight capabilities, fighter jets fly at medium to high subsonic speeds over majority of their air time, for which delta wings in subsonic flow deserve much attention. Among the triangular planforms, the most commonly seen is the slender type with high sweep angles ($\Lambda \geq 55^\circ$) and sharp leading edges. The engendered low aspect ratio gives slender delta wings a small lift curve slope and a moderate maximum lift coefficient. Two counter-rotating conical flow patterns over the top of the wing generate nonlinearly increasing suction with angle of attack, which ensures a high stall angle, as well as an inevitable drag component. Consequently, the lift-to-drag ratio is not as high as most conventional rectangular planforms. This section primarily looks at the development and characteristics of the leading-edge vortex over sharp-edged slender delta wings in the low subsonic speed range. The vortex structure and flow characteristics before and after the vortex breakdown, the nonlinear vortex lift, and the prediction of lift and drag are covered.

Leading-edge Vortex Structure

At very low angle of attack, flow over the delta wing is attached over the entire chord. As the angle increases, the flow on the pressure side of the wing moves outboard and curls inboard but often separates at the sharp leading edge. The separated shear layer curves inboard and rolls into a pair of counter-rotating streamwise LEVs with high vorticity and axial flow in the core. Typically, the shear layer reattaches to the upper surface and induces an outboard spanwise flow towards the leading edges, forming small secondary vortices between the larger and more dominant LEVs and the wing. These secondary vortices, rotating in opposition to the LEVs, have the effect of keeping the primary vortices upwards and inwards [9,33]. Such flow structure is illustrated in Figure 2-2 (a) by Nelson and Pelletier. Flow visualization (Figure 2-2 (b)) reveals that the LEVs appear as two conical jets originating from the front apex and jetting downstream closely to the upper surface. Their trajectory is linear and position persistently inboard of the leading edges. The reattachment of the separated shear layer can occur easily at low angles of attack, but the reattachment location shifts inboard with increasing α until the shear layer from each side meet at the centreline of the wing. Reattachment is no longer attainable at this critical angle, and the LEVs are squeezed towards the centreline, as well as upwards, away from the wing surface, as demonstrated in Figure 2-2 (d). An increase of the sweep angle has the equivalent effect on the reattachment of the vortex sheet. One of the first to study the vortex structure of LEVs was Earnshaw [34] who theorized the vortex structure with three distinct substructures: a viscous sub-core, vortex core, and discrete turns of the vortex sheet. Nelson and Pelletier [9] later refined

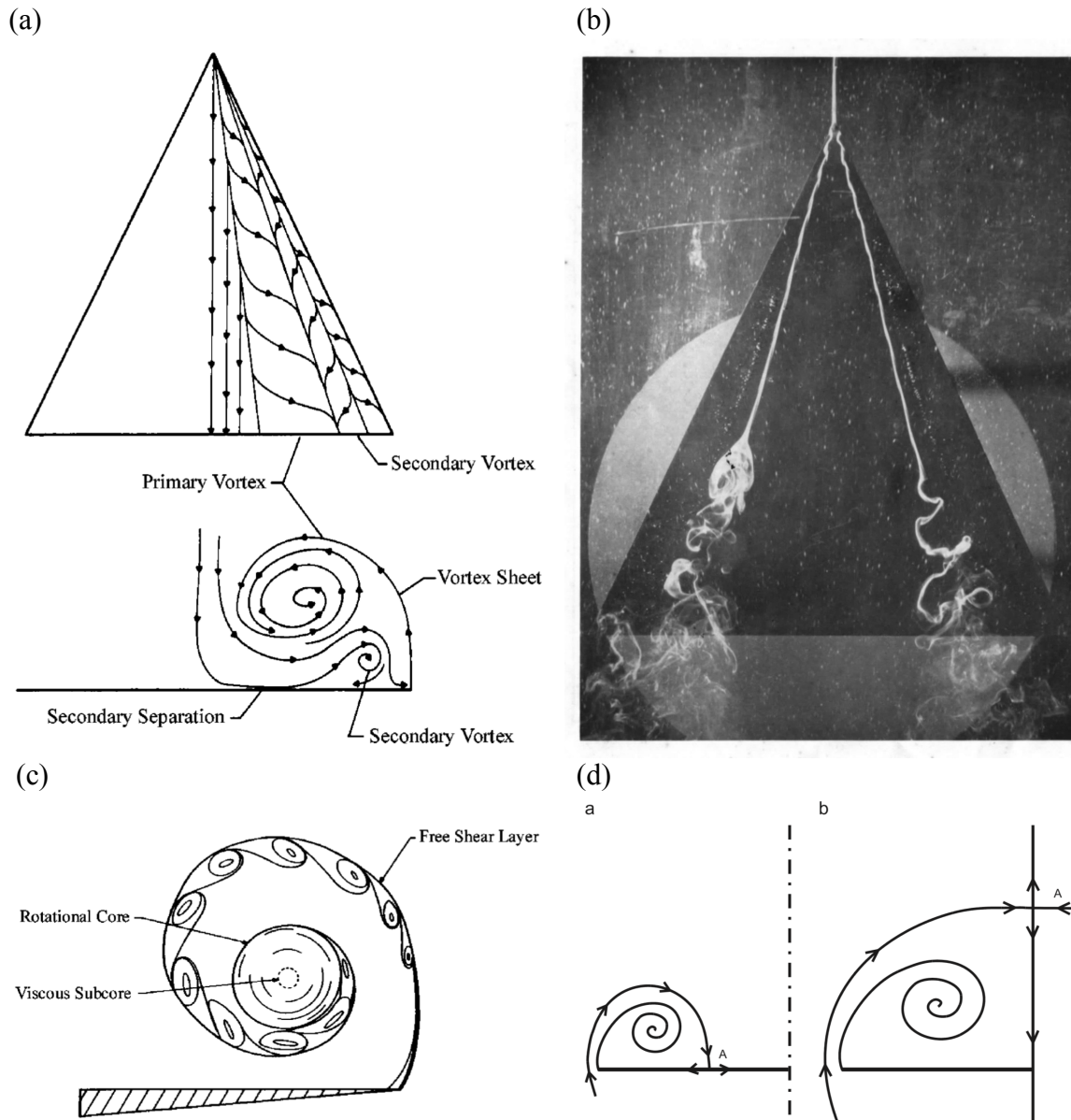


Figure 2-2: Leading-edge vortex (LEV) structure on slender delta wings. (a) Sketch of the LEVs over a slender delta wing [9]; (b) filaments of dye flow over a 65° delta wing at 2 inch/sec [10]; (c) three regions inside a LEV [9]; (d) reattachment location of different delta-wing sweep angles [11].

the structure model based on Earnshaw's concept and others'. A sketch of such is shown in Figure 2-2 (c) below. Similar to a tip vortex, the free shear layer curls into a spiral structure with a discrete number of turns in the outer layers and a well merged core. The rotating core is conical in nature with a diameter roughly 30% of the local semi-span ($r/s = 0.15$), which environs a small ($r/s = 0.025$) but highly viscous core that contains large pressure and velocity gradients. The axial flow of the sub-core is accelerated to over double the free-stream speed and its circumferential velocity nearly as high as the free-stream [34]. The appreciable axial acceleration in the core region leads to favorable low pressure over the wing that gives rise to additional suction/lift, namely the vortex lift. Vortex lift can contribute up to 30% of the total lift of a delta wing [33]. Specifics of the vortex lift are discussed in later subsections. Nonetheless, lift generation of delta wings is not free of impediment, as it is often limited by the phenomenon of vortex breakdown.

Vortex Breakdown

As the LEVs shelter high axial and circumferential velocities in the core and carry those downstream, at a certain chordwise location, the vortices experience an abrupt "burst" or expansion accompanied by dramatic changes to its flow characteristics. Increase in vortex diameter, decrease in the core axial and circumferential velocities, loss of lift and reduction in nose-down pitching moment are clear signs that characterize the bursting phenomenon, termed vortex breakdown [33]. The breakdown is complex and hardly predictable through analytical methods, but thanks to the large collection of experimental data, it is fairly well understood in terms of its position of occurrence and effects on the flow structure and wing loads. Upstream

of breakdown, the vortex appears as a fine jetting spiral gradually expanding in size, upon breakdown, the spiral quickly loses its coherent structure and diffuses into a turbulent flow. There are two possible types of breakdown over a delta wing, the bubble type, which occurs most of the time, and occasionally transitions into the spiral type [9]. Depicted in the dye injection photograph by Lambourne and Bryer [10] (Figure 2-2 (b)), in the bubble type located in the lower vortex, the core seems to expand around an ogival recirculation zone, then exits in the form of donut-shaped vortex rings that diffuse into a turbulent wake. The recirculation zone disappears in the spiral-type breakdown, where the core flow retains the discrete spiral structure and corkscrews into a turbulent wake, seen in the upper vortex in Figure 2-2 (b). A number of theories have attempted to explain why breakdown occurs, amongst which Hall [35] contributed convincing remarks about the process. He suggested that the occurrence of the local swirl exceeding a certain threshold will lead to a local retardation of the axial flow in the core, accentuating asymmetry and causing the abrupt vortex breakdown. Now it's widely acknowledged that both the swirl level and pressure gradient affect the occurrence and movement of breakdown. An increase in either parameter promotes breakdown and drives breakdown position upstream. Moreover, it is noteworthy that the two parameters also depend on wing geometry such that changes in the angle of attack and sweep can alter the breakdown location [36].

Wentz and Kholman [37] studied the chordwise progression of vortex breakdown for $45^\circ < \Lambda < 85^\circ$ over a large spectrum of incidence angles at $Re = 10^6$. It was discovered that a pressure increase in the flow direction along the axis is destabilizing,

and a pressure decrease is stabilizing. Based on this concept, the pressure gradient (dP/dx) is zero at the apex, and it reaches maximum at the trailing edge where the vortex first becomes the most unstable. The minimum angle of attack at which vortex breakdown takes place at the trailing edge, termed “vortex breakdown at trailing edge”, was reported for delta wing models with sweep angles ranging from 60° to 85° . For $60^\circ \leq \Lambda \leq 75^\circ$, the breakdown angle increased with increasing sweep. Surprisingly, the breakdown angle was nearly independent of sweep for very slender wings ($\Lambda \geq 75^\circ$), at a virtually constant value of around 37° , which also marked the stall angle. To an extent, the results proved that vortex breakdown is largely responsible for the lift loss on slender delta wings. As for non-slender wings ($\Lambda \leq 55^\circ$), breakdown occurred much further upstream of trailing edge at low angles of attack due to steeper adverse pressure gradients at the trailing edge, compelling the breakdown location upstream.

Leading-edge Vortex Parameters

Nelson and Visser [33] investigated the distribution of vortical flow parameters in a chordwise progression on a 70° and 75° delta wing at $Re = 2.5 \times 10^5$. The study offered insights into the dependence on the wing geometry, and more importantly, the effect of breakdown on the vortex circulation, vorticity, and velocities. A dramatic reduction was seen in both the core axial velocity, u_c/U , and peak streamwise vorticity, $\zeta c/U$, at $x/c = 0.50 - 0.55$, where breakdown was expected for the 70° wing at $\alpha = 30^\circ$. From the vorticity distribution belt-curves of different chordwise stations, ζ_{peak} enlarged with chordwise location, and reached a maximum at $x/c = 0.411$ before entering the breakdown region. Upon arriving at the breakdown,

the peak level declined quickly, associated with a widening of the vortex core. In the azimuthal direction, spanwise vorticity maintained a more or less constant value upstream of the breakdown location, then turned negative in the breakdown region [33]. Similar observations were found with the axial velocity distribution of this wing configuration. Upstream of breakdown at $x/c = 0.412$ and 0.448 , u_c was strong jet-like, covering nearly 50% of the local semi-span ($r/s = 0.5$). At $x/c = 0.484$, the core flow experienced deceleration, showing the first sign of breakdown closely aft of this station. After breakdown, for $x/c > 0.521$, the axial velocity transforms into a wake-like deficit with the core diameter of roughly 30% of the local semi-span, which continued to broaden downstream [9].

The nondimensionalized circulation, Γ/cU , calculated based on $r/s = 0.25$, scaled with the local semi-span and grows in a virtually linear fashion in the chordwise direction. In terms of the sweep angle, the circulation of the 70° wing was stronger than that of the 75° wing at $\alpha = 30^\circ$ [33]. This supports the earlier remark by Wentz and Kohlman [37] that breakdown on lower sweep wings occur closer to the apex as a result of not only the larger adverse pressure gradient, but also the increased vortex strength.

Peak tangential velocity, $v_{\theta peak}$, reaches $1.5U$ before breakdown with steep velocity gradients concentrated in the viscous sub-core, whose diameter is defined by the spanwise distance between the maximum and minimum tangential velocity, taking up approximately 10% of the local semi-span ($r/s = 0.05$). Following breakdown, $v_{\theta peak}$ was reduced, and the sub-core radius swelled significantly to around $r/s = 0.25$ at $x/c = 0.594$. Besides the viscous sub-core, Nelson and Visser [33] also reported

the chordwise progression of a larger jet-like core, computed based on $u_c/U \geq 1.5$. Radius of the jet-like core grew linearly downstream, so did the smaller sub-core, however, at a much lower rate. As α went up, the core radius increased gradually due to the continuous feeding of vorticity from the separated shear layer.

Lift and Drag Prediction

The method developed to predict the lift of sharp-edged wings centers around the prediction of the nonlinear vortex lift spawned by the additional suction pressure from the LEVs. For flow curving around the leading-edge of a large radius, the suction force acts against inertia to keep the flow attached around edge. Polhamus [38] argued that for the separated flow around a sharp leading edge, the suction force exerted at the edge is converted to a force normal to the upper surface in order to sustain the vortex flow structure. Assuming zero leading-edge suction, Polhamus formulated the lift over a sharp-edged delta wing as the following:

$$C_L = K_p \sin \alpha \cos^2 \alpha + K_v \cos \alpha \sin^2 \alpha \quad (2.6)$$

This simple mathematical equation considers the total lift as the sum of the potential-flow lift and the nonlinear vortex lift, where K_p is the potential-flow lift coefficient, solely dependent on the wing planform, and K_v is the vortex lift coefficient, relatively invariant of sweep for a conventional delta wing. Traub [39] later expanded the formulas for K_p using an updated spanwise circulation distribution that incorporates leading-edge vortex separation.

$$K_p = 4 \tan^{0.8}(\pi/2 - \Lambda) \quad K_v = \pi / \sin \Lambda \quad (2.7)$$

Note that the trigonometric terms in Equation 2.6 vary nonlinearly with angle of attack. For a typical delta-wing aircraft ($0^\circ \leq \alpha \leq 35^\circ$), as the angle rises, part of the potential lift is lost as the squared cosine term decreases by a small margin, meanwhile, the vortex lift gains much more lifting force while the squared sine term builds up rapidly at such angles.

Wentz and Kohlman [37] reported that the Polhamus's leading-edge suction analogy is excellent for the lift prediction of sharp-edged wings with medium sweep between 65° and 80° prior to stall. However, it does overestimate lift for very slender wings and relatively non-slender wings, for not taking into account certain phenomena unique to these wing types. Specifically, for the high-sweep wings with Λ above 80° , at even moderate incidence angle, vortex sheet reattachment is not possible. When the two separated vortex sheets meet above the wing's centreline, vertical elongation occurs, pushing the LEVs inboard and upward (Figure 2-2 (d)). This displacement of the suction cores ultimately results in a significant reduction in the vortex lift. On the non-slender wings, when $\Lambda < 65^\circ$, the vortex stream exits the wing obliquely to the trailing edge. The sudden change in geometry interrupts the vortex from achieving full suction [37]. Coupled with the steeper adverse pressure gradient on these higher aspect-ratio wings, vortex-lift generation becomes futile, and breakdown occurs much closer to the apex.

Aside from lift prediction, it is also proven that using the streamwise component of the normal force given by Polhamus's method can predict the drag force satisfactorily over a wide range of angles of attack. When the angle of attack increases

beyond the occurrence of C_{Lmax} , the normal force method underestimates the actual drag due to negligence of the rising parasitic drag [37].

2.3 Reverse Delta Wing

From the original “Aerofoil boat” X-112 to its modern successors, the AF8 and WSH500, numerous prototypes and sea trials have proven the reverse-delta coupled with anhedral a successful design for fast and economical long-range travel in the open sea. They also have the stability and versatility to operate over rough waters by flying in ground effect at altitudes of up to half the wing span and some can even perform hydrodynamic “jumps” over obstacles [18]. In recent years, reverse delta wings can also be found in applications ranging from wingtip vortex control [40] to biomimicking MAVs in the shape of butterflies and bats [41]. This section discusses recent studies on slender reverse delta wings with an emphasis on the vortex flow characteristics and aerodynamic performances. In addition, comparisons against the delta-wing counterpart, the effect of wing slenderness and some passive tip-vortex control techniques are briefly reviewed.

RDW Vortex Structure

The flow over a slender RDW with $\Lambda \geq 65^\circ$ is characterised by multiple spanwise vortex filaments (SVFs) on the upper surface and two outboard RDW vortices trailing aft each wingtip along the leading edge, as can be seen in Figure 2–3 (a). The SVFs are formed by the roll-up of the shear layer along the leading edge perpendicular to the free stream, and the RDW vortices originate from the spanwise leading-edge vortex with an approximate diameter of $30\%c$ [12]. Streamwise vorticity contours (Figure 2–4) reveal that the RDW vortex exhibits an “arm-and-fist”

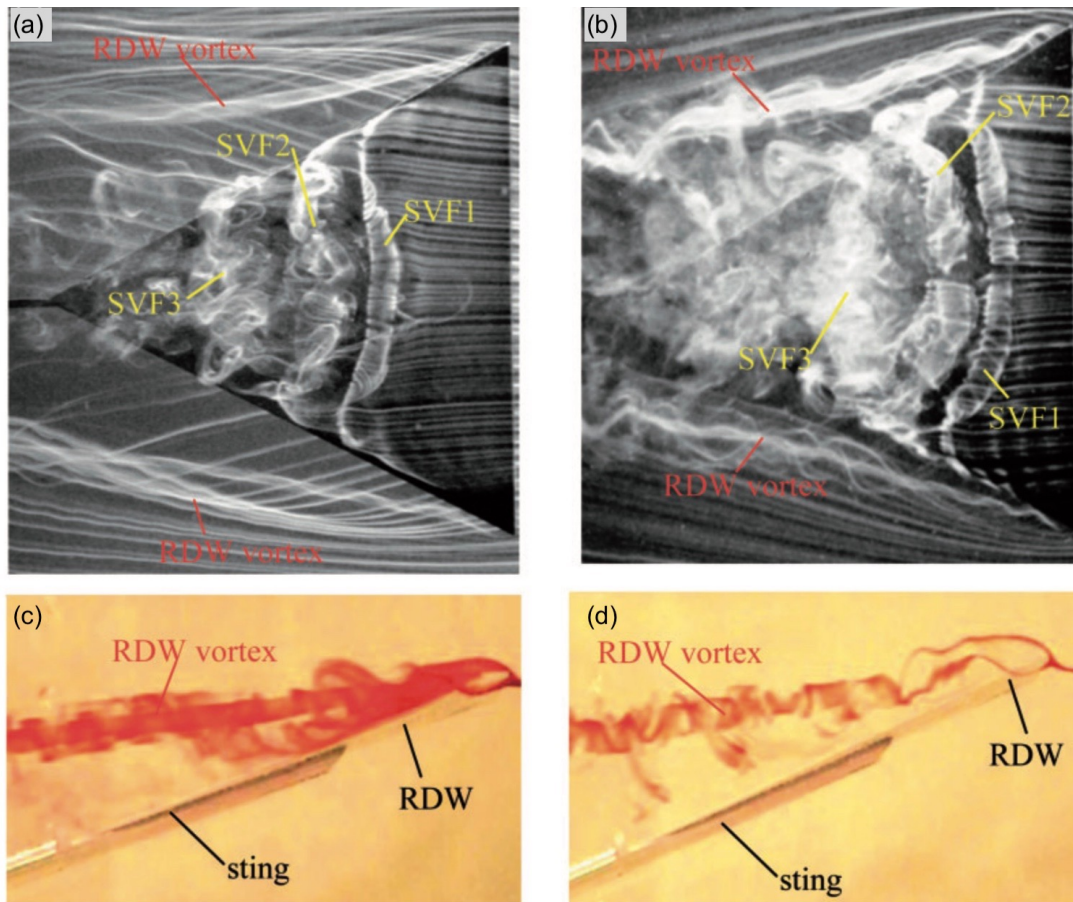


Figure 2-3: Flow visualization photographs of a 65° reverse delta wing (RDW) using smoke-wire (top figures) and dye-injection (bottom figures) techniques. (a) and (c) $\alpha = 14^\circ$ (b) and (d) $\alpha = 20^\circ$. SVF denotes spanwise vortex filament [12].

pattern, which is comprised of the near-axisymmetric vortex and the shear layer escaping outboard from beneath the wing. The “arm” increases in length but decreases in strength as the roll-up process slowly completes downstream. At low angles of attack, the adverse pressure gradients are limited to the trailing apex region, leaving the SVFs well-defined and intact. As the angle of attack increases, high-pressure

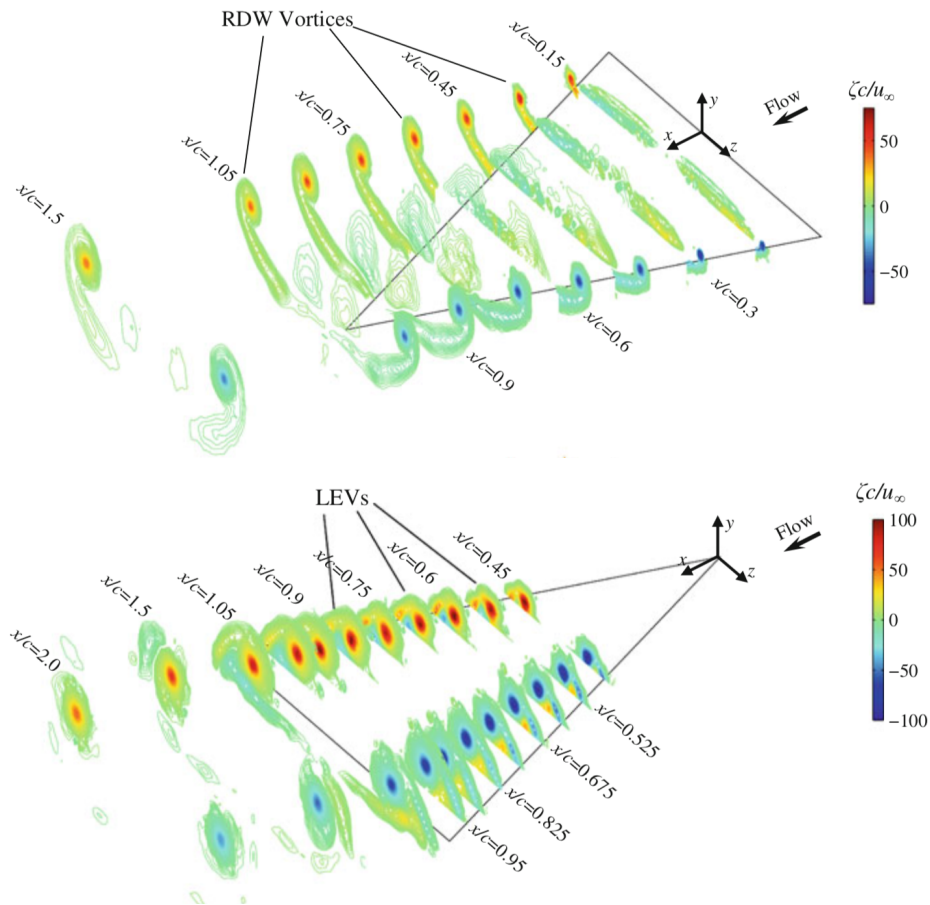


Figure 2–4: Streamwise development of normalized axial vorticity contours of a 65° reverse delta wing (RDW) (top) and delta wing (DW) (bottom) at $\alpha = 12^\circ$ [13].

flow escapes from the trailing edges and destabilizes the SVF closest to the trailing apex (Figure 2–3 (b)). The disruption of the SVFs propagates upstream in response to the stronger pressure gradient at higher angles of attack, and the interaction with the boundary layer further deteriorates the overall SVF structure. Approaching the stalling angle, the separated SVFs generate large wake on the top surface, accompanied by the diffusion of the RDW vortices. Lee and Ko [12] concluded that the

stalling of RDW is triggered by the breakdown of the SVFs and the lift generation primarily relies on the pressure side of the wing.

RDW Vortex Flow Characteristics

Lee and Ko [12] used particle image velocimetry (PIV) to study the vortical flow of a 65° RDW model made of thin flat-plate steel sheet with square edges at $Re = 1.1 \times 10^4$. Measurements of a 65° DW model of the same size and material were taken for comparison. At a fixed α and x/c , RDW vortices were weaker and less concentrated than the LEVs on the DW. Supported by several authors [12, 13], the streamwise vorticity and tangential velocity levels of the RDW vortices are lower than the LEVs of the DW. For a 75° -sweep RDW, at $\alpha = 20^\circ$ and $x/c = 1.359$, $v_{\theta peak}$ of the RDW vortex was approximately half that of the LEV, and r_c twice the size of the LEV [42]. It was shown by [12] that in the RDW vortices, ζ_{peak} and $v_{\theta peak}$ arrived at a maximum at $x/c = 0.2$, both then declined in a virtually linear fashion with increasing x/c . Beyond $x/c = 0.7$, the coinciding location of ζ_{peak} and zero v_θ was believed to indicate that the roll-up was close to completion inside the vortex. Meanwhile, the vortex displayed axisymmetry observed through the Gaussian vorticity distribution curve and the $v_{\theta max} = |v_{\theta min}|$ relationship of the tangential velocity curve. Total circulation, Γ_o , calculated using Stokes' theorem, increased quickly with x/c and levelled off for $0.7 \leq x/c \leq 1.5$, validating the near completion of the shear-layer roll-up in the core region. For the DW vortex, Γ_o plateaued much later at $x/c \geq 1.1$ and the axisymmetry was not observed until $x/c \geq 1.5$.

Lee and Su [13] conducted near-wake measurements of a 65° RDW with beveled edges at $\alpha = 12^\circ$ and $Re = 2.45 \times 10^5$ with a seven-hole pressure probe. They reported that the RDW vortex core flow changed from wake-like aft the leading edge soon to weak jet-like ($u_c/U = 1.06$) after $x/c > 0.5$, and such core speed was maintained at downstream stations. In contrast, the LEVs on the DW of the same make had strong jet-like core velocity up to $1.55U$ but declined to a wake-like flow in the event of vortex breakdown at the trailing edge.

RDW vortex strength and concentration highly depend on the angle of attack. The RDW vortices were concentrated and axisymmetric in the domain of 0 to 16-degree incidence, in which a rising angle of attack enlarged the ζ_{peak} and $v_{\theta peak}$. For $\alpha > 16^\circ$, the SVF breakdown was apparent on the wing; the axisymmetric structure of the tip vortices began to crumble and the vorticity and tangential velocity decreased at higher α . Past $\alpha = 23^\circ$, the “arm” disappeared, and the “fist” developed into a “weak circulation-like flow with small patches of vorticity” [12]. Despite the weakening vortex strength, Γ_o continued to rise with α and the RDW did not stall until $\alpha = 35^\circ$. Additionally, the local maxima of ζ_{peak} and $v_{\theta peak}$ were seen at $x/c = 0.2$, and Γ_o plateaued for $x/c > 0.7$, regardless of angle of attack. All in all, the deterioration of the vortex strength at moderate incidence does not lead to immediate stalling as the pressure side of the RDW is responsible for lift generation.

Furthermore, the RDW vortices were seen to have an inboard and upward movement following its downstream progression, and such effect was promoted by increasing incidence until $\alpha = 22^\circ$ [12].

RDW Aerodynamic Performances

A 65-degree RDW has an overall inferior aerodynamic properties to its DW counterpart. It was found to produce much lower lift but higher drag polar at roughly a Reynolds number of one third of a million (Figure 2–5). Lee and Su [12,40] argued that the flow structure on the suction side of the RDW was responsible for its less efficient aerodynamics. A visual comparison of the vortex structure of the two wings is shown in Figure 2–4. In particular, the DW was helped by the “energizing vortex-lift generating LEVs” over the top and the RDW had instead persistently outboard RDW vortices that were weaker in normalized ζ_{peak} , $v_{\theta peak}$, u_c and Γ_c . As for the drag polar, for the RDW at medium angles of attack, the disrupted and then separated spanwise vortices over the wing subsequently actuated a large axial wake. On the contrary, attached and concentrated jet-like axial flow was attained in the LEVs on the DW. Altaf et al. [42] noticed that the pressure difference between the upper and lower surface on a 75° RDW was smaller than a DW of the same configuration,

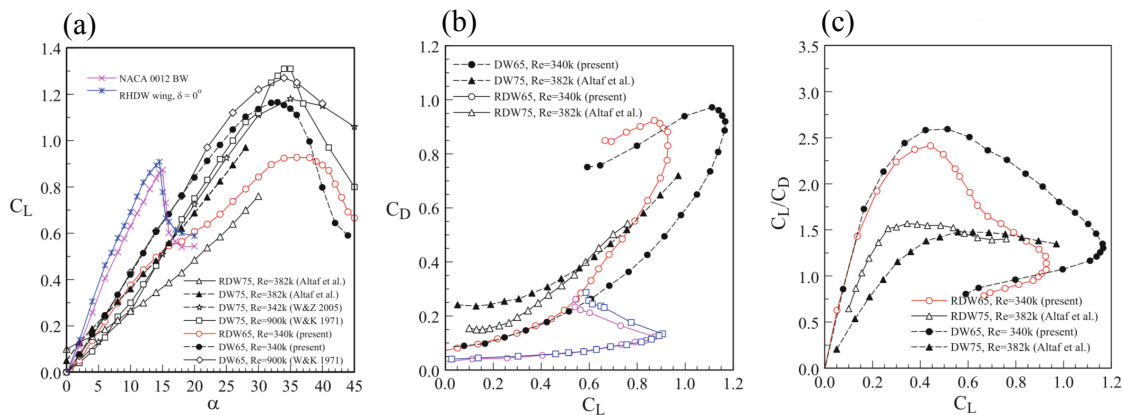


Figure 2–5: Aerodynamic coefficients of reverse delta wing (RDW) and delta wing (DW). DW65 and RDW65 denote 65°-sweep DW and RDW, respectively. (W&Z) denotes (Wang and Zhang) and (W&K) denotes (Wentz and Kohlman). [13]

therefore a lower C_L for the RDW. However, at the same angle of attack, the LEVs give rise to a greater profile drag and thus a larger total drag than the RDW. From force-balance measurements of the 65° -sweep RDW at $Re = 3.3 \times 10^5$, the RDW stalled at $\alpha = 38^\circ$, 5° later than its DW counterpart, and had a smaller C_{Lmax} than the DW [13]. Nevertheless, the RDW achieved inferior L/D values to the DW at both iso- C_L and iso- α conditions [12]. Last but not least, an offset in the roll angle was detrimental to the L/D ratio of a RDW while a DW was practically not affected [42].

Wing Slenderness

RDWs with low sweep angles have also received some attention recently. Lee and Ko [43] discovered that while both the slender (65°) and non-slender RDW (50°) generated less lift compared to their DW counterparts, the non-slender RDW had even inferior lift to the slender one. The vortex flow on a non-slender RDW includes the RDW vortices, similar to the slender wing, and multiple shear-layer vortices. These are weaker and less axisymmetric secondary vortices that arise in the shear-layer roll-up region, between the outboard RDW vortices and the trailing edge. The vortices of the 50° RDW were weaker in terms of the vorticity, tangential velocity and circulation. The vortices lost the concentration and axisymmetry since $\alpha = 18^\circ$, after which they developed into patches of weak vorticity. Interestingly, C_{Lmax} was sustained for $22^\circ < \alpha < 30^\circ$, exposing the impertinent role of RDW vortices in the stalling of the wing.

Passive Tip-vortex Control Techniques

Lee [44] studied the effect of Gurney flaplike side-edge strips (SESs) on a 65° -sweep RDW with a $1.5\%c$ and $3\%c$ strip-height setting. The SESs achieved desirable lift augmentation by increasing C_{Lmax} and the zero-angle-of-attack lift coefficient $C_{L,\alpha=0}$. It was found that the SESs induced a spanwise camber effect and alleviated the crossflow leakage at the trailing/side edges, boosting the positive pressure on the lower surface. At the same time, the SES-equipped RDW had a larger C_D at a given incidence compared to the clean-wing (SES-free) counterpart due to a larger momentum deficit in the wake. Higher vortex strength, more wake-like core flow, and increased total circulation were observed on the RDW with SESs, and these effects were more pronounced on the larger strip height. The lift augmentation outperformed the larger drag and resulted in an improved L/D , showing off the enhanced aerodynamic performances with the employment of the SES.

Inspired by the use of anhedral in the Lippisch-designed X-112 series, Lee et al. [45] investigated a 65° RDW with a variety of anhedral angles at $8^\circ \leq \delta_A \leq 45^\circ$. It turned out that anhedral always led to a lower lift-to-drag ratio than that of the clean RDW (without anhedral). The larger the δ_A , the lower the L/D , which can be attributed to the $99\% - 71\%$ reduction in projected wing area associated with $\delta_A = 8 - 45^\circ$ [45]. However, the addition of anhedral helped sustain the concentrated and axisymmetric form of the RDW vortices at higher incidences where the vortices of the clean wing had already become diffused and skewed. Generally speaking, the larger the anhedral, the stronger the RDW vortices, and the larger the incidence at which the vortices maintained their regularity, with the exception of circulation. Γ_o

was enlarged by the anhedral of $\delta_A = 8^\circ$ and 15° , but decreased on the 30° and 45° configurations. Although the addition of anhedral seems ineffective or even deteriorative for the aerodynamic efficiency of RDWs in free stream, there is supporting evidence that a surging L/D is attainable for a range of anhedral angles at ground clearance less than $40\%c$ ($h/c < 40\%c$) [46].

2.4 Objectives

The objectives of the project can be summarized as such that for each wing configuration:

1. Conduct flow-field measurements at an experimentally optimal angle of attack of 16° under a stable Reynolds number of 3.3×10^5 for $0.2 \leq x/c \leq 1.5$ and obtain the vortex flow parameters
2. Evaluate the streamwise progression of the vortex flow characteristics
3. Perform force-balance measurements at the same flow conditions for $0^\circ \leq \alpha \leq \alpha_{ss} + 10^\circ$ and obtain the lift and drag forces
4. Produce the lift, drag, and lift-to-drag coefficient curves
5. Evaluate the effects of cropping, anhedral, side-edge strips and winglets through the vortex flow parameters and aerodynamic loads of the variously configured models
6. Estimate the lift and induced drag using the flow-field data of $\alpha = 16^\circ$ and evaluate their validity against the experimentally measured values

CHAPTER 3

Experimental Apparatuses and Methodology

The chapter documents the experimental instrumentation, methods and techniques, data acquisition and post-processing of this study. The sections can be divided into three parts. The flow facility and wing models used in the experiments are overviewed first, succeeded by a detailed coverage of the seven-hole pressure probe, two-directional traverse, and the two-component force balance. The methodology and experimental procedure are elucidated, including the data acquisition and reduction, calculations of vortex flow parameters and estimation of aerodynamic loads.

3.1 Flow Facility

The experiments were conducted in the Joseph A. Bombardier wind tunnel located at the Aerodynamics Laboratory inside the Macdonald Engineering Building of McGill University. Photographs of the wind tunnel and a schematic diagram are presented in Figure 3–1. This low-subsonic open-loop wind tunnel, spanning 19 meters, is powered by a 16-blade, 2.5-meter diameter fan to generate the desired flow speed by suction. The test section is 0.9 m in width, 1.2 m in height and 2.7 m in length, the access to which is enabled by a top-hinged window on each side of the test zone. The 3.3 m contraction section provides an approximate 10:1 contraction ratio, preceded by a 10 mm honeycomb flow straighter and three 2 mm anti-turbulence screens. At the outlet, the 9.1-meter long two-stage diffuser is followed by the suction fan which is controlled by a variable AC motor rated at 125 Hp and equipped with

a custom-designed acoustic silencer for noise attenuation. A miniature pitot tube connected to a Honeywell DRAL 510-DN differential pressure transducer was placed at the front of the test section to help calibrate the required fan speed and constantly monitor the free-stream speed.

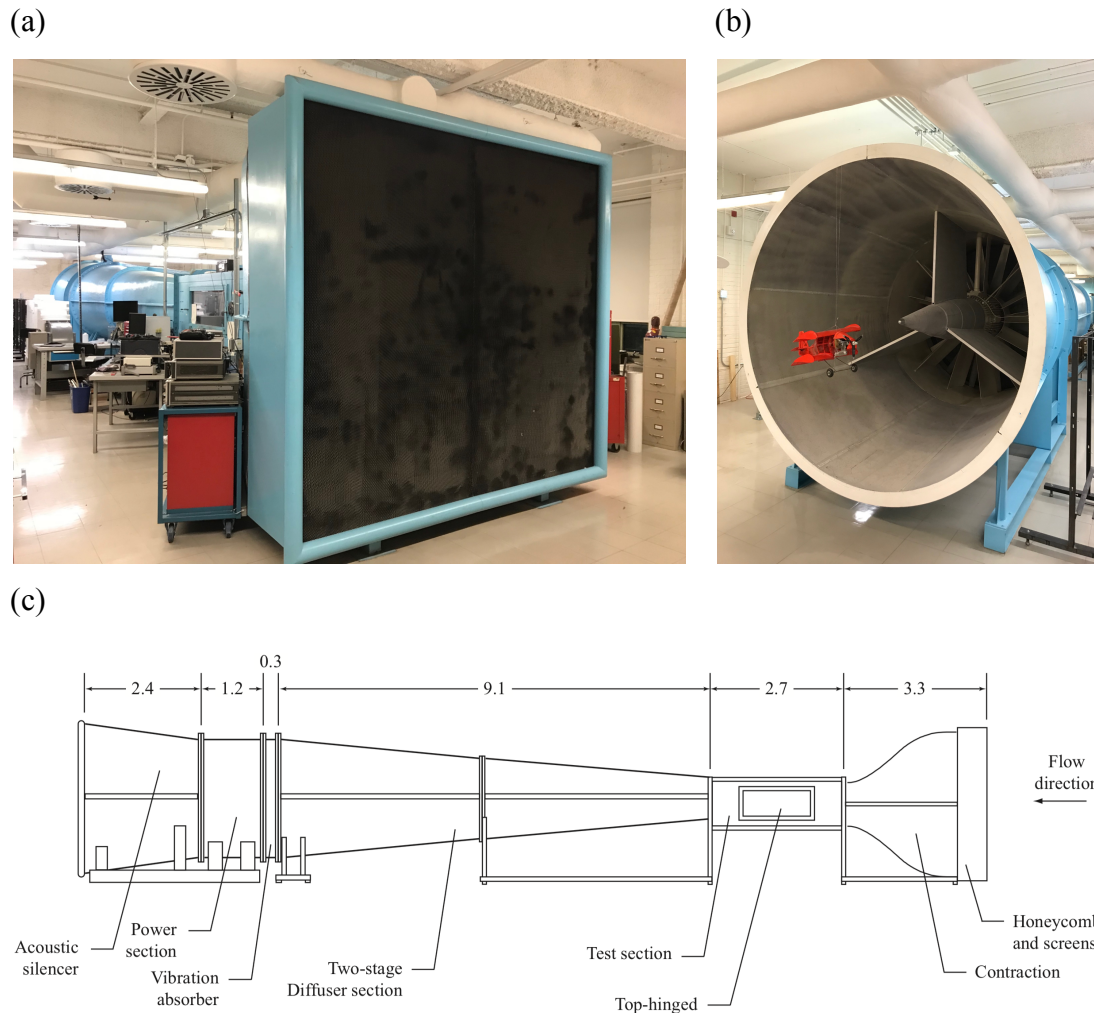


Figure 3-1: Joseph A. Bombardier subsonic wind tunnel. (a) tunnel inlet; (b) tunnel outlet; (c) tunnel schematic diagram [14].

3.2 Wing Models

Seven different RDW models were manufactured in-house to emulate the various planform features from the X-112 series and the AirFish-8. Specifically, the 30%*c* trailing-apex cropping (*crp*), 15° anhedral (*ahd*), and 45° winglets (*wgt*) were employed individually and jointly to create the different configurations. In addition, Gurney flaplike side-edge strips were installed on every clean-wing model as a lift-augmentation device.

The baseline RDW had a maximum chord length of 40.6 cm and a sweep angle of 65°, fabricated with flat 1/16-inch thick iron-steel sheet, giving a thickness-to-chord ratio of 0.39%. The wing had a 37.9 cm leading edge perpendicular to the incoming flow, and the two trailing or side edges converged at the trailing apex point facing downstream. The second wing model had its trailing apex removed by 30% of the maximum chord, introducing a third trailing edge that is perpendicular to the free stream. Based on the second model, the cropped wing was then folded about the centreline to create the 15° anhedral. Then the next model had 5.7 cm ($\approx 15\%c$) of its wingtips bent parallel to the crest at 60° upward relative to the wing surface, or 45° relative to the horizontal plane to emulate the winglets. Lastly, the first three models were retrofitted with side-edge strips (SESs), that included the BW, cropped wing, and the cropped wing with anhedral. The SESs were manufactured with thin aluminum strips with an average width of 1.6 cm, which were meticulously bent longitudinally to a right angle and a desired height of 0.81 cm, 2% of the maximum chord. The strips were installed flush against the side edges and perpendicular to the wing surface of the clean wing models. The 65° DW counterpart was simply the

same baseline RDW reversed 180° . Finally, conventional axisymmetric tip vortices behind a square wing were briefly investigated as complimentary data, which were obtained at $\alpha = 10^\circ$ and $1.01 \leq x/c \leq 3.0$ behind a CNC-machined aluminum NACA 0012 half-wing model installed vertically to the tunnel floor. The three-dimensional models of all seven RDWs and the DW are presented in Figure 3–2, and the geometric parameters are detailed in Table 3–1.

Table 3–1: Wing configurations and geometric parameters

Wing models	c (cm)	c_{cropped}	δ_A	h_{SES}	b (cm)	S (cm ²)	S/S_{BW}	AR
DW	40.64	–	0°	–	37.90	770.2	1	1.865
BW	40.64	–	0°	–	37.90	770.2	1	1.865
BW+SES	40.64	–	0°	0.02c	37.90	770.2	1	1.865
crp	28.45	0.3c	0°	–	37.90	700.8	0.910	2.050
crp+SES	28.45	0.3c	0°	0.02c	37.90	700.8	0.910	2.050
crp+ahd	28.45	0.3c	15°	–	36.61	677.0	0.879	1.980
crp+ahd+SES ¹	28.45	0.3c	15°	0.02c	36.61	677.0	0.879	1.980
crp+ahd+wgt	28.45	0.3c	15°	–	33.66	659.0	0.856	1.720
NACA 0012 ²	27.94	–	–	–	50.80	1419.4	–	1.818

¹crp+ahd+SES denotes cropped reverse delta wing with joint anhedral and side-edge strips

²tip vortex scanned at $1.01 \leq x/c \leq 3.0$ for reference

The wing was bolted to a streamlined T-shaped mounting bracket by two countersunk screws at an approximately 1/3 chord length from the trailing end. For the wing models with anhedral, an adapter made of 1/8" iron-steel sheet was needed to connect the wing and the mounting bracket. The adapter was welded to the down side of crest along the fold line. The T-bracket allowed for precise adjustment of the angle of attack from 0° to 30° . In the present study, all the models were fixed at $\alpha = 16^\circ$ and the wing configuration was the only variable. The mounting bracket

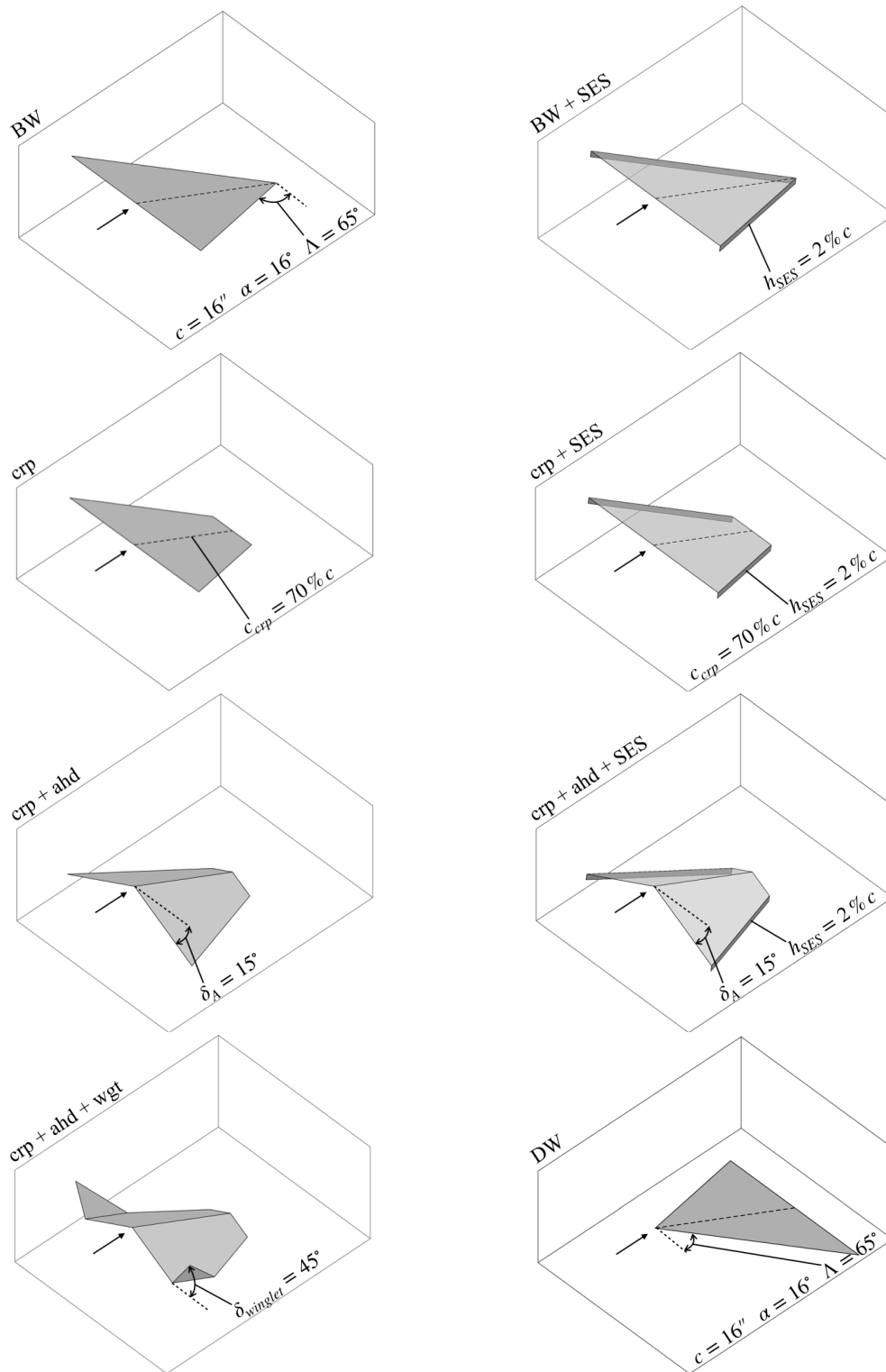


Figure 3-2: Wing configurations. (BW, DW, crp, ahd, wgt, SES each denotes baseline wing, delta wing, cropped, anhedral, winglet and side-edge strip, respectively.)

was inserted into a slit and fastened by three bolts at the top of a NACA 0012-profiled support pointing into the flow. The wing support was then anchored to a large rectangular aluminum plate with chamfered edge on the windward side, which was shifted upstream in 10% c increments to attain the flow-field measurements at progressive streamwise locations. The pressure probe and traverse were placed at the same location for each wing model (Figure 3–3).

3.3 Instrumentation

3.3.1 Seven-hole Pressure Probe

The flow measurements along the wing ($0.2 \leq x/c < 1.01$) and in the near-field ($1.01 \leq x/c \leq 1.5$) were realized by a miniature seven-hole pressure probe. The practicality of the seven-hole pressure probe stood out for the purpose of this study because it is more accurate at high flow angles (up to 70°) than the more conventional four-hole or five-hole pressure probe; can gather both velocity and pressure data while hot-wire anemometry cannot; it enables direct three-dimensional measurements and is more cost-effective compared to other non-intrusive techniques, such as particle image velocimetry (PIV) or laser doppler velocimetry (LDV).

As detailed in Figure 3–4 (a), the pressure probe had a brass tip of 2.8 mm in diameter, on which seven 0.5 mm holes were drilled parallel to the shaft axis and six ports of which were arranged in a 2.4 mm circle around the central port. The tip was finished with a 30° cone angle and fitted into a 110 mm long probe shaft. 1.6 mm Tygon tubes, threaded through a 400 mm long probe sting, connected the pressure taps inside the probe tip to a transducer array box which was mounted far downstream. The transducer array was comprised of seven DC002NDR5 differential

pressure transducers with a maximum head of 50 mm water and an average resolution of 61.5 Pascals/Volt, whose reference pressure was the ambient atmospheric pressure measured in a fibreglass covered damping unit [14]. The output of the transducer array was passed to a custom-built signal conditioner which was made of a seven-channel analog signal differential amplifier with a gain of 5:1 and an external DC power source that provided a 3.5 V offset. The side-view of the complete experimental setup in the test section is presented in Figure 3-3.

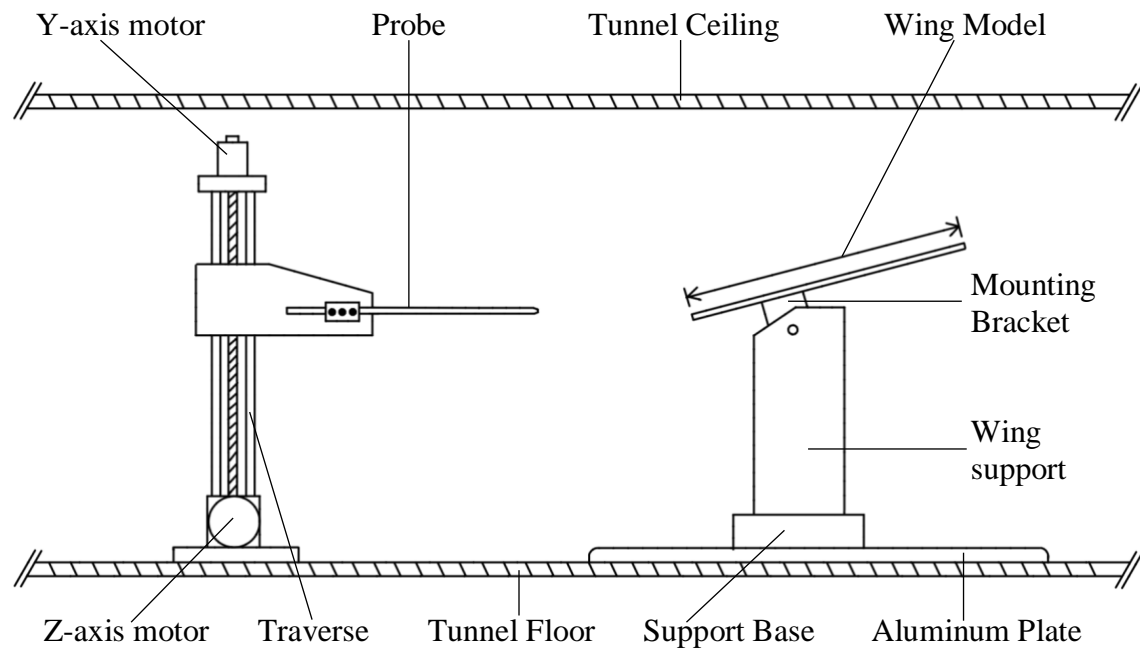
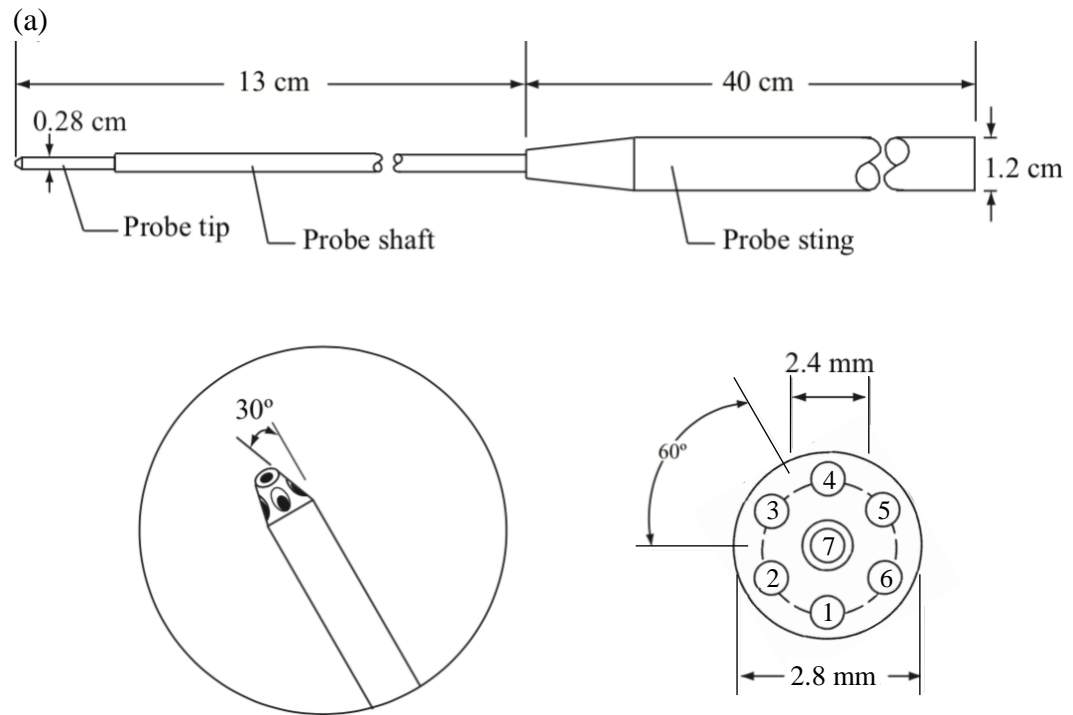


Figure 3-3: General arrangement of the experimental setup in the test section.

The method of determining the flow direction and magnitude and the calibration process are reviewed in brevity. The magnitude of the flow is obtained by a total pressure (relating to the pressure in the port that is most aligned with the flow) and static pressure (relating to the pressures in the surrounding ports), much like a



(b)



Figure 3-4: Seven-hole pressure probe and traverse mechanism. (a) schematic diagram of the probe [14]; (b) the traverse.

conventional pitot tube. The flow direction, described by two sets of angles, either pitch (α) and yaw (β), or cone (θ) and roll (ϕ), is determined by comparing pressures on opposite sides of the probe. The independence of velocity allows the establishment of a single set of calibration coefficients for any flow velocity.

The pressure probe was calibrated in situ following the method of Wenger and Devenport [47]. The process involved subjecting the probe to a set of known angles at the anticipated experimental flow velocity, and recording the static and total pressure coefficients and two directional coefficients, expressed in terms of the pressures sensed by the seven ports. A custom-built traverse was used to pitch the probe by an angle α in the x-y plane and to yaw by an angle β in the y-z plane. The tested range was from -70° to 70° in 5° increments in both directions.

At low flow angles, assuming full flow attachment at the tip, the pressure at the centre port (7) was greater than the other six and was used to calculate the total pressure. The static pressure was approximated by the average pressure of the peripheral ports (1-6). The directional coefficient for pitch was obtained by comparing the pressures on the top and bottom ports (1 and 4), similarly, the coefficient in yaw was the difference between ports 2,3 on the left and ports 5,6 on the right. The

coefficients were normalized by the dynamic pressure as follows:

$$C_\alpha = \frac{p_4 - p_1}{p_7 - \bar{p}} \quad (3.1)$$

$$C_\beta = \frac{(p_5 + p_6)/2 - (p_2 + p_3)/2}{p_7 - \bar{p}} \quad (3.2)$$

$$C_t = \frac{p_7 - p_{tot}}{p_7 - \bar{p}} \quad (3.3)$$

$$C_s = \frac{p_7 - p_{stat}}{p_7 - \bar{p}} \quad (3.4)$$

$$\bar{p} = \sum_{n=1}^6 \frac{p_n}{6} \quad (3.5)$$

where $n = 1, 2, \dots, 7$ and p_n is the pressure sensed at port n .

At high flow angles, the maximum pressure reading appeared in one of the six peripheral ports. The three ports on the leeward side were assumed to be in a separated flow, and only the maximum pressure port (i), the two adjacent ports in the ring (denoted by CW and CCW), and the centre port (7) were included. Therefore, p_i was used for the total pressure coefficient, and p_{CW} and p_{CCW} for the static pressure coefficient. The cone angle θ was determined by the difference between p_i and p_7 , while the roll angle ϕ was the difference between p_{CW} and p_{CCW} . All coefficients were normalized by the dynamic pressure as well. Their mathematical

expressions are:

$$C_\theta = \frac{p_i - p_7}{p_i - \bar{p}} \quad (3.6)$$

$$C_\phi = \frac{p_{CW} - p_{CCW}}{p_i - \bar{p}} \quad (3.7)$$

$$C_t = \frac{p_i - p_{tot}}{p_i - \bar{p}} \quad (3.8)$$

$$C_s = \frac{p_i - p_{stat}}{p_i - \bar{p}} \quad (3.9)$$

$$\bar{p} = \frac{p_{CW} + p_{CCW}}{2} \quad (3.10)$$

By positioning the probe at each known angle and measuring the seven pressures in the probe and the reference pressure, four normalized coefficients were calculated at each angle. The two-step process detailed by Wenger and Devenport [47] fits the data to a third-order least-squares surface and records each error value to create a look-up table. During interpolation of the experimental data, the third-order surface fit plus the linearly interpolated error based on the look-up table constitute the final result. Finally, the velocity vectors u, v, w were calculated from the equations below:

$$|\vec{V}| = \sqrt{\frac{2}{\rho}(p_n - \bar{p})(1 + C_s - C_t)} \quad (3.11)$$

$$u = |\vec{V}| \cos \alpha \cos \beta \quad or \quad = |\vec{V}| \cos \theta \quad (3.12)$$

$$v = |\vec{V}| \sin \alpha \cos \beta \quad or \quad = |\vec{V}| \sin \theta \sin \phi \quad (3.13)$$

$$w = |\vec{V}| \sin \beta \quad or \quad = |\vec{V}| \sin \theta \cos \phi \quad (3.14)$$

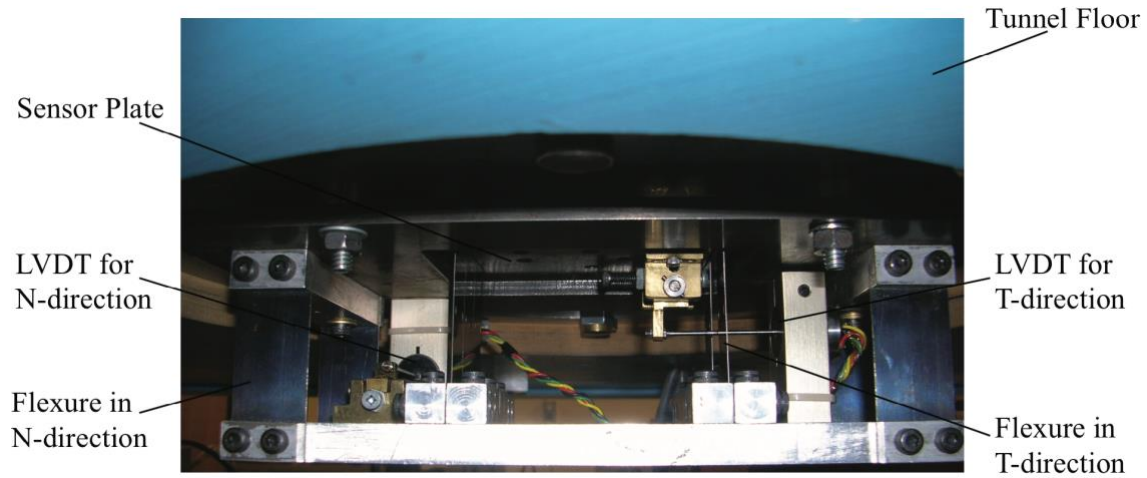
3.3.2 Two-dimensional Traverse Mechanism

For each scan, the movement of the probe in the transverse measurement plane was assisted by a two degree-of-freedom traverse mechanism. The probe was secured in the probe holder on the traverse as shown in Figure 3-4 (b). The spatial relationship between the traverse and the wing model can also be observed in the same figure. A Sanyo-Denki 103-718-0140 stepper motor powered the vertical movement in the y axis, and a Biodine 2013MK2031 stepper motor was responsible for the spanwise movement in the z axis. The traverse translation accuracy was $20 \mu m$ in y and $60 \mu m$ in z . The motors were controlled by a NI PCI-7344 4-axis motion controller that was synchronized with the data acquisition and automation programs in LabVIEW. Flow blockage induced by the traverse was estimated at under 8%.

3.3.3 Two-component Force Balance

The force balance measurements were performed in the same flow facility. The force-balance setup was designed around a circular disk socketed into the centre of the tunnel floor that connected the force sensors underneath the floor to the wing model inside the tunnel through an embedded sensor plate (Figure 3-5 (b)). The circular disk acted as a turntable to allow for change of angle of attack. The rectangular sensor plate, embedded in the turntable, was connected to the wing model by a CNC-machined aluminum mounting shaft and a streamlined cantilever beam. The sensor plate could only translate in the transverse direction (parallel to the wing chord) and the normal direction (perpendicular to the wing chord). It was supported by a set of four 0.035" thick flexures of a 5 mm maximum deflection in each axis (Figure 3-5 (a)), which was independently measured by a Sanborn 7DCDT-1000

(a)



(b)

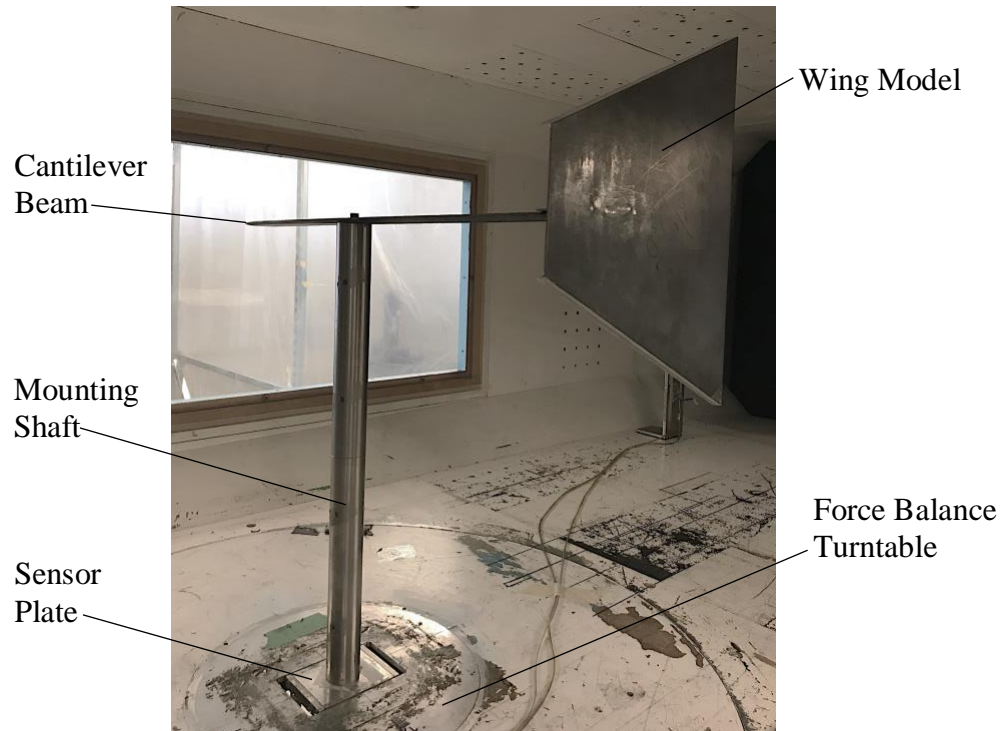


Figure 3-5: Photographs of the two-component force balance. (a) force balance sensors under the tunnel [14]; (b) force balance test section setup.

linear variable differential transformer (LVDT) that was calibrated in situ using a series of calibration weights. During the calibration, known weights were aligned in the normal direction and were hung from the top of the mounting shaft via a pulley system with non-elastic aluminum wire. 50 g weights were incrementally added up to a total of 2 kg and the corresponding time-averaged voltages from the LVDTs were recorded. The same was repeated for the transverse direction. Linear regression analysis of force versus voltage indicated that the resolutions of the LVDTs were 102.3 and 53.9 Newtons/Volt in the normal and transverse directions respectively and the coefficients of determination were under 0.25%. In addition, the combined drag force of the mounting shaft and cantilever beam was measured before testing the wing model and eliminated from the final drag forces of the wing. The actual lift and drag forces (L and D) can be decoupled from the normal and transverse forces (N and T) with the two following equations:

$$L = N \cos \alpha - T \sin \alpha \quad (3.15)$$

$$D = N \sin \alpha + T \cos \alpha \quad (3.16)$$

3.4 Data Acquisition and Reduction

Data acquisition from both the pressure probe and force balance was done using a 16-channel, 16-bit NI PCI-6259 DAQ board installed on a Dell Dimension E100 PC. A NI BNC-2110 connector block was used to connect the transducer array output from the signal conditioner and the DAQ board. The output voltages were sampled at 2000 Hz for 10 seconds for the wake survey, and 15 seconds for the force balance. Due to the large amount of output data and the linear responses in the calibration of

the pressure transducers and LVDTs, only time-averaged results were recorded and stored on the PC. Other sampling frequencies and sampling times were tested, and the resulted differences were less than 0.1 mV. This was attributed to the damping effect on fluctuations inside the 550 mm Tygon tubing connecting to the pressure taps [14]. The flowchart in Figure 3–6 demonstrates the process of data acquisition and reduction for the study.

The time-averaging technique used in the flow-field measurements meant that for a typical scan of 3000 data points, it would take more than 8 hours to complete, which would ultimately undermine the functionality of the wind tunnel and probe traverse. Hence an adaptive grid scheme was employed where a fine resolution of $\Delta y = \Delta z = 3.17$ mm was set in the vortex region and a coarser resolution of $\Delta y = \Delta z = 6.35$ mm in the wing wake and free-stream regions. As the measurements progressed downstream, the grid boundaries and distribution of the fine resolution was adjusted according to the vortex growth and trajectory. After the scan, the coarse resolution grid was interpolated to the fine resolution grid before the computation of the various flow quantities. Figure 3–7 illustrates an example of the adaptive scan grid, the cross-stream velocity vector plot after interpolation, as well as the resulted flow visualization using axial vorticity contours.

3.4.1 Vortex Flow Properties

The three components of the flow velocity were processed in MATLAB to compute vortex flow properties, such as vorticity, tangential velocity, circulation, vortex radius and centre location. The axial vorticity, ζ , was calculated using the finite difference method. The central difference form was applied to all the interior data

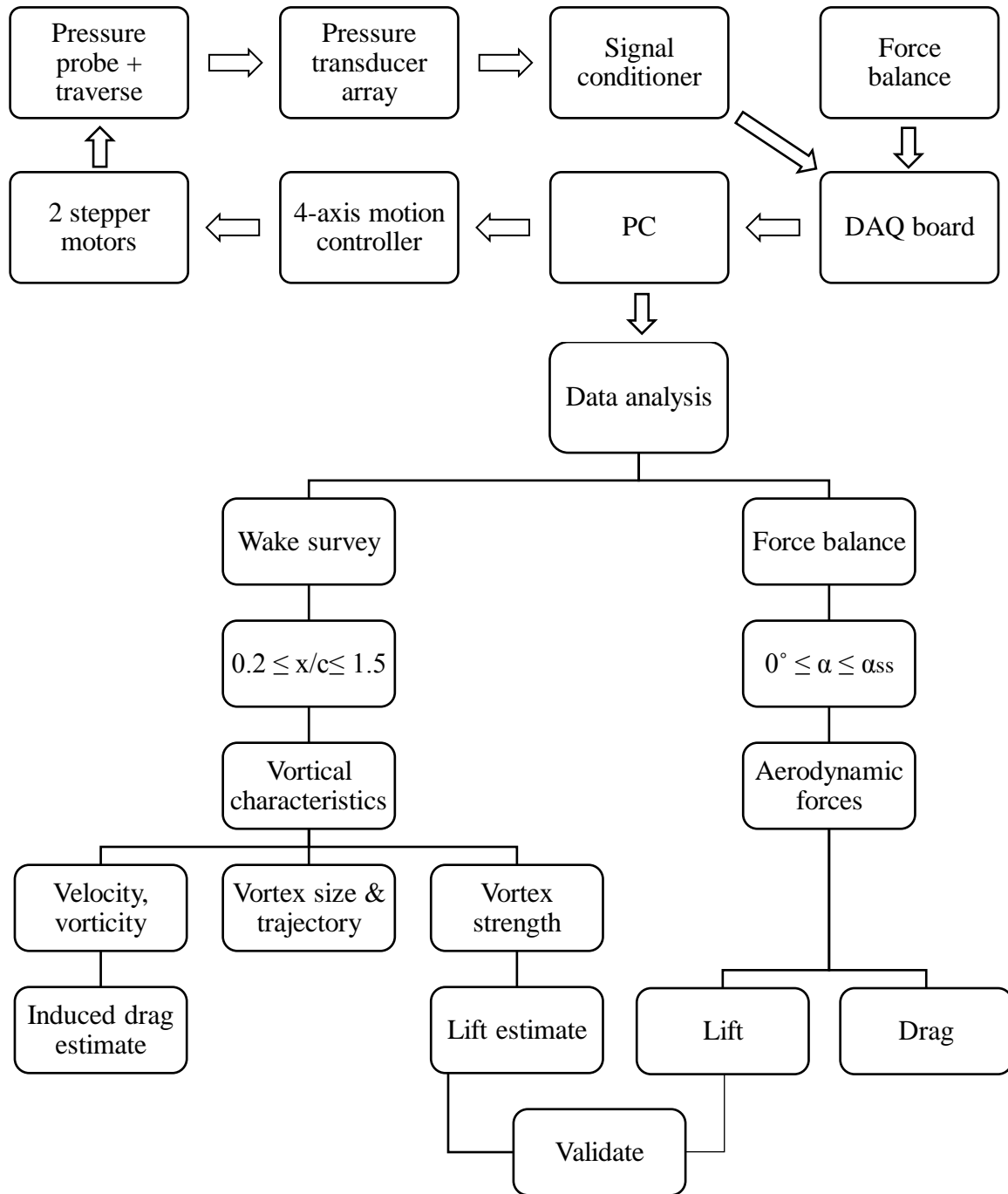


Figure 3-6: Data acquisition overview.

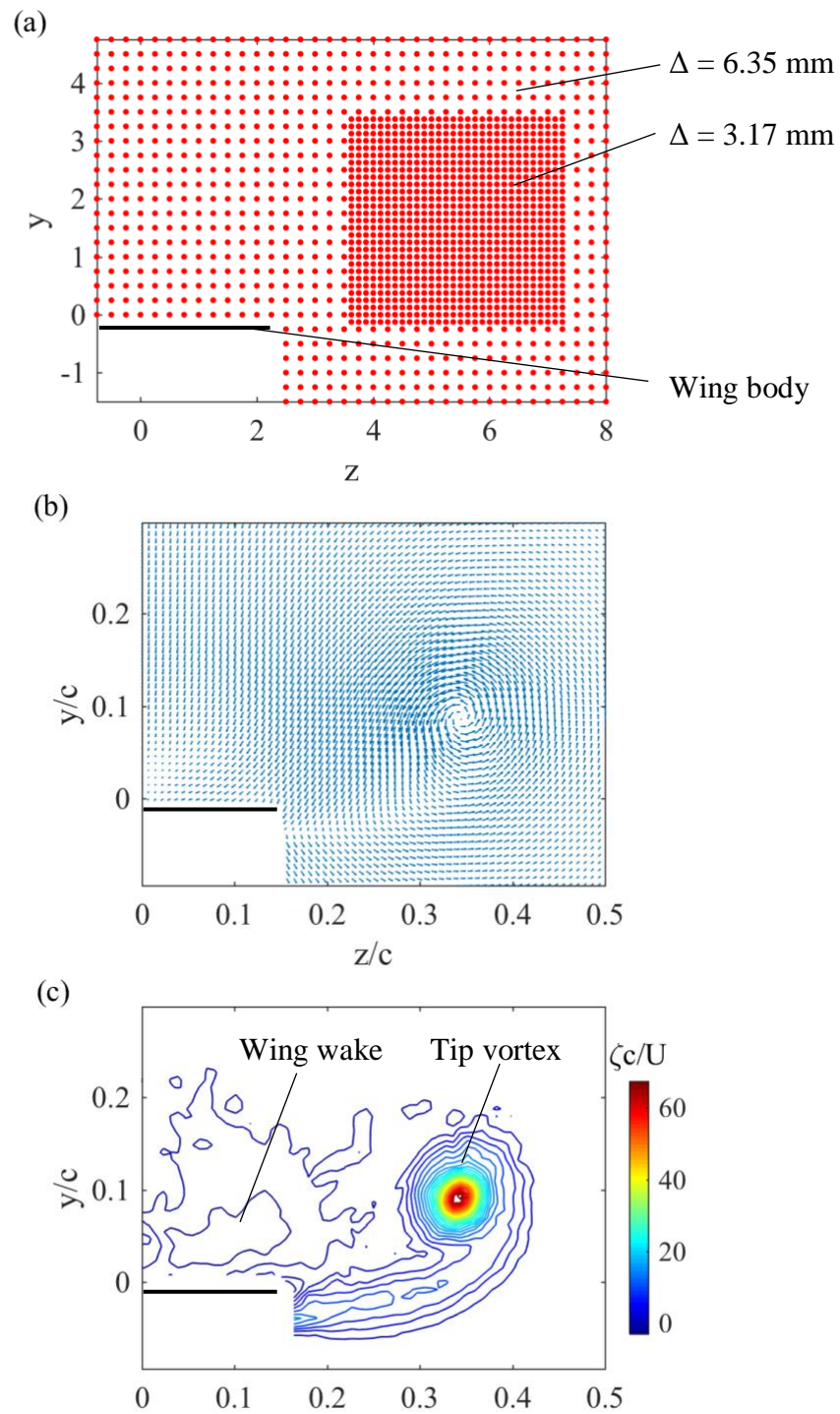


Figure 3-7: RDW+SES at $x/c=1.2$. (a) adaptive grid; (b) cross-stream velocity vectors; (c) axial vorticity contours.

points, while the forward and backward difference forms were used at the grid boundaries,

$$\zeta = (\nabla \times \vec{V})_x = \frac{\partial w}{\partial y} - \frac{\partial v}{\partial z} \quad (3.17)$$

$$\zeta_{j,i} \approx \frac{w_{j,i+1} - w_{j,i-1}}{2\Delta y} - \frac{v_{j+1,i} - v_{j-1,i}}{2\Delta z} \quad (\text{central}) \quad (3.18)$$

$$\zeta_{1,i} \approx \frac{w_{1,i+1} - w_{1,i-1}}{2\Delta y} - \frac{v_{2,i} - v_{1,i}}{\Delta z} \quad (\text{forward}) \quad (3.19)$$

$$\zeta_{n,i} \approx \frac{w_{n,i+1} - w_{n,i-1}}{2\Delta y} - \frac{v_{n,i} - v_{n-1,i}}{\Delta z} \quad (\text{backward}) \quad (3.20)$$

where $j = 1, 2, \dots, m$ and $i = 1, 2, \dots, n$ are the number of the grid points in column and row. Δz and Δy are the spanwise (horizontal) and transverse (vertical) grid spacing, both of which equaled to 3.17 mm. The vortex centre was located at the occurrence of the maximum axial vorticity as seen below.

$$y_c = y(\zeta = \zeta_{max}) \quad z_c = z(\zeta = \zeta_{max}) \quad (3.21)$$

The tangential velocity, v_θ , was computed around the vortex centre with a rotated frame of reference. θ was positive in the counterclockwise direction from the positive z axis, and v_θ followed the same sign convention.

$$v_{\theta j,i} = (v_{j,i} - v_c) \sin \theta - (w_{j,i} - w_c) \cos \theta \quad (3.22)$$

A polar coordinate system was established about the vortex centre in order to estimate the vortex core radius, r_c , and its overall size, r_o (Equation 3.24-3.25). i and j are indices in the radial and tangential direction, where i ranges from 1 to 40, and j is divided into 180 intervals in a full resolution. The core circulation, Γ_c , was

obtained through a line integral of the tangential velocity along the circle of r_c . The total circulation, Γ_o , was computed via an integral of the product of axial vorticity and unit area within the radius of r_o using the initial Cartesian coordinates. (j, i are each the spanwise and vertical index in Equation 3.27.)

$$r_{i,j} = (z_j - z_c)^2 + (y_i - y_c)^2 \quad (3.23)$$

$$r_c = r(v_{\theta i,j} = v_{\theta max}) \quad (3.24)$$

$$r_o = r(\zeta_{i,j} = 0.01\zeta_{max}) \quad (3.25)$$

$$\Gamma_c = \oint V \cdot dl = \sum_{j=0}^{180} v_{\theta i=c,j} \times r_c \Delta\theta_j \quad \Delta\theta_j = \pi/90 \quad (3.26)$$

$$\Gamma_o = \iint \zeta \cdot dS = \sum \sum \zeta_{j,i} \times \Delta z \Delta y \quad r_{j,i} < r_o \quad (3.27)$$

3.4.2 Lift and Induced Drag Estimation

The circulation-based lift force was computed by the Kutta-Joukowski Theorem using Γ_o in the near-field and effective wing span or vortex span, b' (spanwise distance between the centres of a vortex pair), demonstrated in Equation 3.28 and Figure 3–8.

$$L_{\Gamma_o} = \rho U \Gamma_o b' \quad \text{where} \quad b' = 2z_c \quad (3.28)$$

Kaplan et al. [48] showed that lift from the Kutta-Joukowski Theorem can correlate relatively well with theoretical and measured lift forces of thin flat-plate models of a rectangular wing, a semi-elliptical wing and a delta wing with $AR = 2$ and $Re = 8000-24000$. Lee and Ko [12] computed the circulation-based lift for the 65° slender RDW using PIV at $Re = 11000$ and reported an underestimate ($\approx 10-15\%$) relative to the force-balance values obtained at a higher $Re = 340000$. In the present

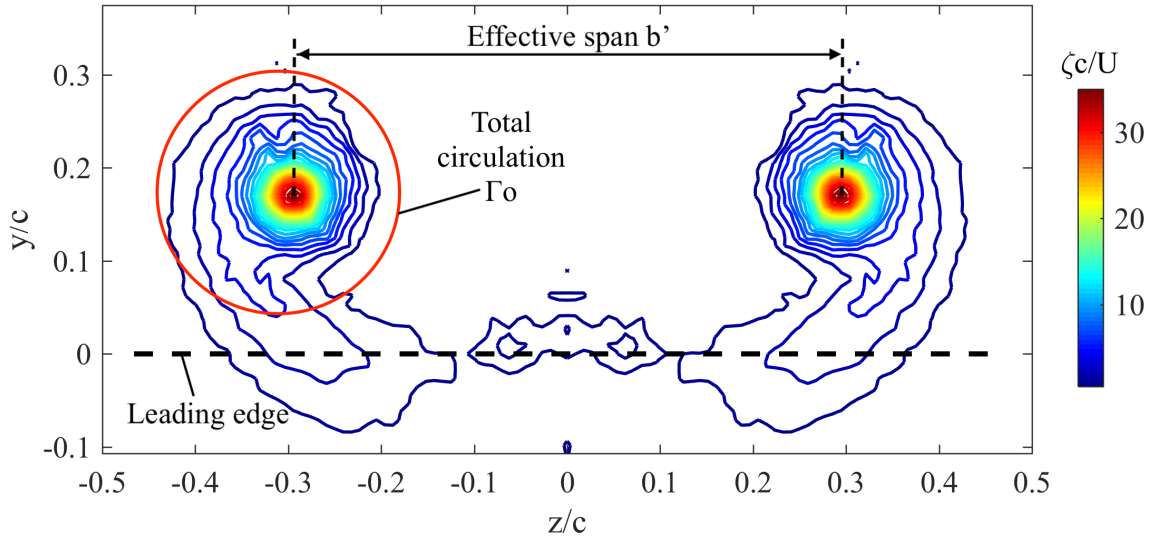


Figure 3–8: Axial vorticity contour plot at $x/c = 1.2$ demonstrating total circulation Γ_o and effective span b' .

study, the same $Re = 330000$ was adopted in both the wake scan and force-balance measurements to find out if the reduced viscous effect could improve the correlation between the estimated and measured lifts for a flat-plate slender RDW regardless of the wing configuration.

The lift-induced drag, D_i , was calculated using Maskell's wake integral model [32]. The application procedure is briefly discussed in this section. Details on the derivation of Maskell's equation can be found in references [31, 40].

$$D_{i,M} = \frac{1}{2}\rho \iint_{S_\zeta} \psi \zeta dydz - \frac{1}{2}\rho \iint_{S_1} \phi \sigma dydz \quad (3.29)$$

$$\text{where } \zeta = -\frac{\partial v}{\partial z} + \frac{\partial w}{\partial y} \quad \sigma = \frac{\partial v}{\partial y} + \frac{\partial w}{\partial z} \quad (3.30)$$

$$v = \frac{\partial \psi}{\partial z} + \frac{\partial \phi}{\partial y} \quad w = -\frac{\partial \psi}{\partial y} + \frac{\partial \phi}{\partial z} \quad (3.31)$$

ζ is the axial vorticity, σ is a special source term derived from integration by parts. ψ and ϕ are the stream function and velocity potential function, respectively. S_1 is any downstream wake measurement plane, and S_ζ is the region within S_1 where vorticity is nonzero. Steady, incompressible flow is assumed, and the boundary condition that ψ and ϕ both be zero on the edges of the downstream measurement plane is imposed. The model shows that the calculation of induced drag comes down to the four parameters $\zeta, \sigma, \psi, \phi$ in the flow field. The result is independent of the streamwise gradients at the boundaries of the scan, which may not be small in the wake of a wing, such as the data in this study ($x/c \leq 1.5$). It can be shown that in the event that the streamwise gradients vanish, the Maskell wake integral model is analytically equivalent to the Kusunose solution shown below [49].

$$D_i = \iint_{S_1} \frac{1}{2} \rho (v^2 + w^2) dy dz \quad (3.32)$$

To apply the Maskell model to the measurements in the near-field, the finite difference method was used once again in order to decompose the stream and potential functions into discrete functions along the grid points, such as ζ and σ . The crossflow velocities were used to implicitly define ψ and ϕ expressed in the form of central differences,

$$v_{j,i} = \frac{\psi_{j+1,i} - \psi_{j-1,i}}{2\Delta z} + \frac{\phi_{j,i+1} - \phi_{j,i-1}}{2\Delta y} \quad (3.33)$$

$$w_{j,i} = -\frac{\psi_{j,i+1} - \psi_{j,i-1}}{2\Delta y} + \frac{\phi_{j+1,i} - \phi_{j-1,i}}{2\Delta z} \quad (3.34)$$

$$2\Delta s v_{j,i} = \psi_{j+1,i} + \psi_{j-1,i} + \phi_{j,i+1} - \phi_{j,i-1} \quad (3.35)$$

$$2\Delta s w_{j,i} = \psi_{j,i+1} - \psi_{j,i-1} + \phi_{j+1,i} - \phi_{j-1,i} \quad (3.36)$$

where $\Delta s = \Delta z = \Delta y$. The model also requires that both functions at the boundaries are zero, thus

$$\psi_{1,n} = \psi_{j,n} = \psi_{m,1} = \psi_{m,i} = 0 \quad (3.37)$$

$$\phi_{1,n} = \phi_{j,n} = \phi_{m,1} = \phi_{m,i} = 0 \quad (3.38)$$

Now a system of $(m - 2) \times (n - 2)$ equations and $(m - 2) \times (n - 2)$ unknowns was formed such that $A\vec{X} = \vec{B}$, where A was a matrix of coefficients, \vec{X} contained the unknown functions of ψ and ϕ and \vec{B} were the known functions of v and w . By inverting matrix A and multiplying it by B , $\vec{X} = A^{-1}\vec{B}$ could be solved. Finally, substituting the four functions into Equation 3.29, the induced drag was obtained with the formula below.

$$D_{i,M} \approx \frac{1}{2}\rho \sum_{j=2}^{n-1} \sum_{i=2}^{m-1} (\psi_{j,i}\zeta_{j,i} - \phi_{j,i}\sigma_{j,i}) (\Delta s)^2 \quad (3.39)$$

3.5 Experimental Uncertainty

The experimental uncertainties involved in the seven-hole pressure probe and force balance measurements are tabulated below. The uncertainties were results of: uncontrollable atmosphere outside the test tunnel, machining tolerances, mechanical hardware and digital sensor limitations, data extrapolation, etc. The propagation of error was analyzed using the constant odds method by Moffat [50].

Table 3-2: Experimental uncertainties of flow conditions and wing models

Parameter	Uncertainty(\pm)	Uncertainty(%)	Operating value
Free stream velocity	0.2 m/s	1.67 %	12 m/s
Wing chord	0.0005 m	0.12 %	0.406 m
Reynolds number	5.39×10^3	1.66 %	3.25×10^5
Wing sweep angle	1°	-	65°
Wing angle of attack	0.5°	-	16°
Wing roll angle	1°	-	0°
Wing yaw angle	1°	-	0°

Table 3-3: Experimental uncertainties of force balance measurements

Parameter	Uncertainty(\pm)	Uncertainty(%)	Operating range
Transverse resolution	0.05 N	0.25 %	0-19.6 N
Normal resolution	0.09 N	0.46 %	0-19.6 N
Wing angle of attack	0.25°	-	0-50°
Transverse calibration linearity	-	0.19%	-
Normal calibration linearity	-	0.23 %	-
A/D conversion	1 mV	-	-
Transverse LVDT reading	0.054 N	0.28 %	0-19.6 N
Normal LVDT reading	0.102 N	0.52 %	0-19.6 N
Total transverse force	0.074 N	0.38 %	0-19.6 N
Total normal force	0.136 N	0.69 %	0-19.6 N
Lift coefficient	0.074	-	0-1.5
Drag coefficient	0.041	-	0-1.4

Table 3–4: Experimental uncertainties of seven-hole pressure probe measurements

Parameter	Uncertainty(\pm)	Uncertainty (normalized)
Free stream velocity	0.2 m/s	1.67 %
Traverse position in y	0.25 mm	0.063 %
Traverse position in z	0.76 mm	0.19 %
Grid resolution in y	3.18 mm	0.78 %
Grid resolution in z	3.18 mm	0.78 %
Vortex centre location in y	3.18 mm	0.78 %
Vortex centre location in z	3.26 mm	0.80 %
Total vortex radius	2.28 mm	0.56 %
Pressure transducer	-	0.33 %
3.5V offset signal	2 mV	0.06 %
Total pressure	-	0.34 %
Velocities u, v, w	0.27 m/s	2.3 %
Tangential velocity	0.39 m/s	3.3 %
Streamwise vorticity	-	9.8 %
Total circulation	-	11.9 %

CHAPTER 4

Results and Discussion

This section presents the results and findings of the low-speed wake survey of the variously configured reverse delta wing (RDW) models. The discussion is organized into two parts, the characteristics of the tip vortices quantified by the vortex parameters, and the aerodynamic performances of the RDWs based on the measured loads. The emphasis is on the former. The 65° flat-plate RDW and its matching delta wing (DW) of the same make are first presented and established as the baseline case. Next, effects of the cropping, anhedral, side-edge strip, and winglet are each elaborated in the aforementioned two-part fashion. The section then reports the predicted lift and induced drag of each wing using the vortex flow field. After comparing to the experimental values, it finally concludes with comments on the predictions and the validity of the prediction methods.

4.1 Baseline Wing - 65°-sweep Reverse Delta Wing

As reviewed in Chapter 2, the behaviour of the vortices on a slender RDW was seen to heavily depend on the angle of attack [12]. Small and concentrated vortices were generated at low angles of attack ($\alpha < 10^\circ$) and larger but diffused vortices were seen at high angles of attack ($\alpha > 20^\circ$). The section first examines the development of the tip vortices behind the baseline 65° RDW at changing angles of attack and strives to find an angle of attack at which the vortex is strong, concentrated and large enough for the purpose of this study. Afterwards, the focus is placed on the

streamwise evolution of the vortices at the selected angle which sets the baseline data for the evaluation and comparison of the other wing configurations. Then the vortical characteristics and properties of the baseline RDW, also referred to as the baseline wing (BW), are discussed in depth and compared with those of the DW counterpart. Lift and drag coefficient curves too are incorporated to supplement the understanding of the wing aerodynamics.

4.1.1 Dependence of the Vortex Structure on the Angle of Attack

The iso-vorticity contours in Figure 4–1 show the baseline RDW vortex when α was increased from 8° to 28° immediately after the trailing apex. At low α , the vortex remained concentrated and the vorticity level at the vortex centre peaked between 12° and 16° , after which it dropped as α continued to rise. In terms of the shape and size, the vortex size increased dramatically, and the vortex centre location shifted more inboard and upward with increasing α .

It can be seen that the vortex initially appeared axisymmetric, indicated by the concentric and tightly spaced contour lines around the core below $\alpha = 16^\circ$, and gradually lost the axisymmetry past 20° . At $\alpha \geq 28^\circ$, the vortex lost coherence and diffused into many tiny patches of circulation-like flow. Lee and Ko [12] conducted the near-wake vortex survey on a 65° RDW between $\alpha = 4^\circ$ and 30° at $Re = 1.1 \times 10^4$ and reported that both ζ_{peak} and $v_{\theta peak}$ reached maximum at $\alpha = 16^\circ$ and the vortex strength was ever-growing at larger α .

The axial velocity contours included in Figure 4–2 at the trailing apex expose that with increasing incidence, the size of the axial flow wake increased much more aggressively in the vertical direction than in the spanwise direction. The growing

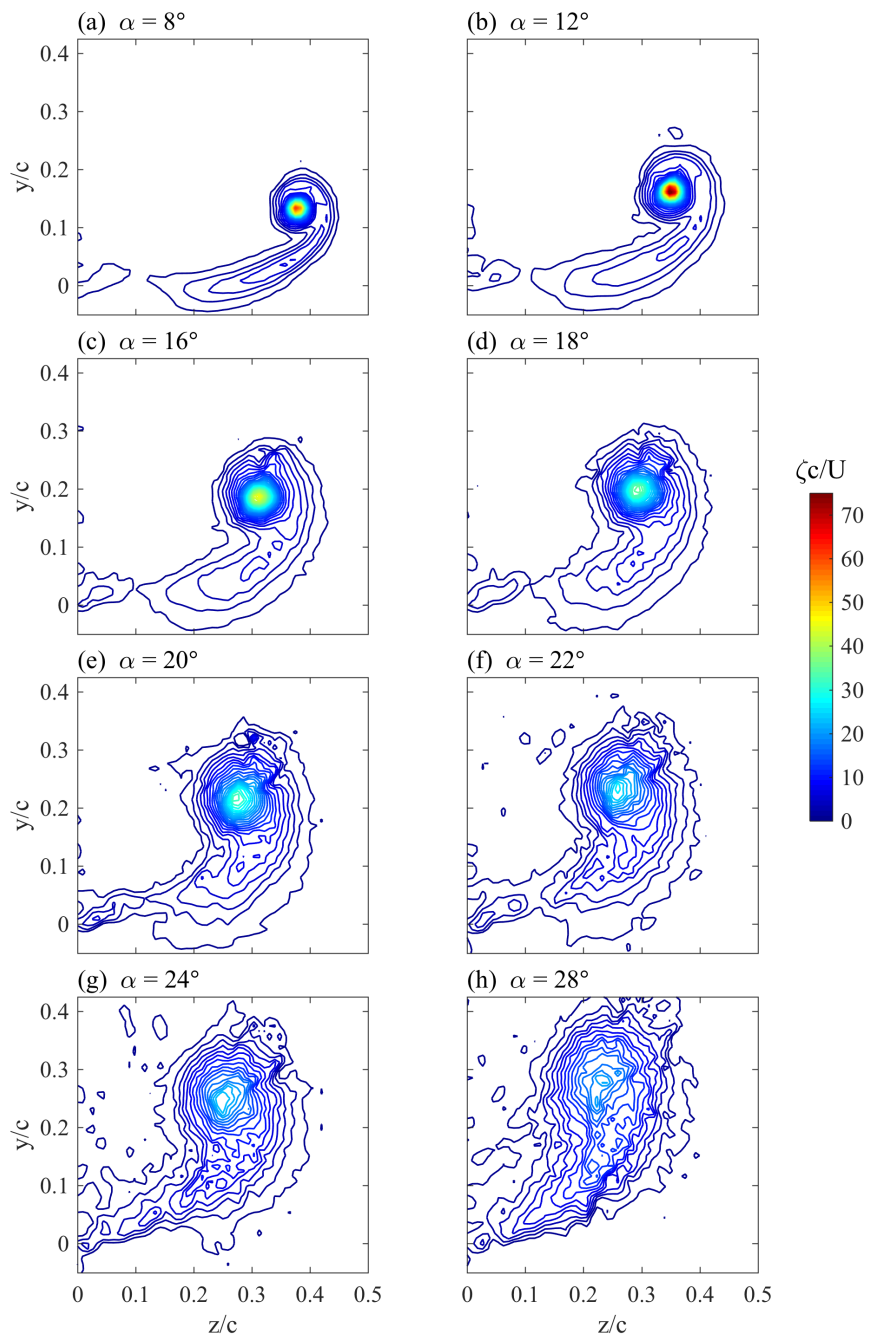


Figure 4-1: Iso-vorticity contours of the baseline RDW vortex at $x/c = 1.01$ for $8^\circ \leq \alpha \leq 28^\circ$.

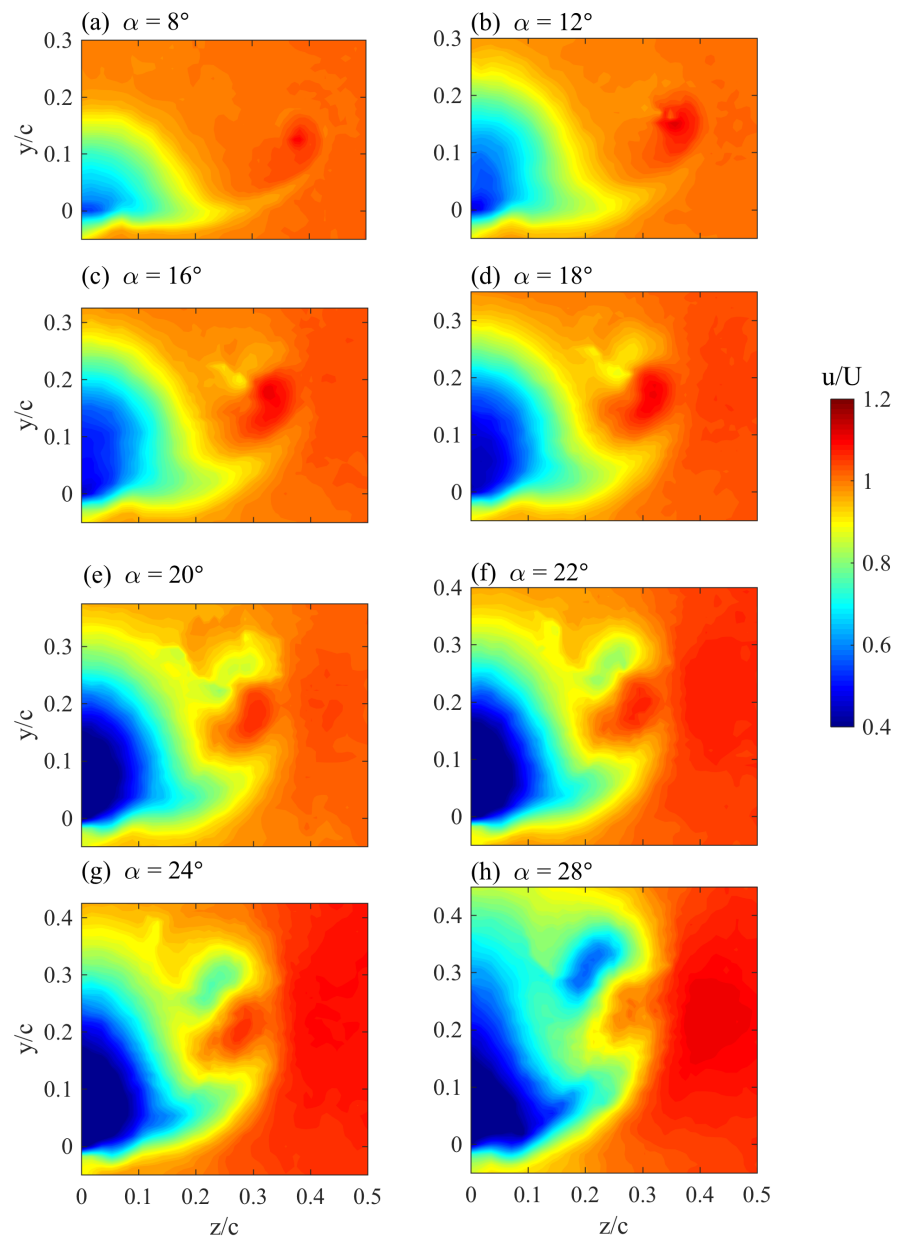


Figure 4-2: Iso-axial velocity contours of the baseline RDW vortex at $x/c = 1.01$ for $8^\circ \leq \alpha \leq 28^\circ$.

wake entrained the tip vortex and retarded the axial flow, with the upper inboard region of the vortex core being the most affected. At $\alpha = 28^\circ$, the vortex was hardly identifiable and was almost entirely “swallowed” by the wing wake. As the main objective was to investigate the streamwise development of the RDW tip vortices, $\alpha = 16^\circ$ was selected for the study because of the well defined vortex structure, strong vorticity and sufficiently large vortex radius.

4.1.2 Streamwise Progression of the Vortex Flow Characteristics of the BW at $\alpha = 16^\circ$

Figure 4-3 (a) presents the iso-vorticity contours of the BW at incremental chordwise stations, from behind the leading-edge, $x/c = 0.2$, to half-a-chord downstream the trailing apex point, $x/c = 1.5$. The separated shear layer continually provided high vorticity to sustain the vortex during the roll-up that lasted until beyond the trailing apex. For $0.2 \leq x/c \leq 0.7$, the shear layer could be identified along the centre of the “arm” section sandwiched between two layers of low-vorticity fluid. Small axial vorticity was present directly above the wing at $x/c \leq 0.3$ but was not observable along the rest of the chord. Between $x/c = 0.8$ and 1.01 , this strip of high-vorticity flow could hardly be differentiated from its surrounding fluid, foreshadowing that the influence on the vortices from the lower-side shear layer had diminished and the majority of the roll-up and vorticity-feeding had been completed. At $x = 1.5c$, the “arm” appeared to have been detached from the wing; the “fist” retained the concentrated structure and its vorticity contours emerged similar to a conventional tip vortex, e.g. NACA 0012 in Figure 4-4 (a3). The peak vorticity level ζ_{peak} was at a maximum at $x/c = 0.3$ and decayed with x/c while the vortex size swelled continuously.

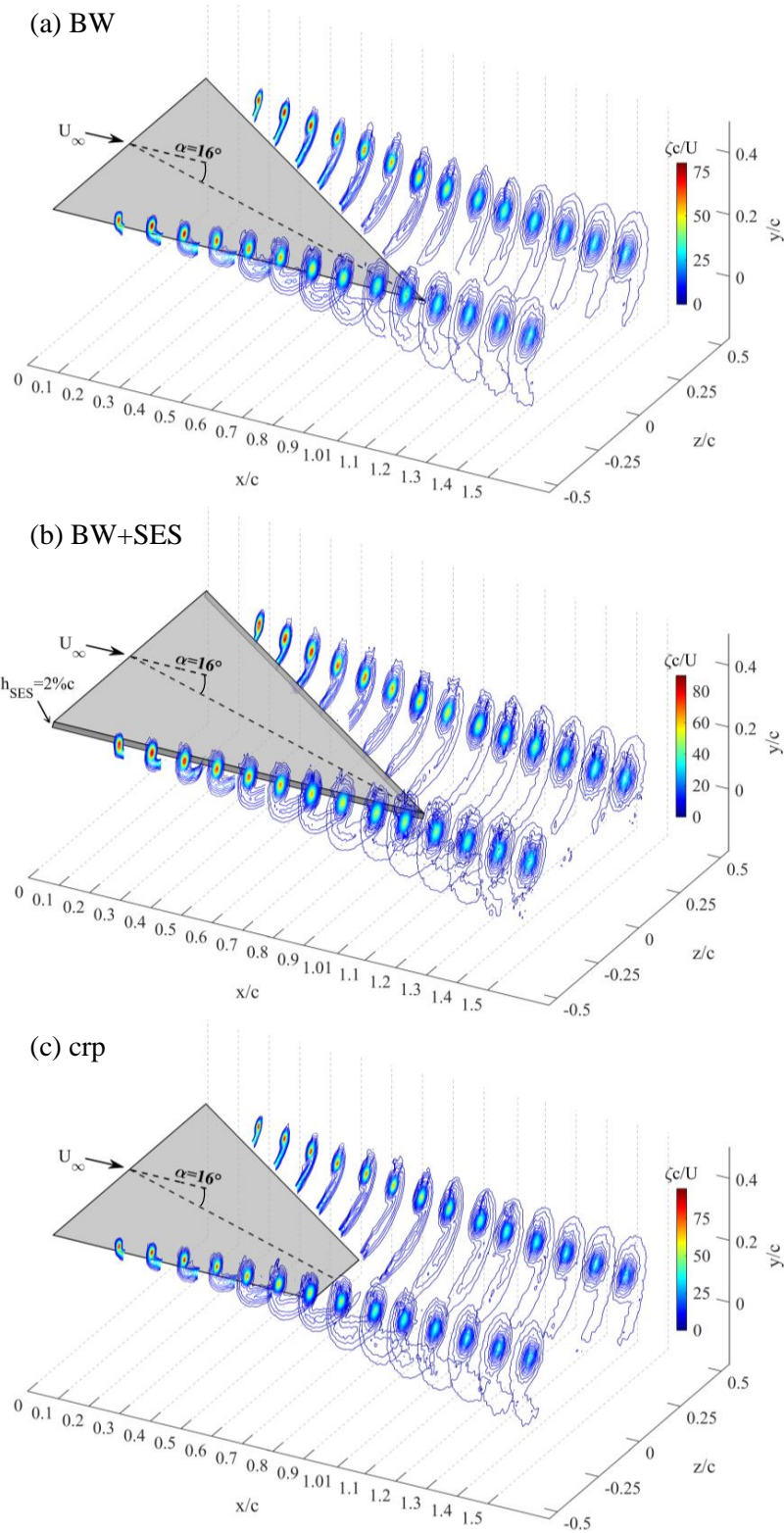


Figure 4-3: Three-dimensional representation of iso-vorticity contours at all stream-wise stations at $\alpha = 16^\circ$.

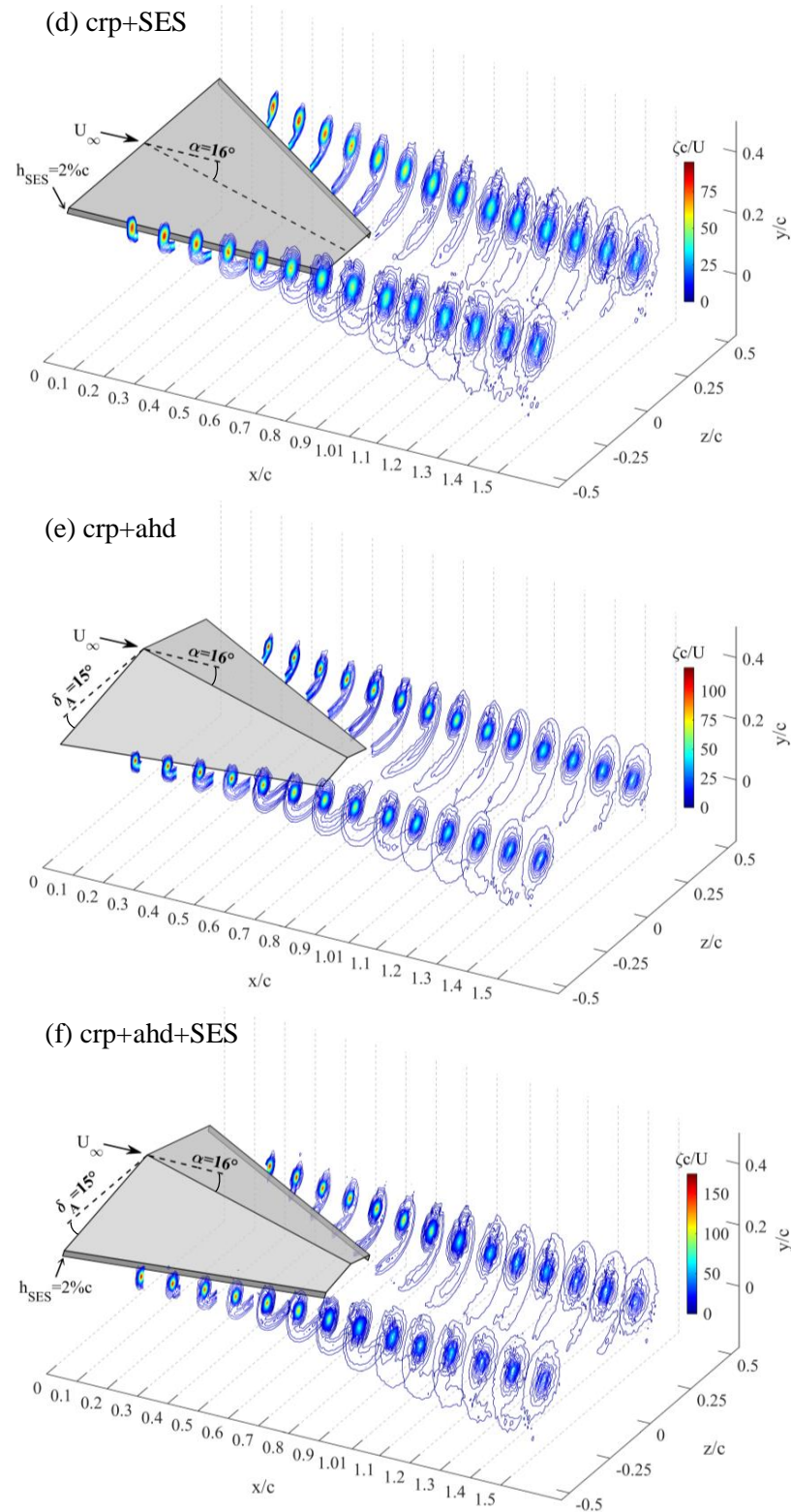


Figure 4-3: Three-dimensional representation of iso-vorticity contours at all stream-wise stations at $\alpha = 16^\circ$. (continued)

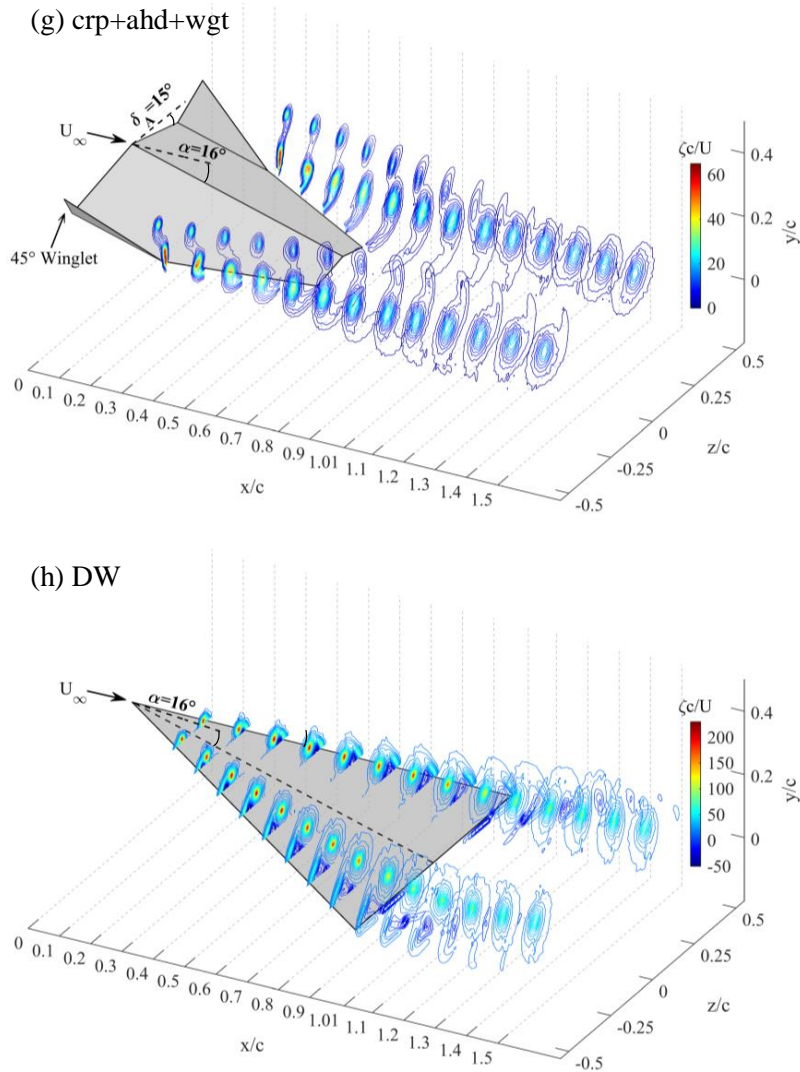


Figure 4-3: Three-dimensional representation of iso-vorticity contours at all stream-wise stations at $\alpha = 16^\circ$. (continued)

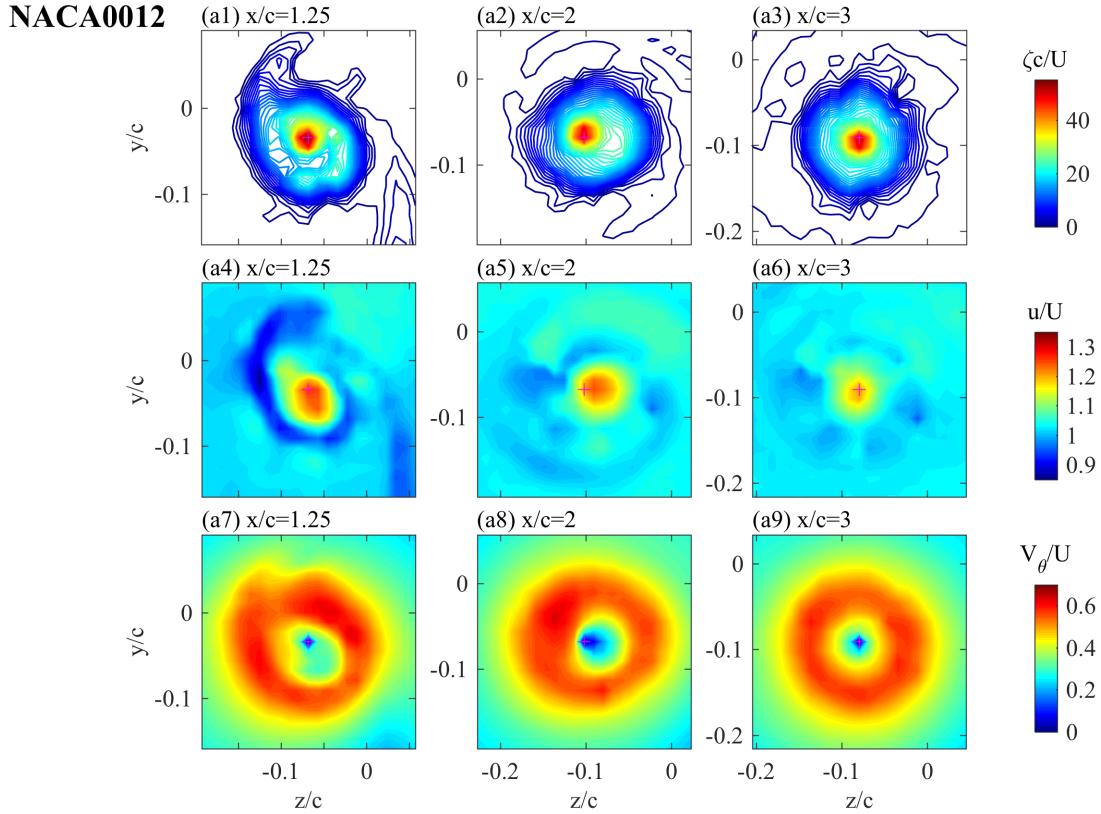


Figure 4–4: NACA0012 tip vortex flow contours at selected x/c . (a1)-(a3) Axial vorticity, (a4)-(a6) axial velocity, and (a7)-(a9) tangential velocity.

The various vortex flow parameters at different chordwise stations are plotted in Figure 4–5 to facilitate a quantitative analysis of the streamwise development of the RDW vortices. In plot (a) and (b), both ζ_{peak} and $v_{\theta peak}$ increased with x/c until 0.3 and died down for $0.4 \leq x/c \leq 1.5$. Because of the circumferential averaging of the v_θ values, a more linear and gentle decay was observed on $v_{\theta peak}$ than ζ_{peak} . Similar trends exhibited for the LEVs of the DW but of higher magnitude than the RDW vortices. For the LEVs, ζ_{peak} was more than double that of the RDW vortices for $0.2 \leq x/c \leq 0.8$, dove to less than half around the trailing edge and abated

farther downstream. $v_{\theta peak}$ of the LEVs were as high as the free-stream velocity, U , from $x/c = 0.4$ to 0.7 , it fell to about $0.8U$ at the trailing edge and continued to slow down afterwards. For $1.1 \leq x/c \leq 1.5$, both ζ_{peak} and $v_{\theta peak}$ on the LEVs were approximately twice as large as those of the RDW vortices.

In the vortex core, the axial flow at the vortex centre experienced a mild acceleration, bringing the core axial velocity u_c to just under $1.1U$ before $x/c = 1.01$ (Figure 4-5 (c)). u_c/U decreased gently to 1.02 at $x/c = 1.5$, largely as a result of viscous diffusion [23]. The DW saw a far greater axial flow acceleration of up to twice the free-stream velocity at $x/c = 0.4$, and u_c remained high until the vicinity of the trailing edge where vortex breakdown had most likely occurred, leading to a weakened wake-like core with an average u_c/U of 0.5 . The fluctuations in the stream-wise LEV's axial velocity curve were likely resulted from the non-axisymmetry of the vortex, where the location of ζ_{peak} did not coincide with the location of minimum u_c in the wake-like core. A finer grid resolution is expected to improve the accuracy of the vortex centre location and the core velocity, however, at the expense of added scan time.

Total circulation, Γ_o , rose at each chordwise station and levelled off after the trailing apex ($x/c = 1.01$). The continual feeding of vorticity from the shear layer could justify the steady increase in Γ before the trailing apex, and the plateau suggested that the roll-up process in the vortex core was near complete, argued by Lee and Ko [12]. They tested the same-sweep RDW at $8^\circ \leq \alpha \leq 18^\circ$ and $Re = 1.1 \times 10^4$ and found that Γ_o was invariant after $x/c = 1.01$ regardless of α . The common observation was that the 65° RDW plateaus near $x/c = 1.01$ at $\alpha = 16^\circ$. Γ_o of the

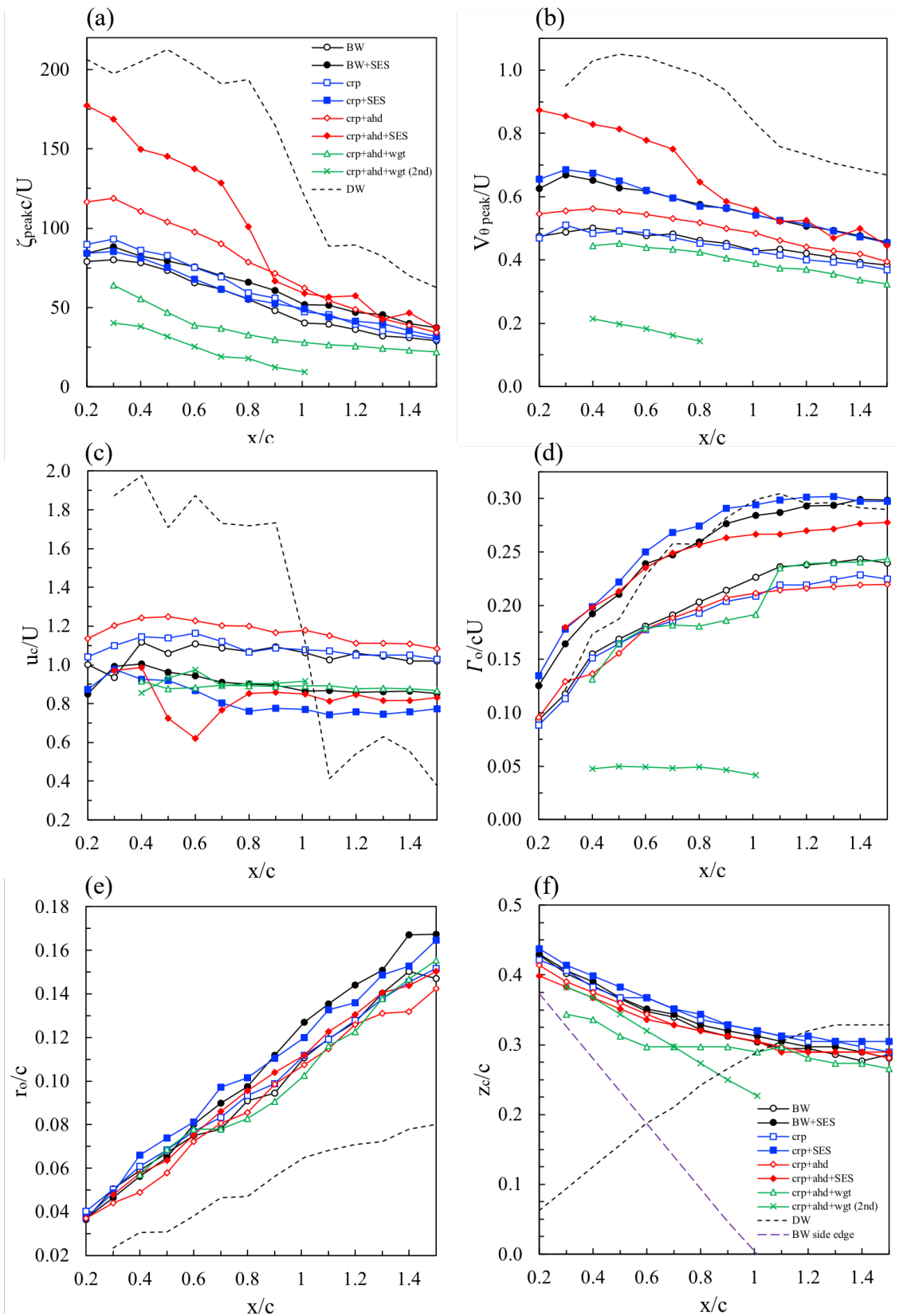


Figure 4-5: (a)-(g) (k)-(l) Streamwise dependence of a series of vortex parameters, (h)-(j) distribution of selected vortex parameters across the vortex core at $x/c = 1.5$.

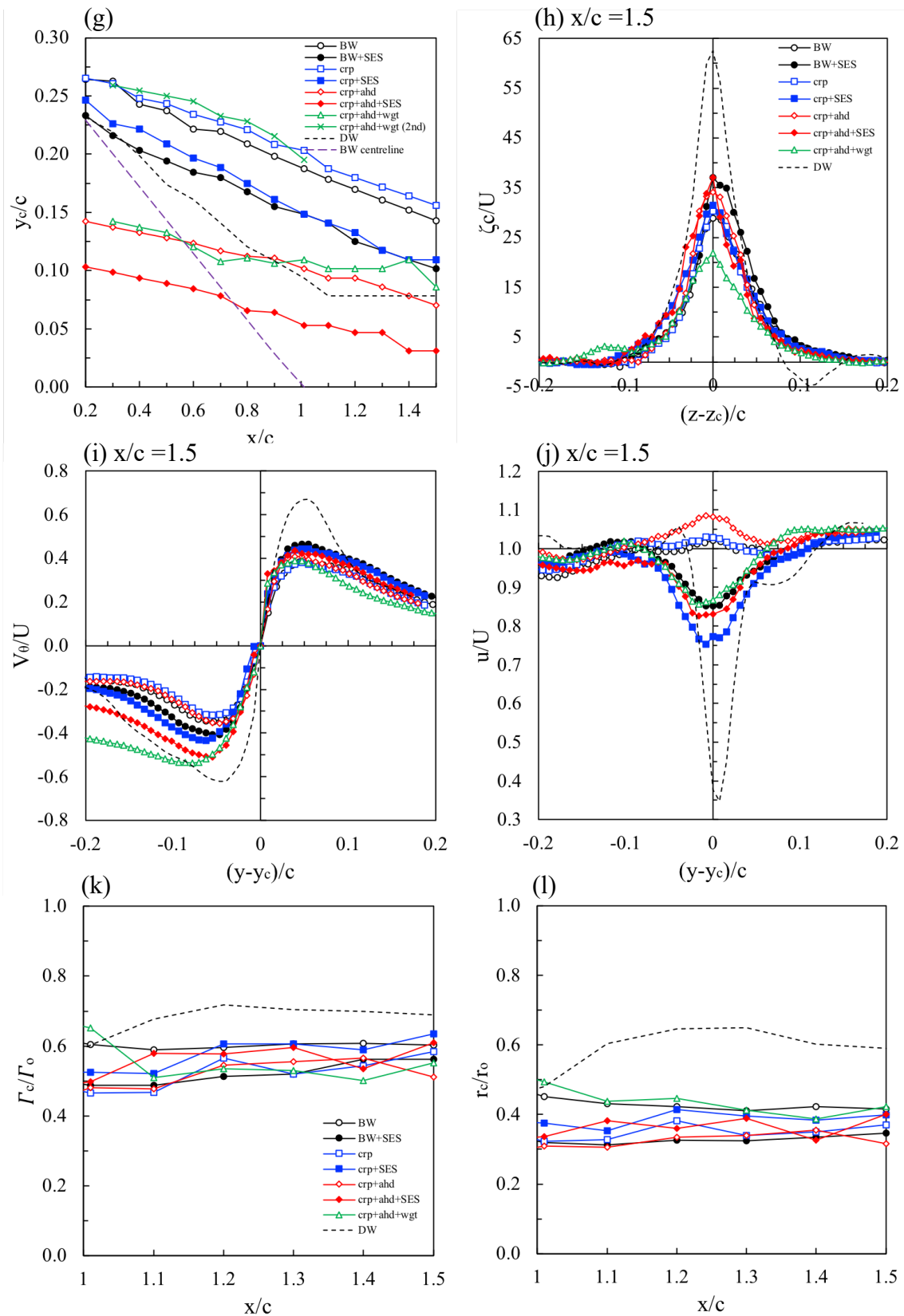


Figure 4-5: (a)-(g) (k)-(l) Streamwise dependence of a series of vortex parameters, (h)-(j) distribution of selected vortex parameters across the vortex core at $x/c = 1.5$. (continued)

DW proliferated above the wing and levelled off at $\Gamma_o/cU = 0.304$, in contrast to 0.242 for the RDW vortex. Behind the BW, the Γ_c -to- Γ_o (core-to-total circulation) was on average 60%, while the ratio was 8% higher on the LEVs, as seen in Figure 4-5 (k).

Figure 4-5 (e) indicates a linear proportionality between the vortex radius r_o and x/c . The vortex centre had an inboard and downward tendency in its downstream evolution, but the vortex always stayed outside the side edges and above the upper surface. The position of the wing is outlined by the purple dotted lines in Figure 4-5 (f)-(g), which helped discover that the more downstream, the bigger the separation between the vortex and the wing in both the spanwise and vertical directions. Throughout the tested streamwise domain, although the vortex centre shifted about $0.125c$ in both directions, the vertical downward shift in y was more linear than the spanwise inboard movement in z . On the other hand, the LEVs were more concentrated, seen by the higher ζ levels and the smaller vortex radii in Figure 4-5 (e). In the same figure, the high strength concentration of the LEVs was also confirmed by the larger ratio of the vortex core radius to outer radius in plot (l), at 17% more than the $r_c/r_o = 43\%$ of the BW vortex. Their persistent inboard position was essential to the desirable vortex lift generated directly on the suction surface of the DW. The shifting of the LEV centre stabilized for $x/c \geq 1.2$.

To better understand the vortex structure and its axisymmetry, close-up of the vortices are found in Figure 4-6 (b). The iso- ζ contours suggest that the RDW vortex was nearly axisymmetric after $x/c = 1.1$, but the axial velocity and tangential velocity contours in Figure 4-7 and 4-8 show that it's not exactly the case. From

$x/c = 0.7$ to 1.5 , in Figure 4–7 (b), the RDW vortex had an apparent duality of wake-like and jet-like axial flow, in comparison to the concentric axial flow patterns inside the LEV in (a). Distributions of the streamwise velocity further confirmed that lower fluid momentum existed in the roll-up on the RDW and the vortex was not yet axisymmetric in the near-wake. As shown in Figure 4–8 (b), outside the vortex centre, the outer layer moving with the highest tangential speed had yet surrounded the centre at the trailing apex. At a similar chordwise position behind the NACA 0012 (Figure 4–4 (a7)), the stagnant vortex centre was wholly enclosed by a ring of highly rotational fluid at $x/c=1.25$; by $x/c = 3$, a uniform circular distribution of high v_θ was displayed in (a9). On the DW, the fluid of high tangential speed was seen to progressively circle around the vortex eye. At $x/c = 1.5$, the fluid had nearly surrounded the stagnant centre, approaching a much more axisymmetric state than the RDW vortex in the near-wake (Figure 4–8 (a)).

Furthermore, it's worthwhile to pay attention to the variation of axial vorticity, tangential velocity and axial velocity in the RDW vortex. Figure 4–9 presents the distribution of these three parameters at selected x/c along a vertical line passing through the vortex centre, (z_c, y_c) , lending insight to how the roll-up evolved and the axisymmetry was gradually approached as x/c increased. ζ and v_θ are assigned positive values in the counter-clockwise direction. The tangential velocity was zero at the vortex centre, ascended to a local maximum $v_{\theta peak}$ which was used to identify vortex core radius, r_c , then asymptotically approached zero away from the centre. As x/c changed from 0.7 to 1.5 , the axial vorticity distribution evolved closer to the Gaussian distribution with a diminishing peak value. The local maximum and

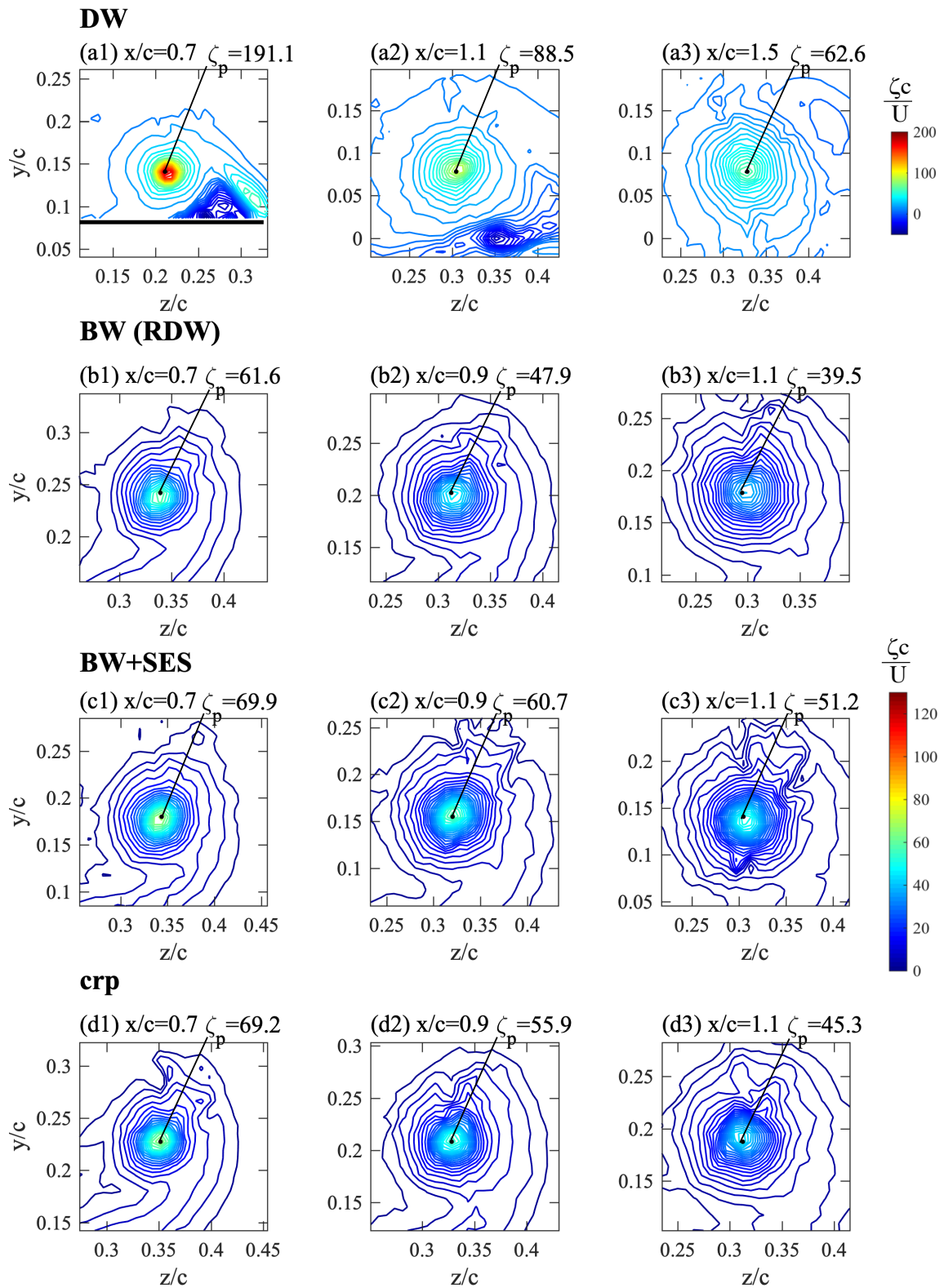


Figure 4-6: Close-up of normalized iso-vorticity contours at selected x/c . ζ_p denotes $\zeta_{peak}c/U$.

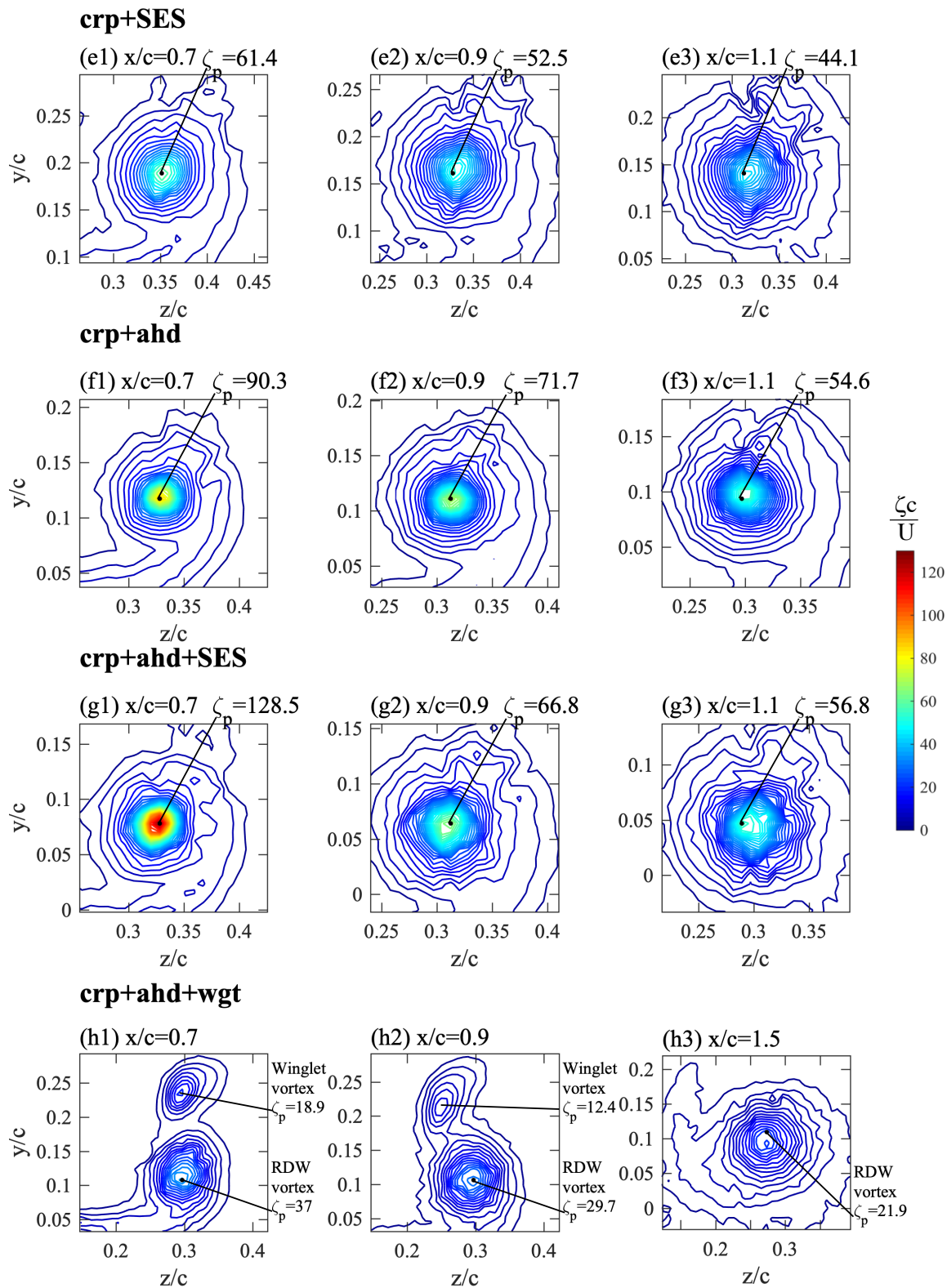


Figure 4-6: Close-up of normalized iso-vorticity contours at selected x/c . ζ_p denotes $\zeta_{peak}c/U$. (continued)

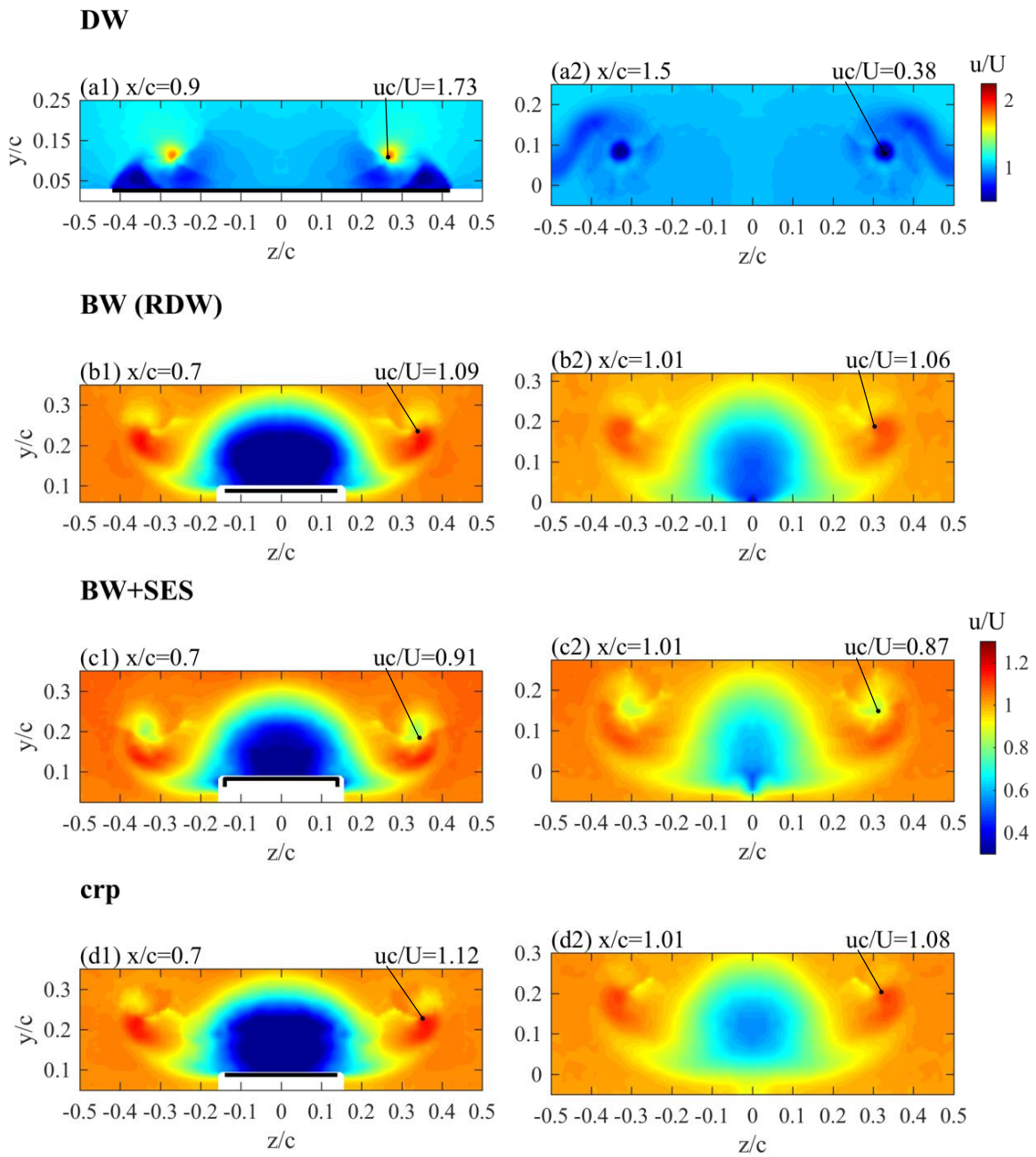


Figure 4-7: Normalized axial velocity contours at selected x/c .

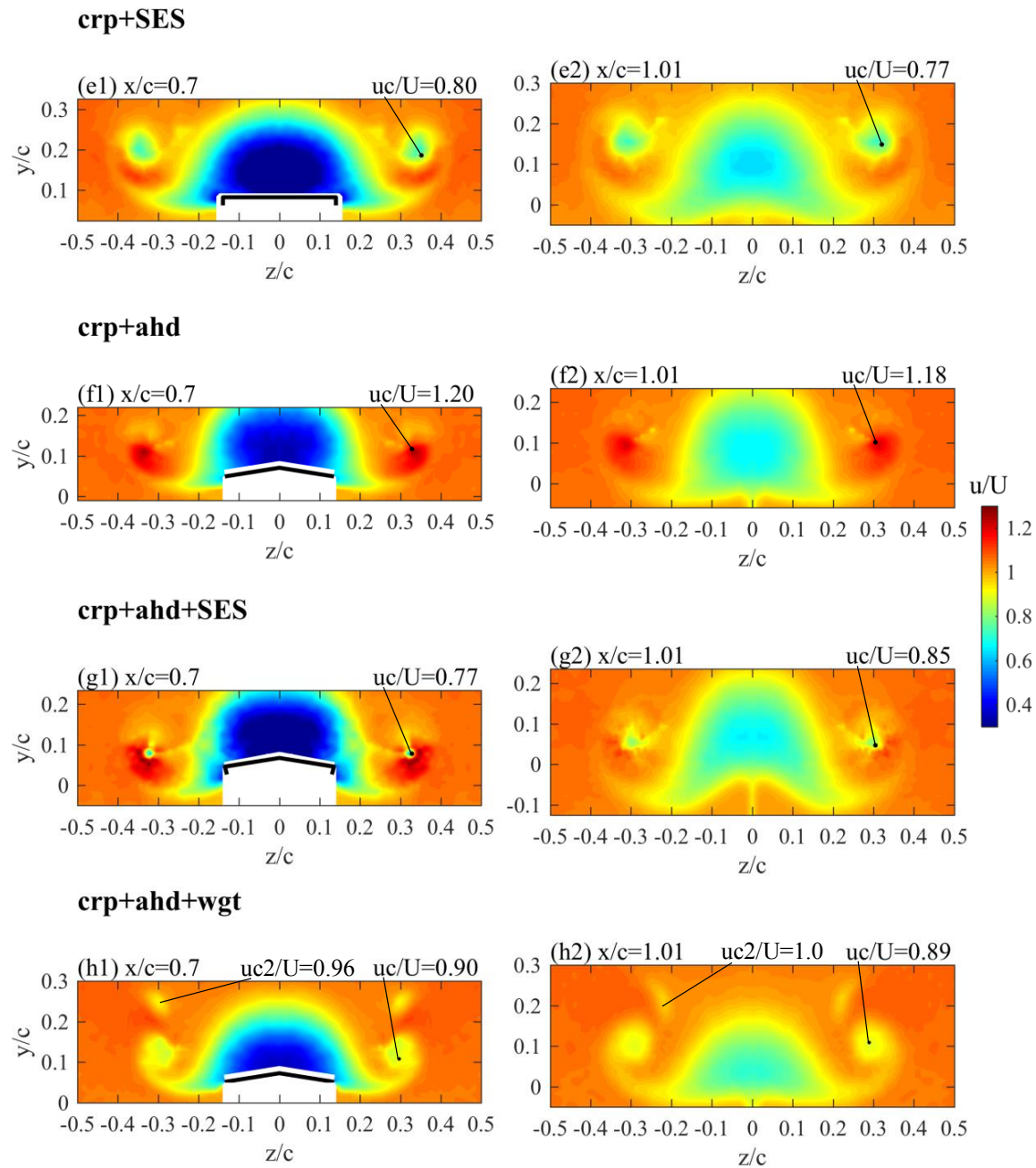


Figure 4-7: Normalized axial velocity contours at selected x/c . (continued)

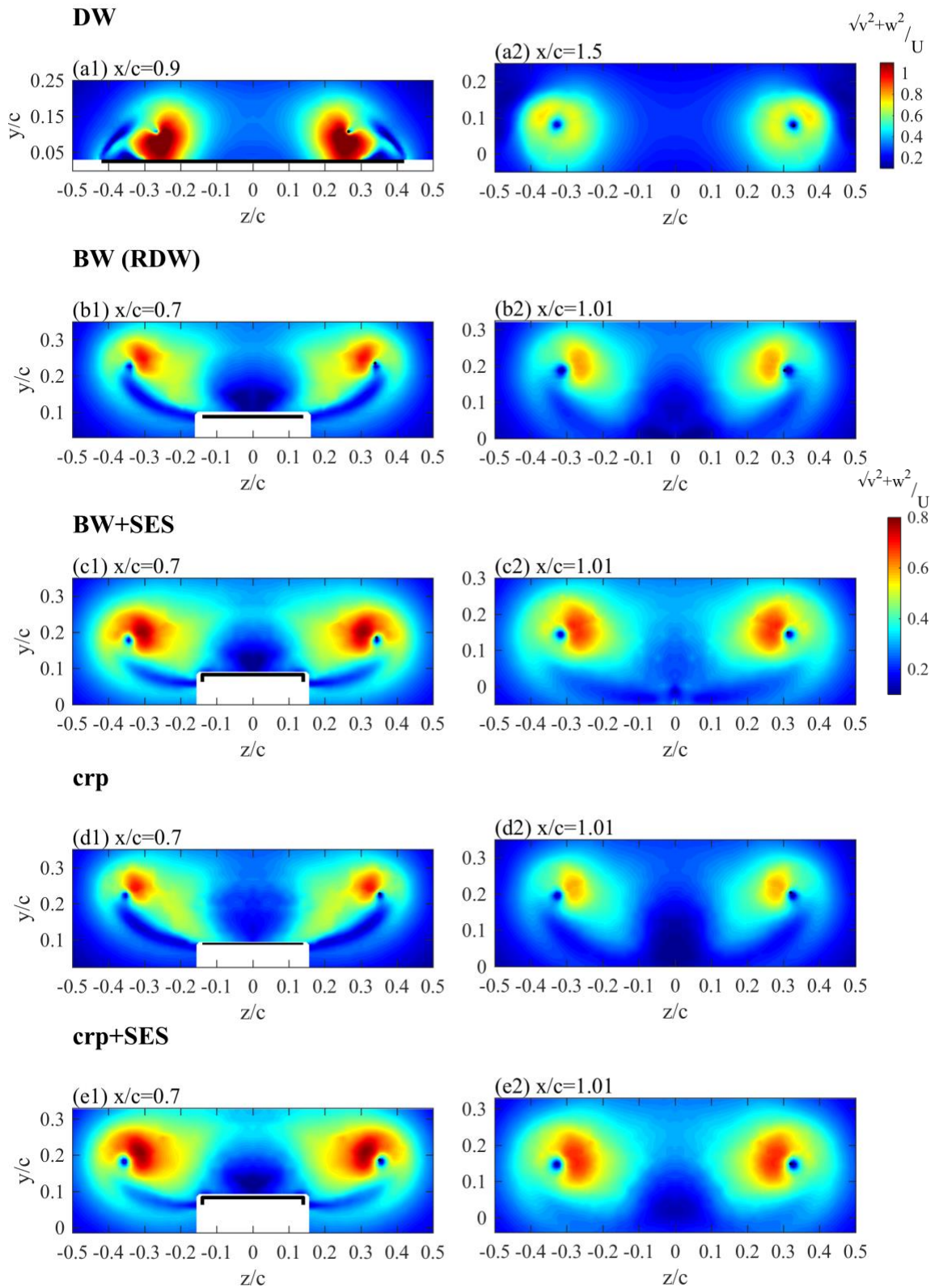


Figure 4-8: Normalized streamwise velocity contours at selected x/c .

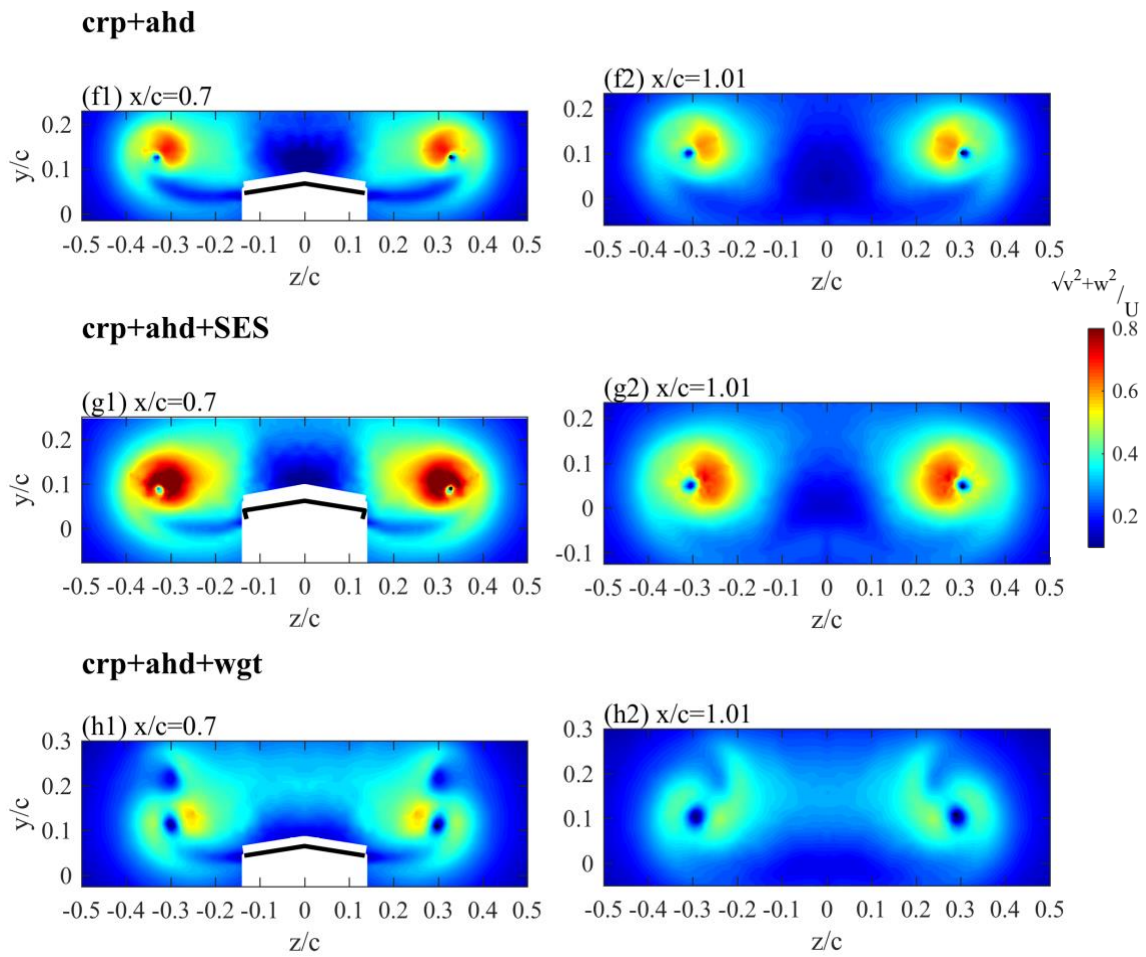


Figure 4-8: Normalized streamwise velocity contours at selected x/c . (continued)

minimum of the tangential velocity were rendered more equal ($v_{\theta,max} \approx |v_{\theta,min}|$), and the entire curve more symmetric about the origin. The magnitude of the maximum axial velocity decreased from 1.15 to 1.02, whose location eventually coincided with the vortex centre. Overall, the axial flow inside the vortex core was weak jet-like ($1 \leq u_c/U \leq 1.1$).

4.1.3 Aerodynamic Performance of the BW

The DW generated more lift ($C_{Lmax} = 1.49$) than the RDW ($C_{Lmax} = 1.21$) thanks to the vortex lift coming from the strong LEVs, but stalled earlier at $\alpha_{ss} = 33^\circ$. Figure 4–10 (a)–(c) show a comparison of the aerodynamic loads between the BW and its DW counterpart. The C_L curve of the DW was almost linear for $\alpha \leq 30^\circ$, but at $\alpha = 12^\circ$ on the BW, the linearity was disrupted by a drop in slope, signalling a change in the mechanism of lift production. Flow visualization of the same-sweep RDW at $\alpha = 14^\circ$ and 20° (Figure 2–3) revealed that three SVFs appeared on the upper surface and were intact at $\alpha = 14^\circ$. As α was increased to 20° , SVF3 was disrupted and the vortices were diffused, which was attributed to the instability of the SVFs and its interaction with the boundary layer. Near $\alpha_{ss} = 38^\circ$, it was reported that large disturbances from the three-dimensional flow leaked from the side edges broke down all three visible SVFs which gave birth to a large separated wake and ultimately the stalling of the wing [12]. As a result of the instability of the SVFs, the intervention of the side-edge flow, and the absence of leading-edge vortex lift, the RDW C_L curve attained its nonlinearity prior to stall and produced inferior maximum lift.

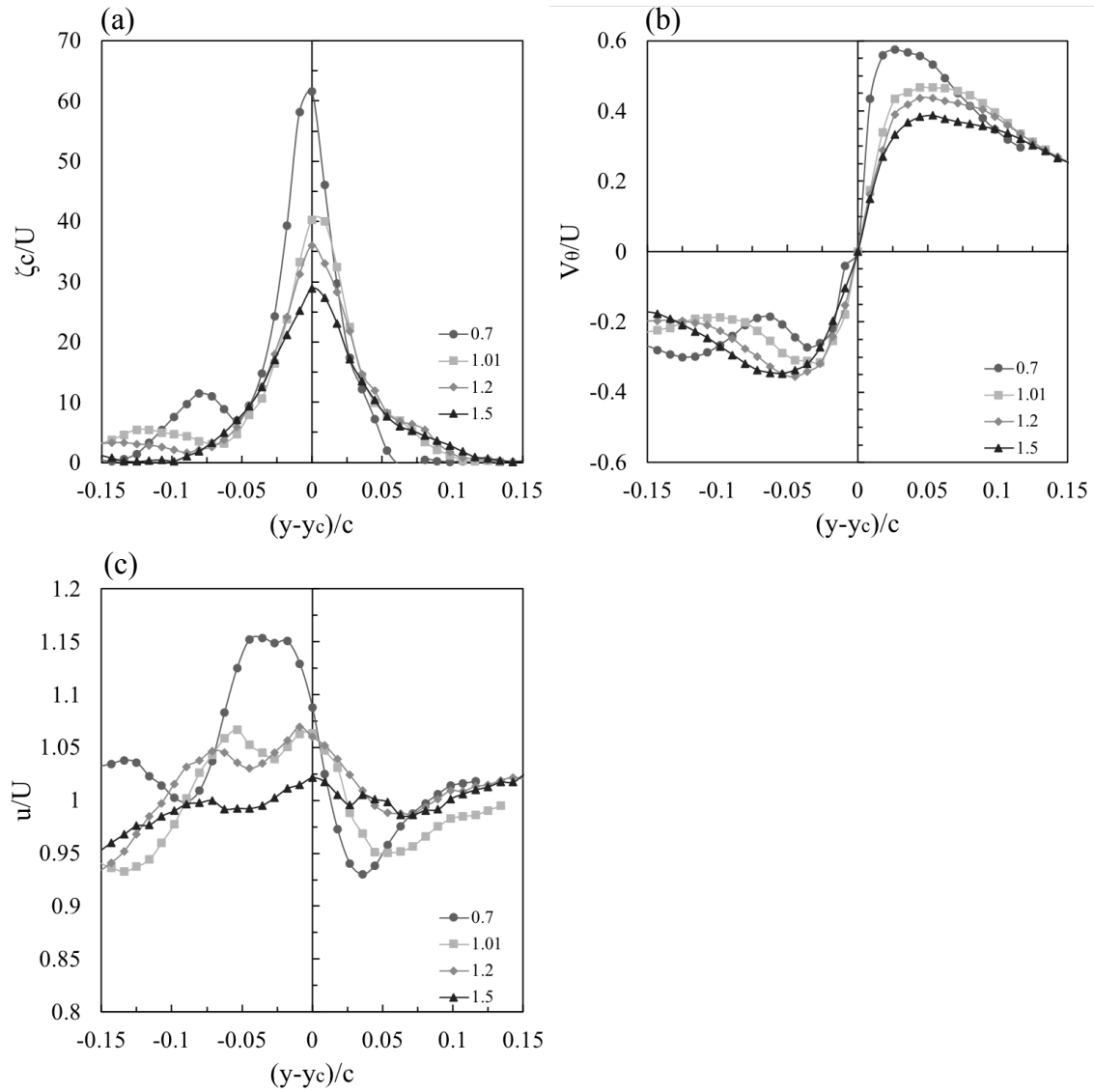
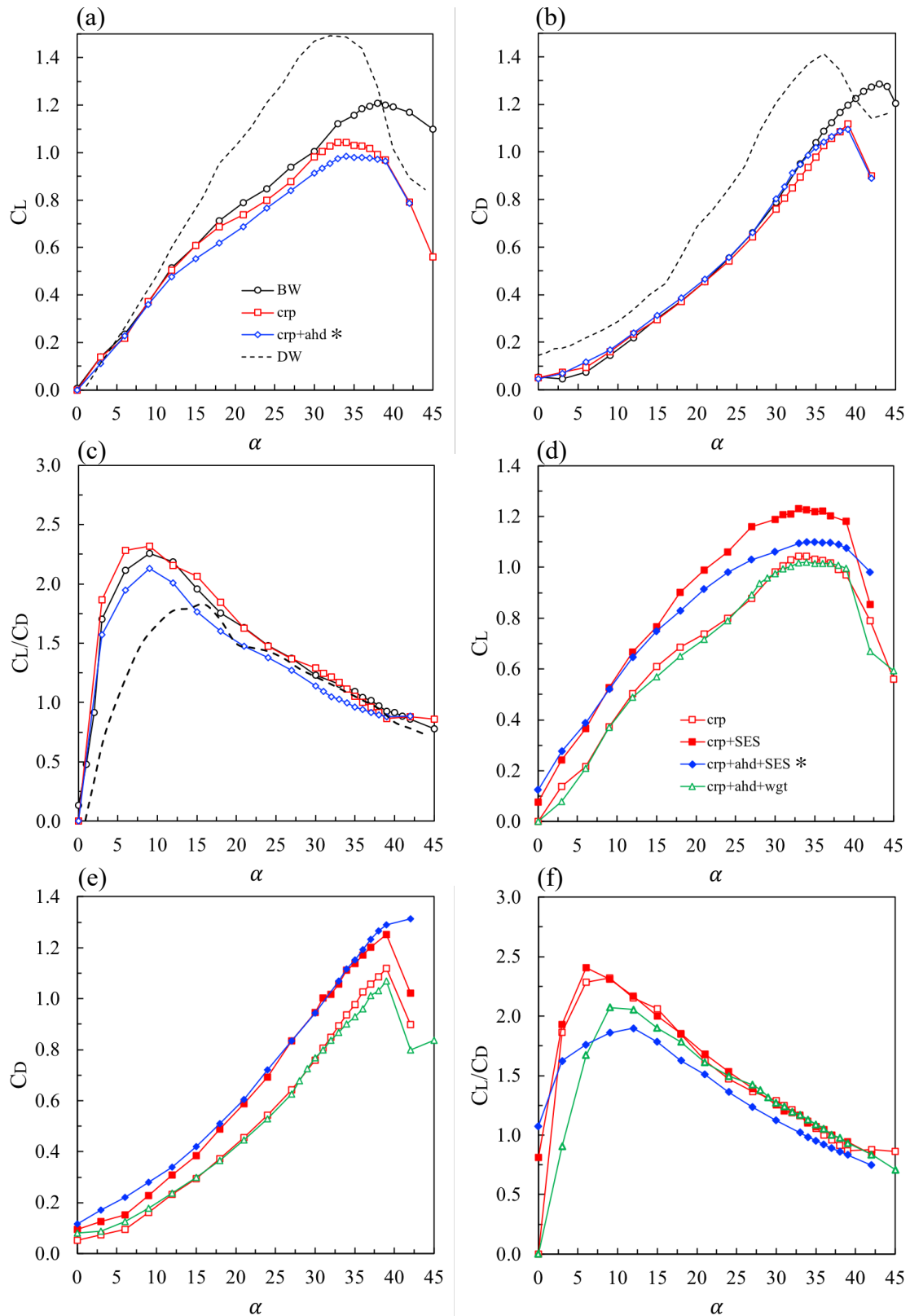


Figure 4-9: (a) Axial vorticity, (b) tangential velocity, and (c) axial velocity distributions of the baseline RDW vortex along a vertical line passing the vortex centre at selected x/c .



* Work contributed by Lee and Tremblay-Dionne

Figure 4-10: Lift and drag coefficient curves. (a)&(d) C_L curves, (b)&(e) C_D curves, (c)&(f) L/D curves.

The difference in the C_D curves of the DW and RDW was not as distinct as the C_L curves, found in Figure 4–10 (b). The DW had a higher drag, especially at medium to high α , which Lee and Ko [12] claimed to rise from the larger profile drag of the LEVs and the occurrence of vortex breakdown that was driven upstream with increasing α .

In plot (c) of the same figure, the baseline RDW produced lift more than twice as much as drag between $5^\circ \leq \alpha \leq 13^\circ$. L/D was the highest, 2.25, at $\alpha = 9^\circ$ where it was the most aerodynamically efficient. For $\alpha > 15^\circ$, the slope of decline was much gentler than at $\alpha < 5^\circ$, in other words, the loss in the aerodynamic efficiency was more forgiving at higher angles of attack.

4.2 Effect of 30% Cropping on the 65° RDW

To take full advantage of the ram pressure in ground effect, it is necessary for a WIG craft to minimize ground clearance whenever possible. A full-chord RDW planform, taking off at an angle of attack higher than in cruise mode, will demand large thrust to overcome the hydrodynamic drag on the rear section of the hull and tail. More importantly, having seen previously in the flow visualization of the RDW vortices, SVF breakdown was aggravated by the messy three-dimensional flow wrapping around the trailing apex at fairly low α . These reasons motivated the cropping of the trailing apex. In addition, the crop ratio directly translates to the percentage by which the vehicle can be displaced closer to the underlying surface than the BW, i.e., the 30% cropped RDW can fly 30% closer to the ground than the uncropped one at any given angle of attack. The 20%, 30%, and 40% cropping each introduces 4%, 9%, and 16% reduction in surface area, and in weight if given a

uniform distribution of density. On the other hand, the surface area reduction will adversely affect lift production, especially for the high-incidence regime. It is also expected to have an impact on the RDW vortex flow, in particular, the instability and breakdown of the SVFs at high angles of attack because of the geometrically modified trailing edge condition.

4.2.1 Vortex Flow Characteristics of the Cropped RDW

Following the same set of flow measurements as the BW, Figure 4–5 (b)-(c) demonstrate that in terms of the tangential and axial flow velocities in the vortex core, there was negligible difference between the cropped and regular planforms. Both the magnitude and streamwise trend of $v_{\theta peak}$ and u_c were nearly unchanged after cropping. Peak axial vorticity, ζ_{peak} , on the cropped RDW was 16% larger at maximum, occurring at $x/c = 0.3$, and the difference gradually shrank to zero in the wake. At $x/c = 1.5$, there was virtually no distinction in ζ_{peak} , $v_{\theta peak}$ and u_c between the vortices created by the cropped and baseline models, which was verified by the contour plots of Figure 4–6 (b) and (d). Figure 4–8 shows the cross-stream flow velocity contours at the cropped trailing edge. Between (b1) and (d1), air on the BW escaping from the side edges carried a larger cross-stream velocity than on the cropped RDW, meanwhile, the darker-coloured region on top of the BW indicated a lower spanwise velocity. The somewhat greater difference in the cross-stream velocity on the top and bottom of the BW suggests that it generated a greater pressure difference and thus lift than the cropped wing at $\alpha = 16^\circ$. The aerodynamic loads are discussed in more depth via force-balance data shortly after.

In Figure 4–5 (d), along the wing, the total circulation of the cropped RDW followed similar footsteps of the BW up to the cropped trailing edge at $x/c = 0.7$. Farther downstream, the disparity in Γ_o between the two models expanded as the BW vortex continued to strengthen at a greater rate. The levelling-off at $x/c = 1.1$ remained a commonality. $\Gamma_o = 0.22$ for the cropped wing at $x/c = 1.5$ was observed, an 8.3% drop from $\Gamma_o = 0.24$ on the BW. Due to the cropping, the vortex centre location was mildly more outboard and upward away from the top surface. Γ_c/Γ_o experienced a 8% decrease on the cropped wing, so did the r_c/r_o ratio. Lastly, no apparent deviation from the baseline case were discovered in ζ , v_θ , and u distributions across the vortex centre, included in Figure 4–5 (h)-(j).

4.2.2 Aerodynamic Performance of the Cropped RDW

The cropped RDW experienced an earlier stall and a lower maximum lift coefficient than the baseline RDW. The C_L curve resembled that of the BW closely for $0^\circ \leq \alpha \leq 18^\circ$. A minor decrease in C_L exhibited until stalling at $\alpha_{ss} = 33^\circ$ (Figure 4–10 (a)). $C_{Lmax} = 1.04$ on the cropped wing made up 86% of $C_{Lmax} = 1.21$ on the baseline wing. Because of the pivotal role of the SVFs in the stall mechanism of slender RDWs, the promoted stall can be resulted from an earlier SVF breakdown triggered by the 30% c cropped trailing edge. Additionally, the cropped trailing edge perpendicular to the free stream is likely to have induced a greater adverse pressure gradient that can contribute to the SVF breakdown. However, further investigation would be required to consolidate this argument.

Looking at the drags in Figure 4–10 (b), C_D of the cropped RDW did not depart much from the baseline case. For $\alpha < 15^\circ$, the cropped wing had a slightly larger drag

than the BW. The difference was gradually reversed past $\alpha = 21^\circ$. At $\alpha > 30^\circ$, the regular RDW would be accompanied by a larger wing profile drag, plus the cropped wing could retain a lower maximum drag in the means of promoted separated flow over the top surface.

There existed no practical variance between the baseline and cropped cases in terms of L/D , as the cropped wing had both marginally lower lift and drag at medium to high incidence angles.

4.3 Effect of 15° Anhedral on the 30%c Cropped RDW

The RFB X-113 utilized the planform anhedral and two floating sponsons at wingtips to raise the fuselage above the water. This catamaran design reduced the engine power required and the hydrodynamic drag penalty during take-off and at the same time achieved more power efficiency and quieter operations. The design continued on the much larger RFB X-114 that weighed more than twice of its predecessors and was capable of transporting six passengers. Later on, in order to better appeal to the mass market, the AF8 was designed to carry up to ten passengers and crew with a more spacious cabin. Having to also accommodate the low ground clearance from its cropped RDW planform, when floating, the hull under the fuselage and two sponsons form a trimaran design. The increased hydrodynamic drag had to be overcome by a 500 Hp V8 engine at take-off. The X-112 series and AF8 have an estimated planform anhedral of $15\text{-}20^\circ$.

4.3.1 Vortex Flow Characteristics of the Cropped RDW with Anhedral

The anhedral increased the peak vorticity and tangential velocity levels in the RDW vortex centre. As shown by Figure 4–5, comparing ζ_{peak} on the cropped wing

without and with anhedral, the increase in vorticity was far more pronounced along the wing. ζ_{peak} of the cropped wing with anhedral was 27.5% higher at $x/c = 0.3$, and the difference shrank to less than half, 12.5%, at $x/c = 1.5$. $v_{\theta peak}$ of the anhedral-equipped model reached the local maximum at $x = 0.4c$, possessing 16% larger velocity; by the last streamwise location ($x/c = 1.5$), it was only 7% higher than the flat cropped wing. The computed vortex radius on the anhedral-equipped model was 5% smaller, averaged over $x/c = 0.7 - 1.5$, but it did not result in a more concentrated vortex, as the average Γ_c/Γ_o remained the same as the cropped flat wing (Figure 4-5 (k)). The vortex strength was mainly unchanged along the wing chord, however, Γ_o of the cropped RDW did come on top of the anhedral-equipped counterpart marginally for $x/c \geq 1.1$ (Figure 4-5 (d)).

Effect of Anhedral on Crossflow

In Figure 4-8 (d1) and (f1), the roll-up can be observed similarly that the shear layer containing high-velocity spanwise flow escaped from the pressure side and looped inboard, sandwiching the boundary layer between the vortex and the lower-wall shear layer. The region of the highest crossflow was circulating above and inboard of the stagnant centre. The anhedral-equipped wing in (f1) induced a stronger roll-up in the sense that at the same streamwise location, high crossflow environed the vortex centre fully, and the boundary layer was deflected downward and away from the vortex centre. In contrast, the boundary-layer flow leaking from underneath the flat wing in (d1) penetrated the vortex centre, which obstructed the shear layer roll-up, resulting in lower tangential speeds and a less concentrated vortex core. Moreover, the crossflow contours depicted that a larger downwash was attached

to the top surface of the flat wing than on the anhedral-equipped wing, indicating that anhedral also helped minimize the downwash and therefore the induced drag. In plot (f2), at $x/c = 1.01$, the anhedral did not produce significantly faster rotating vortices, but the crossflow contours in the vortex appeared to be more concentrated and circular in comparison to the flat wing in (d2). Additionally, the anhedral planform kept the vortices closer to its wing surface and the faster crossflow rotation induced a mild inboard shift, but most of all, the high momentum led to a 34% reduction of the vertical shift from $x/c = 0.2$ to 1.5 in the vortex trajectory. (Figure 4-5 (f)-(g)).

Effect of Anhedral on Axial flow

Figure 4-7 (d) and (f) depict the axial wake behind the cropped wing without and with anhedral at the cropped trailing edge and the original trailing apex point. At $x/c = 0.7$, flow over the anhedral-equipped wing had a narrow wake width with a reduced wake deficit, implying that the anhedral reduced the size of the SVFs at the experimented incidence angle. The narrower separated wake with shrunk wake deficit persisted downstream on the anhedral-equipped model at $x/c = 1.01$, but the dissimilarity progressively perished with streamwise distance. The two cases exhibited similar wake sizes at $x/c = 1.5$, which suggests that the drag at $\alpha = 16^\circ$ on both should be more or less the same.

Another distinct effect of anhedral was an accelerated axial velocity in the vortex core region along the wing and in the near-field. At half a chord downstream of the trailing apex, a 5% increase in the core axial flow was recorded. The higher crossflow around the vortex core induced by the anhedral acted as a shield that prohibited the

free-stream from penetrating the core and retarding the axial flow, an idea extracted from the investigation by Lee and Pereira [27] on the jet-like or wake-like nature of the axial flow in a tip vortex.

4.3.2 Aerodynamic Forces of the Cropped RDW with Anhedral

The lift and drag of the cropped wing with anhedral did not differ significantly from the flat cropped wing. Between the two configurations, C_L was almost identical at low α (Figure 4–10 (a)). As α increased, the difference grew, with the latter generating more lift by 6% at their common stalling angle of 34° . At $\alpha = 16^\circ$, a 10% difference in C_L was seen. The lower lift coefficient was mainly due to the reduction in the projected surface area. The anhedral-equipped wing experienced a small increase in C_D at very low and high angles of attack until stalling, specifically for $\alpha < 9^\circ$ and $24^\circ < \alpha < 36^\circ$. From the earlier discussion that anhedral can help minimize induced drag, the increase found in total drag seems to have risen from a larger profile drag of the SVFs at rather low α . Lee et al. [45] found that C_L always decreased with increasing anhedral angle (δ_A) and C_D was larger at very low and high α for $\delta_A \leq 22^\circ$. They argued that the higher C_D could be caused by the variable behaviours of the flow over the wing's top surface. Extensive studies of the axial flow for different δ_A over a wide range of angles of attack are needed to support such deductions.

4.4 Effect of 2% Side-edge Strip on Different RDWs

Gurney flaplike side-edge strips with $h_{SES} = 2\%$ were retrofitted onto the BW, cropped wing without and with anhedral. In this section, the three SES-equipped wings are compared to their clean-wing (without SES) counterparts, as well as to

each other. While the majority of the various SES-induced effects were consistent and universal for the three clean-wing configurations, certain effects uniquely impacted one or two particular models.

4.4.1 Vortex Flow Characteristics of the SES-equipped RDWs

Effect of SES on Vorticity

The changes in peak vorticity levels with the employment of SES are seen in Figure 4–5 (a). Comparing each SES-equipped model with the respective non-SES model, a constant increase in ζ_{peak} on the BW exhibited for the entire experimented streamwise range. While ζ_{peak} initially decreased along the wing for the cropped RDW with SES, it recovered to the same level as the cropped RDW without SES beyond the trailing apex point ($x/c = 1.01$). As for the cropped wing with both anhedral and SES, ζ_{peak} was boosted by as much as 52% before the cropped trailing edge, then dipped rapidly to the same magnitude as the cropped wing with anhedral only. In summary, the addition of SES did not affect the peak vorticity at the vortex centre for $x/c \geq 1.01$, with the exception of the BW, where the SESs surrounded the side edges and intersected at the apex point, closing off the entire downstream-facing perimeter. Side-edge leakage was therefore obstructed along the entire maximum chord. In contrast, the SESs on the cropped wings were intercepted by the trailing edge introduced by cropping. As a result, the downstream perimeter stayed “open” and the vorticity-feeding by shear-layer roll-up also ceased after $x/c = 0.7$.

Effect of SES on Cross-stream Flow

The SESs engendered larger spanwise flow velocities in the tip vortices. During the early formation of the vortex, fluid carrying high-crossflow speed spewed from

the pressure side of the wing, bringing about stronger roll-up and higher tangential flow about the vortex centre, universally across all three clean-wing configurations, which is noted in the crossflow velocity contours in Figure 4–8 (b)-(g). Furthermore, the outreaching boundary-layer flow was consistently suppressed by the presence of the SESs. In a way, its length shortened, the outboard extension was averted from the vortex centre, and the retardation was less effective in the vortex centre, which also led to the higher tangential flow in the core. Increased levels of peak tangential velocity, shown in Figure 4–5 (b), are evident by the addition of the SESs. The effect on $v_{\theta peak}$ of the BW and cropped wing were nearly identical at every x/c . The v_{θ} values were increased for about 20% at $x/c = 1.5$, with even greater upstream differences. As for the cropped wing with anhedral, $v_{\theta peak}$ surged by 60% behind the leading edge, downstream however, the increase escalated to 13% at $x/c = 1.5$. The plummeting of the v_{θ} value beyond $x/c = 0.7$ was similar to the streamwise progression of ζ_{peak} . All in all, at the last streamwise location, $v_{\theta peak} \approx 0.45U$ was reached on all three SES-equipped configurations, despite the fact the anhedral also resulted in larger v_{θ} around the vortex core.

Returning to the crossflow velocity contour plots (Figure 4–8 (b1)-(g1)), the SESs created an equivalent spanwise camber effect that entrapped more air flow beneath the wing and ultimately gave rise to desirable lift augmentation. Comparing the three clean wings with their respective SES-equipped counterparts at $x/c = 0.7$, the side-edge-leakage flow contained higher spanwise velocities, so did the downwash on top of the wing, suggesting that the SESs inevitably generated more induced drag at the same time of more lift.

Effect of SES on Axial Flow

The SESs imposed a bigger wetted area on the wingtips of the clean wing, giving rise to a wake-like axial flow ($u_c/U < 1$) in the vortex centre at an early stage of vortex formation. The core axial velocity, u_c , started at near unity at $x/c = 0.3$ on all the SES-equipped models, and turned into more wake-like downstream (Figure 4-5 (c)). The high crossflow around the vortex core on the SES-equipped wings helped shelter the wake-like core from the surrounding jet-like flow. Farther downstream, the wake-like axial flow was sustained. Both the BW and cropped anhedral wing with SES experienced $u_c/U \approx 0.85$ at $x/c = 1.5$, and the cropped wing with SES alone suffered more severely at 0.77.

The separated wing wake behind each wing configuration can be identified in Figure 4-7 (b)-(g). At locations of $0.7c$ and $1.01c$, the wake grew in size by the employment of the SESs, nonetheless, the deficit in the centre of the separated wake became smaller. Additionally, the plots confirm the aforementioned SES-induced wake-like nature in the vortex core with the most impact found on the cropped wing with SES. Furthermore, at $x/c = 1.01$ behind the SES-equipped wings, larger axial-velocity deficits were apparent below $y/c = 0$, verifying the spanwise camber effect and the entrapment of flow under the wing. The enlarged wakes incited by SES are expected to result in higher drag forces on the SES-equipped wings, which is further examined in a following subsection.

Effect of SES on Vortex Strength

SES universally enhanced the vortex strength by 25-32% on all the clean wings. The BW and cropped anhedral wing, under the effect of the SES, achieved a

25% and 26% boost at $x/c = 1.5$, respectively. The streamwise trend of Γ_o for both models was consistently similar to their SES-free counterparts. Γ_o of the two rose steadily at the same rate for $x/c < 0.7$, then the BW with SES continued on while the cropped wing with joint anhedral and SES started flatlining. Both models eventually plateaued after the trailing apex (Figure 4–5 (d)). Nonetheless, the cropped wing with SES received more strengthening than the BW with SES throughout the streamwise stations, a 32% increase from its SES-free model at the last x/c where the BW and cropped wing with SES obtained a Γ_o of 0.298, and the cropped wing with joint anhedral and SES, 0.278. Figure 4–5 (k) reveals that in terms of Γ_c/Γ_o , the SESs rendered the vortices mildly more concentrated on the cropped models (+5%), but less on the baseline model (-8%) in the near-wake.

Effect of SES on Vortex Size and Trajectory

A small increase in the vortex radius was witnessed. r_o on the BW, cropped wing, and cropped wing with anhedral each increased by 12%, 8%, and 7% (averaged over $x/c = 1.01 - 1.5$). Linearized relations of r_o and x/c show that the SESs also slightly increased the streamwise growth rate of vortex radius on all three models by 0.5-1.8%, amongst which the BW was the most affected likely as a result of the fully “closed” downstream-facing trailing edges. Similar to Γ_c/Γ_o , r_c/r_o was increased by 4% in average on the cropped wings, and decreased by 10% on the BW with SES comparing to their respective clean wings (Figure 4–5 (l)).

With the SESs of $h_{SES} = 2\%c$, the vortex centre was displaced vertically (y_c/c) by 4.1% c and 3.9% c on the BW and cropped anhedral wing in the near-field, and

4.7% c on the cropped wing. No displacement in the spanwise direction (z_c/c) was observed between the SES-equipped models and their respective SES-free models.

The inconsistencies in the vortex strength enhancement and vertical displacement of the vortex centre found on the cropped wing with SES imply that the manufactured SES height for this particular model was erroneously larger than the SESs installed on the other two wings.

4.4.2 Aerodynamic Performances of the SES-equipped RDWs

The spanwise camber effect from the SES helped entrap air flow beneath the wing, boosting the positive pressure and achieving significant lift augmentation for the cropped wing without and with anhedral. The SES produced an upward shift of the C_L curve and an unchanged stalling angle, seen in Figure 4–10 (d)-(f). As much as 35% of lift enhancement was seen at low to medium angles of attack, from 12° to 27° . On the cropped wings, both flat and with anhedral, the use of SES increased C_{Lmax} by 18% and 12% in the vicinity of $\alpha_{ss} = 33 - 34^\circ$.

The lift augmentation by the SESs was accompanied by a higher drag, which can be mostly attributed to the larger separated wake and stronger crossflow in the tip vortices. C_D on both models hiked up, meanwhile, the drag increases at very low and high α in the effect of anhedral were persistent on the SES-equipped models. In general, the increases in C_D and C_L on the cropped wing led by the SES were one-to-one, leaving the L/D curve almost indistinguishable from its SES-free wing. Because of the higher C_D at very low α on the cropped wing with joint anhedral and SES, its L/D declined relative to its non-SES counterpart. The cropped wing with

SES had the best aerodynamic efficiency of 2.4 in the free stream at $\alpha = 6^\circ$ amongst all the configurations.

4.4.3 Effect of Joint Anhedral and SES on the cropped RDW

This wing configuration gave rise to the highest ζ_{peak} and $v_{\theta peak}$ along the cropped wing chord, it also produced the biggest downward vertical displacement in the vortex trajectory relative to the BW, making the closest vortices to the top surface of the RDW. Γ_o at $x/c = 1.5$ was 7% lower than the BW and cropped wing with SES. C_{Lmax} was 5% higher than the cropped clean wing, but 11% lower than the cropped wing with SES which rendered the best overall aerodynamic efficiency outside ground effect. It is anticipated for the aerodynamic efficiency of the RDW with anhedral and SES to overtake the other configurations in ground effect. RDWs with anhedral is capable of funneling more air into the “air cushion”. Lee et al. [46] reported that L/D rocketed by more than 40% for $\delta_A = 8-15^\circ$ when subject to extremely low ground proximity ($h/c < 10\%$). On top of that, the suppression of side-edge leakage by the SES could further maximize the ram effect and bring about a greater L/D .

4.5 Effect of 45° Winglets on the 30%*c* Cropped RDW with 15° Anhedral

Since the invention of the X-112 series, the Lippisch-type WIG vehicles have featured large winglets that contained ailerons to help stabilize the vehicle in pitch [18]. 50 years later, modern WIG crafts like the AF8 and WSH500 continue to adopt similar winglet designs equipped with ailerons. Specifically, the AF8 has two 2.3-meter long (17.5%*c*) winglets placed at 44° from the horizontal plane (schematics shown in Figure 1–4). It is in the author’s interests to investigate the effectiveness of the winglets as a passive tip-vortex control device. The next subsections examine the

effect of winglets by drawing comparisons between the cropped RDW with anhedral and winglets and the cropped wing with anhedral alone.

4.5.1 Vortex Flow Characteristics of the Winglet-equipped RDW

Behind the leading edge of the cropped wing with joint anhedral and winglets, a dual vortex pattern exhibited for $x/c = 0.2 - 1.01$. One was generated by the winglet tip, the other by the wing body itself, and the latter was predominant in vorticity, tangential velocity and vortex strength. For $x/c > 1.01$, the secondary vortex (winglet tip vortex) was no longer identifiable and slowly extruded into the main vortex. In the end, a single merged vortex was present at $x/c = 1.5$ (Figure 4-6 (h)), whose strength was surprisingly on par with that of the BW. Figure 4-5 (a)-(c) showed that the winglets did lessen the tip vortices, producing the lowest vorticity and crossflow velocity levels and a wake-like core axial flow. The primary and secondary vortices, each on their own, was weaker than the vortex of the cropped wing with only anhedral before $x/c \leq 1.01$. However, the merged vortex at $1.1 \leq x/c \leq 1.5$ had a strengthened circulation higher than its winglet-free model, actually matching the BW vortex strength.

The winglets also led to decelerated axial core flow, turning the jet-like flow on the cropped anhedral wing to wake-like in the dual-vortex. From axial velocity contours in Figure 4-7 (h1)-(h2), at the cropped trailing edge, u_c in the main vortex was 75% of that on the model without winglets, and u_c in the secondary vortex was just below the free-stream speed, which were maintained at $x/c = 1.01$. Depicted in the same plots, the separated wing wake developed behind the winglet-equipped model was nearly identical in size to its winglet-free counterpart, only wider and

shorter. It can be speculated that the drag forces on both models were more or less the same at $\alpha = 16^\circ$.

Figure 4-8 (h1)-(h2) uncover that the winglets brought about lower crossflow velocities in the core region but larger magnitude of downwash over the wing. Comparing the winglet-equipped model in (h) with the respective non-winglet model in (f), the merging of the main and secondary vortices suppressed the shedding of the boundary-layer flow but created faster rotational flow directly above the upper surface, consequently a higher induced drag. At $x/c = 1.01$, the vortex appeared to be the least concentrated in the sense of the larger region of near-zero tangential flow at the vortex centre. The entrainment of the secondary vortex was not yet complete.

This configuration generated vortices that were the closest to the trailing or side edges in the spanwise direction. The vertical displacement of the primary vortex was identical to the vortex produced by its winglet-free counterpart until the merging process accelerated with the dissipation of the secondary vortex. Beyond $x/c = 1.1$, the merging shifted the main vortex upward, deviating from the cropped anhedral wing in the vertical direction, meanwhile, more outboard in the spanwise direction. The outer radius of the main vortex was essentially the same as the BW vortex, based on linearized relations of r_o versus x/c .

4.5.2 Aerodynamic Performance of the Winglet-equipped RDW

Both C_L and C_D curves of the winglet-equipped model resembled those of the cropped wing, as can be seen in Figure 4-10 (c)-(f). C_L was higher than the cropped wing with only anhedral at medium to high angles of attack. At $\alpha_{ss} = 34^\circ$, C_{Lmax} was equal to 1.02 on the winglet-equipped configuration, which was 2% lower than the

cropped wing, and 6% higher than the cropped anhedral wing. Anhedral-induced high drag at low α was present on the winglet-equipped model, but a decline in C_D for $\alpha > 30^\circ$ put the drag below the cropped wing without and with anhedral. The lower drag suggests that a smaller separated wake was perhaps obtained with the addition of winglets near stalling.

Though winglets reduced the vorticity and tangential speed of the tip vortices, it surprisingly strengthened the vortices. The winglet-equipped model also brought about an inferior aerodynamic efficiency than the winglet-free models for $\alpha < 21^\circ$. The results suggested that the winglets on the Lippisch-type WIG craft are not necessarily an effective tip vortex control device. The X-112 series, AF8, and WSH500 all use short ailerons on their winglets, together with the large horizontal stabilizer and elevators in the rear, they serve to ensure the vehicle's stability in pitch. The 45° mounted ailerons, coupled with rudders on the rear vertical stabilizer, can also assist in roll maneuvers and reduce turning radius and overall agility of the craft.

4.6 Lift Estimation Using Vortex Strength

It has been shown that total circulation of tip vortex can correlate to the lift force on the wing. Lee and Su [13] reported that C_L computed using Γ_o of the tip vortex at $x/c = 3.0$ behind a NACA 0012 rectangular wing constituted approximately 80% the force-balance acquired C_L values over a range of angles of attack. One of the objectives of this project was to find out if such correlation stands for the RDWs.

The Polhamus' leading-edge suction analogy in Equation 2.6 provides an accurate and easy way to estimate C_L of slender delta wings at low to medium α [38]. For the 65° -sweep DW at $\alpha = 16^\circ$, $C_{L,P}$ based on Polhamus's formula was 0.807, with

K_v and K_p of 3.466 and 2.173 respectively using Equations 2.7 provided by Traub [39]. C_{L,Γ_o} , based on Γ_o and b' from the wake scan data at $x/c = 1.2$, was equal to 0.811. The actual C_L at $\alpha = 16^\circ$ was obtained from linear interpolation between the force-balance data points at $\alpha = 15^\circ$ and 18° . $C_{L,P}$ and C_{L,Γ_o} were in excellent agreement with $C_{L,FB}$ of 0.818, each underestimating the direct measurement by 1.4% and 0.8% respectively. The success of the circulation-based lift prediction lent more confidence to its application to the RDW vortices.

As discussed in previous sections, the vortex strength Γ_o universally plateaued after the streamwise location of $1.1c$ for all the models, therefore, Γ_o at $x/c = 1.2$ was selected to compute C_{L,Γ_o} . C_{L,Γ_o} and $C_{L,FB}$ values of each RDW configuration are presented in Table 4–1, including the DW.

Table 4–1: Predicted and measured lift coefficients at $\alpha = 16^\circ$

Wing configurations	Γ_o/cU	b'/c	C_{L,Γ_o}	$C_{L,FB}$	$\frac{C_{L,\Gamma_o}}{C_{L,FB}}$	ΔC_L
DW	0.295	0.320	0.811	0.818	99.2%	0.8%
BW	0.238	0.295	0.601	0.643	93.4%	6.6%
crp	0.219	0.305	0.573	0.635	90.2%	9.8%
crp+SES	0.298	0.313	0.800	0.812	98.5%	1.5%
crp+ahd	0.216	0.289	0.536	0.575*	93.2%	6.8%
crp+ahd+SES	0.278	0.289	0.689	0.776*	88.7%	11.3%
crp+ahd+wgt	0.239	0.281	0.577	0.597	96.7%	3.3%

* Work contributed by Lee and Tremblay-Dionne

For the RDW models, the circulation-based predictions underestimated the actual lift by 1.5% to 11.3%. Note that the computations of C_{L,Γ_o} using the wake scan data from $x/c = 1.1$ to 1.5 contained no disparity, among which the largest discrepancy was within 3.5% of the total C_L . In summary, the C_{L,Γ_o} estimates corresponded

to 88.7-99.6% of the actual lift measured on the RDWs, suggesting that the strength of RDW vortices can indeed represent the majority of the lift force in spite of being physically outboard of the wing body.

4.7 Induced Drag Estimation Using Streamwise Vorticity Field

Lift-induced drag coefficients, C_{Di} , were computed using the near-field cross-stream velocity and streamwise vorticity field acquired through the wake scans through Maskell's wake integral model, as described in Chapter 3 Section 3.4.2. The stream and velocity potential functions, ϕ and ψ , were solved from v and w using the finite difference method, then D_i was calculated by integrating ζ , σ (a special source term), and ϕ, ψ at each grid point in the downstream measurement plane. Detailed application can be found in [40].

The streamwise development of C_{Di} at $\alpha = 16^\circ$ is plotted in Figure 4-11. C_{Di} curve of the BW started at 0.021 and increased to a peak of 0.082 at $x/c = 0.6$, after a gentle decline, it levelled off at 0.68 at $x/c = 1.2$. On the other hand, C_{Di} on the DW climbed to a greater peak of 0.13 at its trailing edge ($x/c = 1.01$), dropped to 0.11 after $x/c = 1.2$, and became invariant farther downstream. The rest of the curves of RDW configurations obeyed a similar pattern as the BW, levelling off for $x/c \geq 1.2$ after the decline following the peak near the cropped trailing edge ($x/c = 0.7$). In the near-field ($x/c \geq 1.01$), it can be seen that the BW, cropped wing and winglet-equipped wing all experienced a similar induced drag at 16° . The anhedral resulted in a minimum D_i , and the SESs increased D_i on the BW and cropped wing. The cropped wing with SES saw the highest D_i among all the RDW models, approaching a similar value as the DW.

For consistency, C_{Di} values at $x/c = 1.2$ (same streamwise location chosen for the estimated C_{L,Γ_o}) were used to compare with the total drag C_D from force balance data ($C_{D,FB}$), tabulated in Table 4-2. For the RDW configurations, $C_{Di,M}$ (C_{Di} computed using Maskell's model) constituted 17.5-27.5% of $C_{D,FB}$. The

BW, cropped, and winglet-

equipped models had a C_{Di} in the range of 0.065-0.068, while the cropped wing with anhedral had the lowest value of 0.058, a 12.4% reduction from the cropped flat wing.

With the addition of the SESs, C_{Di} on the cropped wing increased by 70% relative to its SES-free counterpart, and the cropped wing with anhedral, by 50%. Furthermore, C_{Di,C_L} was also calculated by Equation 4.1 using experimentally measured C_L , aspect ratio AR , and an Oswald efficiency factor e of 0.9, and is included in Table 4-2 below.

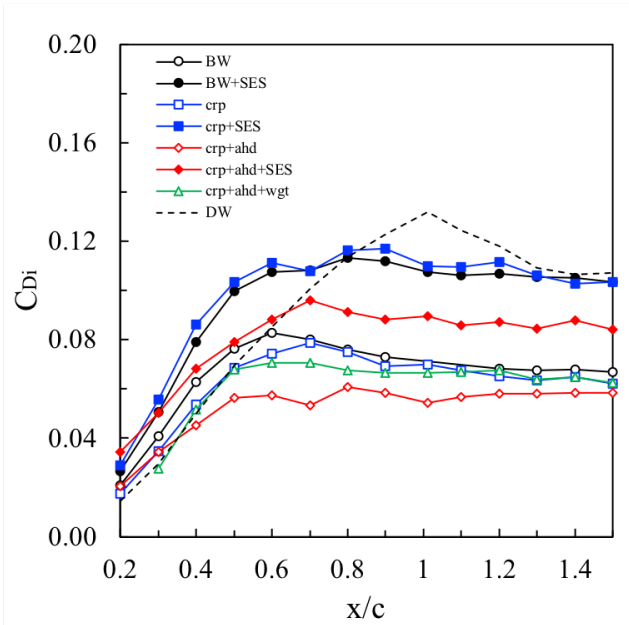


Figure 4-11: Streamwise development of the induced drag coefficients computed with the Maskell wake-intergral model.

$$C_{Di} = \frac{C_L^2}{\pi e AR} \quad (4.1)$$

Table 4-2: Estimated and theoretical induced drag coefficients at $\alpha = 16^\circ$

Wing configurations	$C_{D_i,M}$	C_{D_i,C_L}	$\frac{C_{D_i,M}}{C_{D_i,C_L}}$	$C_{D,FB}$	$\frac{C_{D_i,M}}{C_{D,FB}}$	$\frac{C_{D_i,C_L}}{C_{D,FB}}$	$\Delta_{C_{D_i}}$
DW	0.118	0.127	93.1%	0.448	26.4%	28.3%	2.0%
BW	0.0684	0.0784	87.2%	0.325	21.1%	24.2%	3.1%
crp	0.0651	0.0765	85.2%	0.321	20.3%	23.8%	3.5%
crp+SES	0.111	0.125	89.1%	0.405	27.5%	30.9%	3.4%
crp+ahd	0.0579	0.0627*	92.4%	0.329	17.6%	19.1%	1.4%
crp+ahd+SES	0.0872	0.114*	76.4%	0.442	19.7%	25.8%	6.1%
crp+ahd+wgt	0.0676	0.0676	100.1%	0.320	21.1%	21.1%	0.0%

* Work contributed by Lee and Tremblay-Dionne

C_{D_i,C_L} took up 19.1-30.9% of $C_{D,FB}$, and was in agreement with $C_{D_i,M}$. The Maskell method gave slightly lower estimates than the C_L -based method, with discrepancies under 3.5% of the total C_D for all the cases, except for the cropped RDW with joint anhedral and SES (which had a 6.1% discrepancy). Anderson [16] stated that induced drag of an airplane is about 25% of the total drag at cruise. According to Kroo [51], for a typical transport aircraft, the real-life induced drag accounts for roughly 40% of the total drag, which is 10-20% larger than the C_{D_i} obtained in this study. The accuracies of the wake integral results, including the lift and induced drag forces, can be improved by expanding the near-field wake survey plane in all three directions, should the spatial and temporal constraints of the experiment be ameliorated.

CHAPTER 5

Conclusions

Wingtip vortex characteristics and aerodynamic performances of a 65° reverse delta wing (RDW) of various wing configurations were investigated in the near field at an angle of attack of 16° and a Reynolds number of 3.3×10^5 . Some characteristics were universally observed in the streamwise evolution of tip vortices on all the RDW configurations. The peak axial vorticity, tangential velocity, and core axial velocity levels in the vortex core reached their local maxima around $x/c = 0.3$ and gently decayed with downstream progression. At half a chord length behind the wing ($x/c = 1.5$), peak tangential velocities in the vortices were generally 40-50% of the applied free-stream velocity, and vortex-centre axial velocities were either 10-15% above (jet-like) or below (wake-like) the free-stream speed. On the other hand, the vortex strengths increased with streamwise distance until the trailing apex point and mature to a plateau afterwards (for $x/c > 1.01$). The vortices grew almost linearly in size and their centre locations shift closer to the wing body further downstream. No matter the wing configuration, the tip vortices were persistently outboard, implying that they are impertinent to RDW's lift generation.

The 30%c trailing-apex cropping was proven to engender minimal changes to the vortex flow, with the exception that the vortex strength on the cropped RDW was 9% weaker than the BW and its spanwise centre location was the most outboard across the tested wing models. The lift and drag deviated very little from those of

the BW at low to medium angles of attack, however, the cropping promoted stalling ensued from 5° reduction in stalling angle and 15.5% drop in maximum lift.

The 15° anhedral produced mildly smaller and faster-rotating vortices which developed closer to the wing top surface by approximately 8% downstream. Nonetheless, the anhedral had a negative impact on the aerodynamic performance with inferior lift generation beyond angles of attack of 12° and higher drag at low and high angles near stall, despite that anhedral was found to minimize induced drag of the wing.

The employment of the Gurney flaplike side-edge strips (SES) with a height of $2\%c$ can effectively strengthen tip vortices by 25-32% and augment lift by up to 35% on all the wing models. In addition, the SESs led to higher tangential flow but decelerates axial flow in the vortex core, meanwhile, induced a $4\%c$ downward vertical displacement in the vortex trajectory (at $x/c = 1.5$). The cropped RDW with joint anhedral and SES gave rise to vortices that were the strongest vortices in peak vorticity and crossflow velocity and the nearest to the wing top surface vertically. Amongst the tested configurations, the combination of 30% cropping and $2\%c$ SES led to the highest lift coefficient and aerodynamic efficiency. On top of it, with the addition of the 15% anhedral, the maximum lift suffered a 12.5% drop, yet still came in second place in terms of lift generation. This joint anhedral and SES is anticipated to yield far superior aerodynamic efficiency in ground effect than the other configurations, as a result of the significantly boosted ram pressure by the “air tunnel” effect from the anhedral and hindered side-edge leakage from the SES.

The 45° winglets generated a pair of co-rotating vortices aside the wing which merged into a single tip vortex in the near field. The primary vortex produced by the wing body was stronger than the secondary vortex created by the winglet, and both were weaker than the RDW tip vortices of other configurations. However, their merged vortex turned out to be as strong as that of the baseline RDW, leading to respectable lift generation, on par with the cropped wing. The high vortex strength observed on the winglet-equipped model revealed that the winglets on the Lippisch-type WIG craft are rather for improving agility and stability in roll using ailerons.

Last but not least, the correlation between vortex strength (total circulation) and lift force was also investigated. The lift coefficient of each configuration was estimated using total circulation and effective span between their vortex pair, which agreed fairly well with the actual lift coefficients measured by force balance. Discrepancies between the estimated and measured lift, ranging from 1.5% to 11.3%, disclosed that the RDW vortex strength can represent majority of the wing's lift in spite of the suggested irrelevance to lift generation. Moreover, induced drag was computed via the vortex crossflow and vorticity field. The estimated induced drag coefficients constituted for 17.6-27.5% of the total drag with discrepancies lower than 6% compared to the theoretical values.

The next phase of work would naturally be focused on the aerodynamics of RDW tip vortices in ground effect, so as to quantitatively study the phenomenon behind the Lippisch-type WIG vehicles. Adopting the established experimental methods, the same set of variously configured RDW models could be subject to different levels of ground proximity at the same flow conditions and angle of attack, and the test

results of which could be analyzed and compared against the baseline or OGE cases in the current study. In particular, the vorticity contour plots would offer insights into the suppression of wingtip vortices in GE, and the computational analysis via Maskell's wake-integral model would help quantify the anticipated reduction of the induced drag. Corresponding force-balance measurements of lift and drag on these wing models may also be found interesting.

Furthermore, it would be beneficial to understand the influence of the Reynolds number of higher magnitude closer to that of real WIG vehicles, which was not achievable given the testing facility available to the present study. In reality, WIG vehicles often operate over unsteady bodies of water. To better emulate more realistic flying conditions in GE, more work could look into the effect of wavy grounds of various amplitude and wave lengths. On the other hand, moving grounds simulated by a belt conveyor system may also be of the interests of researchers and engineers.

References

- [1] M. Van Dyke, *An Album of Fluid Motion*. Standford, California: The Parabolic Press, 1982.
- [2] R. Arndt, *LIPPISCH AERODYNE RESEARCH (WW2-1972)*. [Online]. Available: <http://disaircraft.greyfalcon.us/LIPPISCHE%20AERODYNE%20RESEARCH.htm>. [Accessed June 15, 2018].
- [3] *Caspian Sea Monster KM Ekranoplan*. [Online]. Available: <https://www.youtube.com/watch?v=DGjXSg45iSY>. [Accessed June 15, 2018].
- [4] *AirFish 8 Gallery*. [Online]. Available: <http://www.wigetworks.com/airfish-8-gallery/>. [Accessed June 15, 2018].
- [5] *Wing Ship Technology Gallery*. [Online]. Available: http://www.wingship.com/?page_id=90. [Accessed June 15, 2018].
- [6] R. GRAY, “Chinese cyg-11 craft that can fly or ‘float’ on a cushion of air above the sea,” DailyMail.com: dailymail.co.uk, April 17, 2015. [Accessed June 3, 2018].
- [7] K. Fach, U. Petersen, and H. J. Reischauer], *Classification Experience with an 8 Seater WIG Craft*. [Online]. Available: <http://mararchief.tudelft.nl/file/37025/>. [Accessed June 21, 2018].
- [8] J. S. Chow, G. G. Zilliac, and P. Bradshaw, “Mean and turbulence measurements in the near field of a wingtip vortex,” *AIAA Journal*, vol. 35, pp. 1561–1567, 1997.
- [9] R. C. Nelson and A. Pelletier, “The unsteady aerodynamics of slender wings and aircraft undergoing large amplitude maneuvers,” *Progress in Aerospace Sciences*, vol. 39, pp. 185–248, 2003.

- [10] N. C. Lambourne and D. W. Bryer, “The bursting of leading edge vortices: Some observation and discussion of the phenomenon,” tech. rep., London HMSO RM 3282, 1962.
- [11] I. Gursul, Z. Wang, and E. Vardaki, “Review of flow control mechanisms of leading-edge vortices,” *Progress in Aerospace Sciences*, vol. 43, pp. 246–270, 2007.
- [12] T. Lee and L. S. Ko, “Experimental study of the vortex flow and aerodynamic characteristics of a reverse delta wing,” *Journal of Aerospace Engineering*, vol. 230, p. 1126–1138, 2016.
- [13] T. Lee and Y. Y. Su, “Aerodynamic performance of a wing with a deflected tip-mounted reverse half-delta wing,” *Experiments in Fluids*, vol. 53, pp. 1221–1232, 2012.
- [14] J. Pereira, *Experimental Investigation of Tip Vortex Control Using a Half Delta Shaped Tip Strake*. PhD thesis, McGill University, Montreal, Quebec, Canada, 2011.
- [15] M. Pubby, “‘Wake turbulence’ led to C-130 J aircraft crash,” *The Indian Express*: indianexpress.com, April 23, 2014. [Accessed June 3, 2018].
- [16] J. D. Anderson Jr., *Fundamentals of Aerodynamics*. New York, NY: McGraw-Hill, 5th ed., 2011.
- [17] A. Lippisch, “Alexander Lippisch Papers,” MS 243, Special Collections Department, Iowa State University Library, 1897-1993, undated.
- [18] K. V. Rozhdestvensky, “Wing-in-ground effect vehicles,” *Progress in Aerospace Sciences*, vol. 42, p. 211–283, 2006.
- [19] B. Gunston, *The Osprey Encyclopedia of Russian Aircraft 1875-1995*. London: Osprey Aerospace, 1995.
- [20] R. Babikian, *The Historical Fuel Efficiency Characteristics of Regional Aircraft from Technological, Operational and Cost Perspectives*. PhD thesis, Department of Aeronautics and Astronautics, Massachusetts Institute of Technology, Cambridge, MA, USA, 2001.

- [21] *Background of FF*. [Online]. Available: <http://www.fischer-flugmechanik.com/site/index.php?menu=background>. [Accessed June 20, 2018].
- [22] International Maritime Organization, “Wing-in-ground (WIG) craft,” 2003.
- [23] W. R. C. Phillips, “The turbulent trailing vortex during roll-up,” *Journal of Fluid Mechanics*, vol. 105, pp. 451–467, 1981.
- [24] G. K. Batchelor, “Axial flow in trailing line vortices,” *Journal of Fluid Mechanics*, vol. 20, pp. 645–658, 1964.
- [25] B. R. Ramaparian and Y. Zheng, “Measurements in rollup region of the tip vortex from a rectangular wing,” *AIAA Journal*, vol. 35, pp. 1837–1843, 1997.
- [26] D. Birch, T. Lee, F. Mokhtarian, and F. Kafyeke, “Structure and induced drag of a tip vortex,” *Journal of Aircraft*, vol. 41, pp. 1138–1145, 2004.
- [27] T. Lee and J. Pereira, “Nature of wakelike and jetlike axial tip vortex flows,” *Journal of Aircraft*, vol. 47, pp. 1946–1954, 2010.
- [28] N. A. Chigier and V. R. Corsiglia, “Tip Vortices-Velocity Distributions,” tech. rep., NASA-TM-X-62087, 1971.
- [29] P. Gerontakos and T. Lee, “Lift-induced drag of a cambered wing for $Re < 1 \times 10^6$,” *Experiments in Fluids*, vol. 42, pp. 363–369, 2007.
- [30] T. Lee and S. Choi, “Wingtip vortex control via tip-mounted half-delta wings of different geometric configurations,” *ASME Journal of Fluids Engineering*, vol. 137, p. 121105, 2015.
- [31] K. Kusunose, “Drag prediction based on a wake-integral method,” *AIAA-98-2723*, 1998.
- [32] E. Maskell, “Progress towards a method for the measurement of the components of the drag of a wing of finite span,” *RAE Technical Report 72232*, 1973.
- [33] R. C. Nelson and K. D. Visser, “Breaking down the delta wing vortex: The role of vorticity in the breakdown process,” University of Notre Dame, Notre Dame, Indiana, USA, 1990.
- [34] P. Earnshaw, “An experimental investigation of the structure of a leading edge vortex,” tech. rep., RAE Technical Report 2740, 1961.

- [35] M. Hall, “Vortex breakdown,” *Annual Review of Fluid Mechanics*, vol. 4, p. 195–218, 1972.
- [36] I. Gursul, “Review of unsteady vortex flows over slender delta wings,” *Journal of Aircraft*, vol. 42, p. 299–319, 2005.
- [37] W. H. Wentz, Jr. and D. L. Kohlman, “Wind tunnel investigations of vortex breakdown on slender sharp edged wings,” *NASA Technical Report FRL-68-013*, 1968.
- [38] E. C. Polhamus, “A concept of the vortex lift of sharp-edge delta wings based on a leading-edge suction analogy,” tech. rep., NASA TN D-3767, 1966.
- [39] L. W. Traub, “Implications of the insensitivity of vortex lift to sweep,” *Journal of Aircraft*, vol. 37, pp. 531–533, 2000.
- [40] T. Lee and Y. Y. Su, “Wingtip vortex control via the use of a reverse half-delta wing,” *Experiments in Fluids*, vol. 52, p. 1593–1609, 2012.
- [41] A. O. Ancel, R. Eastwood, D. Vogt, C. Ithier, M. Smith, R. Wood, and M. Kovač, “Aerodynamic evaluation of wing shape and wing orientation in four butterfly species using numerical simulations and a low-speed wind tunnel, and its implications for the design of flying micro-robots,” *Interface Focus*, p. 7: 20160087, 2016.
- [42] A. Altaf, A. A. Omar, W. Asrar, and H. B. L. Jamaluddin, “Study of the reverse delta wing,” *Journal of Aircraft*, vol. 48, pp. 277–286, 2011.
- [43] T. Lee and L. S. Ko, “Vortex flow and lift generation of a non-slender reverse delta wing,” *Journal of Aerospace Engineering*, vol. 231, pp. 2438–2451, 2017.
- [44] T. Lee, “Impact of gurney flap-like strips on the aerodynamic and vortex flow characteristic of a reverse delta wing,” *ASME Journal of Fluids Engineering*, vol. 138, pp. 1–9, 2016.
- [45] T. Lee, L. S. Ko, and V. Tremblay-Dionne, “Effect of anhedral on a reverse delta wing,” *Journal of Aerospace Engineering*, 2017.
- [46] T. Lee, V. Tremblay-Dionne, and L. S. Ko, “Ground effect on a slender reverse delta wing with anhedral,” *Journal of Aerospace Engineering*, 2018.

- [47] C. W. Wenger and W. J. Devenport, “Seven-hole pressure probe calibration method utilizing look-up error tables,” *AIAA Journal*, vol. 37, pp. 675–679, 1999.
- [48] S. Kaplan, A. Altman, and M. Ol, “Wake vorticity measurements for low aspect ratio wings at low reynolds number,” *Journal of Aircraft*, vol. 44, pp. 241–251, 2007.
- [49] M. B. Giles and R. M. Cummings, “Wake integration for three-dimensional flowfield computations: Theoretical development,” *Journal of Aircraft*, vol. 36, pp. 357–365, 1999.
- [50] R. J. Moffat, “Contributions to the theory of single-sample uncertainty analysis,” *Journal of Fluids Engineering*, vol. 104, pp. 250–258, 1982.
- [51] I. Kroo, “DRAG DUE TO LIFT: Concepts for Prediction and Reduction,” *Annual Review of Fluid Mechanics*, vol. 33, pp. 587–617, 2000.